Nano-Micro Letters
e-ISSN 2150-5551
CN 31-2103/TB
REVIEW
https://doi.org/10.1007/s40820-026-02111-0

Cite as
Nano-Micro Lett.
(2026) 18:266

Received: 11 December 2025
Accepted: 20 January 2026

Design Concept of Metal Sulfide Photocatalyst for Efficient Photocatalytic Hydrogen Evolution

Qizhi Gao[1], Xinlong Zheng[1], Jiaxin Lin[1], Jiadi Zhai[1], Fan Yang[1], Xinjie Chen[1], Minghui Wang[1], Miaomiao Yang[1], Jing Li[1], Xiaodong Shi[1], Yonghao Xiao[1] ✉, Xinlong Tian[1] ✉, Yuhao Liu[1] ✉

HIGHLIGHTS

- Highlighting the essential 3D electronic dimensionality, isotropic orbital hybridization is shown to enhance charge carrier mobility in metal sulfide (MS) photocatalysts, overcoming structural dimensionality limits.
- A controllable-photocorrosion approach is developed to functionally harness corrosion, in situ generating catalytically active sulfur species that boost photocatalytic hydrogen evolution and structural durability.
- The intrinsic sulfur-coordination directionality synthesis method suppresses MS photocorrosion, offering a scalable stability enhancement, proved for CdS and ZnCdS systems.

ABSTRACT Metal sulfide (MS) photocatalysts hold unique features of narrow-bandgap range, high light absorption coefficient, and suitable band structures, offering significant potential for efficient visible-light photocatalytic hydrogen evolution (PHE) via water splitting. However, the low electronic dimensionality of the traditional MS photocatalyst generally decreases the transfer and migration efficiency of the photogenerated charge carriers. In addition, severe intrinsic photocorrosion issue also severely reduces the photostability, hindering the practical application of PHE at scale. In this regard, the advanced design concept of MS photocatalysts, focusing on the high electronic dimensionality construction and efficient photocorrosion inhibition, is of great importance. This review firstly introduces the basic mechanisms of PHE, followed by an in-depth discussion of the fundamental distinction between structural dimensionality and electronic dimensionality, highlighting the superiority of 3D electronic connectivity in enabling isotropic charge migration and shallow defect states. Afterward, the MS photocatalysts with 3D electronic dimensionality and solutions to photocorrosion are systematically summarized, with a special emphasis on the emerging paradigm of advanced "controllable-photocorrosion," which strategically utilizes the corrosion process to create active sites rather than merely suppressing it. Finally, the current unsolved challenges of MS photocatalysts are comprehensively discussed.

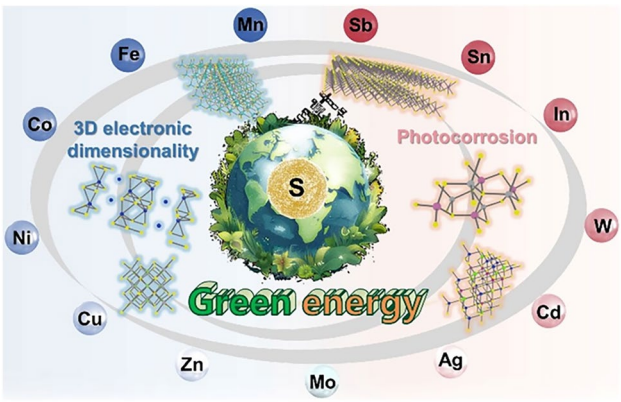

KEYWORDS Metal sulfide photocatalysts; Photocatalytic hydrogen evolution; Water splitting; Electronic dimensionality; Photocorrosion

Qizhi Gao, Xinlong Zheng, and Jiaxin Lin contributed equally to this work.
✉ Yonghao Xiao, yonghao.xiao@hainanu.edu.cn; Xinlong Tian, tianxl@hainanu.edu.cn; Yuhao Liu, yhliu@hainanu.edu.cn
[1] State Key Laboratory of Tropic Ocean Engineering Materials and Materials Evaluation, School of Marine Technology and Equipment, School of Materials Science and Engineering, Hainan Provincial Key Lab of Fine Chem, School of Cyberspace Security (School of Cryptology), School of Physics and Optoelectronic Engineering, Hainan University, Haikou 570228, People's Republic of China

Published online: 02 March 2026

1 Introduction

The prevailing reliance on traditional energy sources results in detrimental environmental impacts and severe energy security challenges [1–16]. The emerged hydrogen energy is a key candidate due to its promise of zero emissions and remarkably high energy density [17–24]. Among hydrogen production methods, photocatalytic hydrogen evolution (PHE) via water splitting stands out as a particularly promising approach for the direct and sustainable conversion of solar energy [25–30], relying on the exploration of semiconductor photocatalysts. Since the initial development of TiO_2 for photoelectrochemical water splitting [31], the semiconductor-based photocatalysis has been established as a promising PHE pathway. This breakthrough spurred extensive research efforts aimed at enhancing the PHE efficiency of TiO_2 [32–36]. At the same time, a wide array of other metal oxide (MO) photocatalysts, typically ZnO, CeO_2, WO_3, SnO_2, and $BiVO_4$, have been simultaneously investigated and applied in PHE technique [37–47]. However, the charge separation efficiency in most MO photocatalysts remains limited, largely due to the highly localized nature of O 2*p* states, which leads to a large effective mass of photogenerated holes. Moreover, the dominance of deeply lying of O 2*p* orbitals in the valence band (VB) results in wide bandgap [48]. In this case, PHE applications employing MO are generally restricted to ultraviolet (UV) light activation, which constitutes only about 4% of the solar spectrum. To achieve efficient PHE under visible light, the exploration and development of narrow-bandgap semiconductor photocatalysts are therefore imperative [49–51].

Metal sulfide (MS) semiconductor materials have garnered significant research attention as visible-light photocatalysts due to their inherently narrow bandgaps, which arise from S 3*p* orbitals, pronounced quantum size effects, and low carrier effective masses [52–59]. These attributes enable efficient solar spectrum utilization, extending light absorption from UV into the visible region, while their elevated conduction band (CB) potentials provide robust thermodynamic driving forces for hydrogen evolution reaction (HER) [60–62]. Typical examples including CdS, ZnCdS, $ZnIn_2S_4$, $CuInS_2$, and Cu_2ZnSnS_4 (CZTS) represent a strategic research direction for achieving high-efficiency visible-light-driven PHE [63–68]. The approaches to improve the performance of MS photocatalysts, including morphology/structure engineering, elements doping, vacancy introduction, and heterojunction engineering, have been widely investigated [69–76], while the electronic dimensionality characteristics of MS photocatalysts have received little attention. Moreover, MS photocatalysts generally suffer from photocorrosion [77–80], which greatly hinders the long-term photostability. In this case, the design concept focusing on the electronic dimensionality and photocorrosion solutions is crucial for exploring the advanced MS photocatalysts to enable the scale-up PHE application.

The concept of "3D electronic dimensionality" transcends the conventional focus on structural dimensionality (0D, 1D, 2D, 3D). The structural dimensionality describes the geometric morphology, whereas electronic dimensionality defines the spatial connectivity of atomic orbitals constituting the band edges. A material can possess a 3D crystal structure but suffer from low electronic dimensionality due to directional orbital confinement, leading to the low charge migration efficiency. True 3D electronic dimensionality, characterized by isotropic orbital hybridization in all directions, is the key determinant for low effective mass, high carrier mobility, and benign defect properties [81–83]. At the same time, the controllable-photocorrosion strategy represents a paradigm shift from conventional corrosion suppression. Traditional approaches for solving photocorrosion, such as cocatalyst deposition or heterojunction construction, aim to passively prevent the oxidation of S^{2-} ions by extracting the photogenerated holes [63]. In contrast, the controllable-photocorrosion actively engineers the material to harness the photocorrosion process. The initial, controlled photocorrosion sacrificially consumes holes and, more importantly, in situ generates highly active sulfur species that boost the HER, while a robust subsurface layer halts further destruction. This transforms a detrimental process into a self-optimizing, functional mechanism for enhanced and stable performance. The visual contrast of 3D electronic dimensionality with lower dimensions and the corresponding illustration of controllable-photocorrosion mechanism are shown in Fig. 1. Therefore, on the basis of the construction of 3D electronic dimensionality, the substantial inhibition or fundamental solution to the photocorrosion issue of MS photocatalysts is also crucial.

In parallel with the increasing research efforts on MS photocatalysts, several representative reviews have focused on the photocatalytic applications. Typically, Chandrasekaran et al. comprehensively summarize controlled synthesis,

https://doi.org/10.1007/s40820-026-02111-0

property modulation, and applications of MS nanocrystals in electrocatalytic, PHE, and photoelectrochemical water splitting, highlighting structure–performance relationships and future scientific research directions [85]. Furthermore, considerable attention has also been given to emerging MS photocatalysts such as $CuInS_2$, $ZnIn_2S_4$, ZnCdS, etc., which have been extensively reviewed for their broad PHE application [86–90]. Despite these notable reviews, a systematic overview that addresses both electronic dimensionality and innovative strategies for mitigating photocorrosion remains lacking. Given the key roles of 3D electronic dimensionality and photostability, this review highlights the recent advances of MS photocatalysts exhibiting 3D electronic dimensionality and effective resistance to the photocorrosion. The basic mechanism of PHE via water splitting is firstly introduced, and thereafter, the exploration of MS photocatalysts in PHE applications is concisely summarized. Subsequently, the design concept of 3D electronic dimensionality and photocorrosion solution of MS photocatalysts are provided, and the explored advanced MS photocatalysts with 3D electronic dimensionality and promising photocorrosion solution features are comprehensively discussed. Particularly, the evolution from lower (0D/1D/2D) to three-dimensional (3D) electronic connectivity represents a critical pathway to overcome the charge separation/migration and stability bottlenecks in next-generation MS photocatalysts. Finally, the current challenges and future research directions for advanced MS photocatalysts are presented, which may inspire the development of more suitable materials for the PHE.

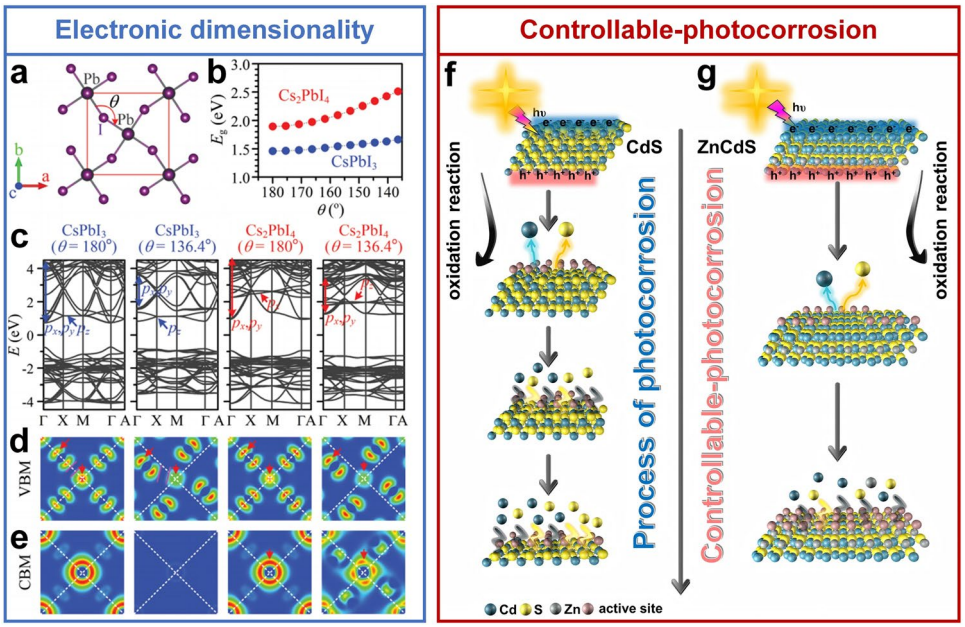

Fig. 1 A visual exhibition of electronic dimensionality (blue part) and controllable-photocorrosion (red part). Fundamental concepts for advanced design of MS photocatalyst: **a** Schematic illustration of in-plane Pb–I–Pb bond angle (θ) variation in model 3D $CsPbI_3$ and 2D Cs_2PbI_4 perovskites. **b** Calculated bandgaps increase as θ decreases, with 2D systems exhibiting greater sensitivity due to their lower electronic dimensionality. **c** Band structures and charge density distributions for the **d** VBM and **e** CBM under ideal ($\theta = 180°$) and distorted ($\theta = 136.4°$) configurations. Reduced orbital overlap along the inorganic framework diminishes electronic connectivity, effectively lowering the electronic dimensionality. This suppresses carrier dispersion and raises band edges, providing a conceptual link between structural distortion, electronic dimensionality, and band engineering in functional materials. Reproduced with the permission of Ref. [81]. Copyright 2017, Elsevier. Comparison of uncontrolled photocorrosion and engineered controllable-photocorrosion: **f** Schematic of the deleterious positive feedback loop in traditional MS (CdS as example): accumulation of photogenerated holes triggers uncontrolled sulfide oxidation ($CdS + 2\,h^+ \rightarrow Cd^{2+} + S$), causing massive sulfur vacancy generation, structural degradation, and permanent activity loss. **g** Innovative "controllable-photocorrosion" paradigm based on ZnCdS solid solution in Ref. [84]. This self-limiting process involves: (i) The sacrificial sulfur-rich surface layer is selectively oxidized by holes, consuming the corrosive species and in situ generating catalytically active sulfur sites that enhance HER kinetics. (ii) The predefined corrosion front is autonomously halted upon reaching the underlying robust Zn–S layer, preventing bulk degradation. This transforms photocorrosion from a failure mechanism into a functional tool for performance augmentation and stability

2 Fundamental Mechanisms and Core Concepts

2.1 Mechanism of PHE via Water Splitting

Photocatalytic water splitting is a process involving the decomposition of water into hydrogen and oxygen [91–98], which necessitates incident photons with energies exceeding the thermodynamic threshold of 1.23 eV to generate the charge carriers (electron−hole pairs) under light irradiation. Concurrently, harnessing visible-light radiation for efficient PHE mandates a semiconductor band gap predominantly below 3.0 eV. Thermodynamically, water splitting is associated with a significant positive Gibbs free energy ($\Delta G_{H^*} = 237$ kJ mol^{-1}) change, rendering it a highly endergonic process [64]. This substantial energy barrier constitutes a fundamental limitation for PHE approaches. PHE via water splitting comprises three pivotal phases that govern overall system efficiency [25, 99]: (i) Semiconductor photocatalysts initiate energy conversion by ultrafast generation of electron−hole pairs upon photon absorption (Fig. 2a). (ii) Segregated electrons and holes migrate to respective cocatalysts, driving HER and oxygen evolution reaction (OER) (Fig. 2b). Semiconductor photocatalysts require appropriate band potentials to drive HER and OER, while effective charge management is crucial to minimize major energy loss from recombination.

2.2 Scientific Principle of Electronic Dimensionality

The realization of efficient PHE requests semiconductors with optimal photoelectric properties, most critically a bandgap tailored for visible-light-spectrum absorption (1.23–3.0 eV) to maximize solar energy utilization (Fig. 2c) [100–106]. However, beyond the bandgap, the efficiency of charge migration, a process pivotal to the second phase of PHE, is also fundamentally governed by less-discussed but paramount material's feature: electronic dimensionality. Specifically, the electronic dimensionality surpasses the conventional classification based on the structural dimensionality, including 0D, 1D, 2D, 3D structures. It quantitatively describes the spatial connectivity and overlap of the atomic orbitals that constitute the VB maximum (VBM) and CB minimum (CBM). High electronic dimensionality, ideally approaching 3D connectivity feature, arises from extensive orbital hybridization along all the crystallographic directions. This results in isotropic band dispersion, low effective masses for both photogenerated electrons and holes, and high carriers' mobility, enabling efficient and directionally unbiased charge migration to surface reaction sites. On the contrary, semiconductor materials with low electronic dimensionality (2D, 1D, and 0D) suffer from directional orbital confinement. It can lead to the anisotropic carrier transport, pronounced band tailing, and the formation of deep-level defect states that act as recombination centers, severely compromising the PHE efficiency. Therefore, the electronic dimensionality of semiconductor photocatalyst is significantly different from its traditional structural dimensionality due to the factors like specific chemical bonding or lattice distortions that impede orbital overlap. The design of advanced photocatalysts should prioritize achieving 3D electronic connectivity within the crystal structure. This ensures delocalized band edges, minimizes the formation of deleterious deep traps, and facilitates rapid charge separation/migration, forming the electronic foundation for high-performance PHE.

2.3 Intrinsic Challenge of MS Photocatalysts: Photocorrosion

On the basis of achieving suitable bandgaps and efficient charge separation/migration, the long-term scale-up application of semiconductor photocatalysts is critically hindered by their inherent instability under light irradiation conditions, primarily due to the photocorrosion issue of MSs [108–114]. This degradation mechanism is an electrochemical corrosion process accelerated by the light irradiation during PHE. The core reaction involves the oxidation of lattice S^{2-} anions by photogenerated holes accumulated at the surface of MS photocatalysts, leading to irreversible structural destruction, generation of metal cations, formation of element sulfur, and a consequent rapid decay in PHE activity. The thermodynamic tendency for this chemical reaction is intrinsically linked to the easily destruction of the metal–sulfur bond during PHE process. Thus, the photocorrosion issue represents a fundamental stability challenge that is decoupled from, and often intensifies, limitations in charge dynamics. Only enhancing the charge separation does not inherently resolve this thermodynamic instability. Therefore, addressing photocorrosion issue requires dedicated strategies that either

 https://doi.org/10.1007/s40820-026-02111-0

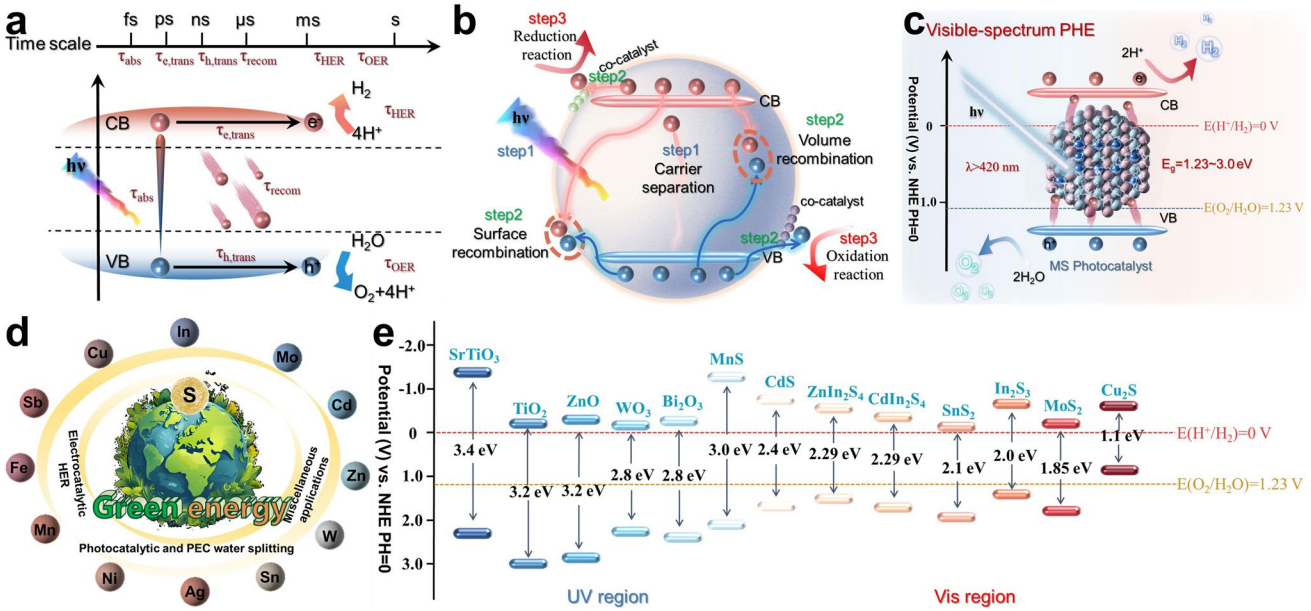

Fig. 2 Basic mechanism illustration of PHE. **a** Photogenerated charge transfer behaviors and the corresponding consuming time. Reproduced with the permission of Ref. [25] Copyright 2015, Springer. **b** Charge migration behaviors during PHE process. **c** Schematic illustration of water splitting over semiconductor photocatalysts. The corresponding overall mechanistic content includes the steps of (i) adsorption of photon leading to the exciton state; (ii) photogenerated charges' separation and migration; (iii) surface reduction in protons for HER and oxidation of water for OER. **d** Harnessing MS in the realm of renewable energy application utilizations. **e** Energy band potentials of MS photocatalyst under extensive investigation for PHE applications. Reproduced with the permission of Ref. [107] Copyright 2022, Wiley

kinetically inhibit the oxidation of S^{2-} or thermodynamically redirect photogenerated holes toward alternative, productive reaction pathways before they can attack the lattice.

3 Evolution of MS Photocatalysts: From Binary to Multinary Systems

Guided by the discussion of the fundamental requirements mentioned above, including visible-light absorption, efficient charge separation/migration, and operational photostability, the exploration progress of MS photocatalysts has undergone a significant evolution. This progression has been marked by strategic material design aimed at balancing these competing properties. The exploration began with the binary MS (BMS) such as CdS, MoS_2, PbS, ZnS, etc., owing to their structural simplicity and facile synthesis processes [107, 115–119]. These BMSs demonstrated the initial promise of MS for efficient visible-light PHE. However, their practical application revealed intrinsic limitations, which has been comprehensively summarized by Zheng et al. [120]: CdS suffers from serious photocorrosion, MoS_2 exhibits phase instability, and materials like CuS face issues with lattice mismatches in composite systems.

To overcome the intrinsic drawbacks, research advanced toward multinary MS (MMS), which offer enhanced chemical robustness, versatile elemental configurations, and tunable band structures [121–129]. Particularly noteworthy are MMS comprising group XI – XIII elements (Cu/Ag/Zn – In/Ga – S), which demonstrate exceptional solar energy harvesting capabilities, optimal bandgap energetics, and eco-compatibility, positioning them as premier platforms for efficient PHE (Fig. 2d, e) [130]. Figure 3 comprehensively summarizes the exploration process of MMS photocatalysts in the PHE application. Specifically, pioneering investigations focused on silver-based MMS photocatalysts (Ag-MMS), such as $AgGaS_2$, $AgInS_2$, $AgBiS_2$, and $AgIn_5S_8$, leveraging their eco-compatible constituents and exceptional photostability within optimal bandgap ranges for solar harvesting. Nevertheless, the thermodynamic constraints are imposed by the inherent chemical inertness of silver, hindering the fabrication of monodisperse phase-pure nanostructures.

Copper-/zinc-based MMS systems offer simplified synthesis and are promising for enhanced PHE [63]. Among these,

$CuInS_2$ and $ZnIn_2S_4$ have attracted significant interest due to their facile synthesis, suitable bandgaps (~ 1.5 and ~ 2.5 eV), and eco-friendly composition [131–133]. Notably, $ZnIn_2S_4$ has shown particular promise for efficient PHE [134–137]. To reduce reliance on expensive indium, earth-abundant alternatives such as antimony have been explored, leading to materials like $CuSbS_2$ [64, 138]. This cost-effective photocatalyst not only addresses material limitations but also exhibits considerable PHE potential. Sarilmaz et al. first reported microrod and nanodot $CuSbS_2$ for hydrogen production (Fig. 4a–d) [139]. Subsequent studies developed modified $CuSbS_2$ and heterojunctions ($CuSbS_2$/CdS and $CuSbS_2/TiO_2$) for PHE and degradation of Rhodamine B (Fig. 4e–g) [140–143]. Therefore, the progression of MS photocatalysts can be summarized as BMS of CdS, MoS_2, PbS, CuS, etc. → MMS of Cu/Ag/Zn − In/Ga − S with high-cost element → MMS of $CuSbS_2$ with low-cost elements (Fig. 5). Noticeably, MS photocatalysts generally exhibit excellent PHE performance, benefiting from their suitable electronic band structures and strong light harvesting capabilities. However, the VB potentials and interfacial kinetics of many MS systems make direct water oxidation and oxygen evolution difficult, and the photogenerated holes tend to oxidize lattice S^{2-} species, leading to severe photocorrosion [144–149]. To circumvent this issue, the sacrificial reagents, representatively Na_2S/Na_2SO_3, lactic acid, and triethanolamine, are commonly introduced to selectively consume the photogenerated holes with low oxidability, thereby facilitating the reduction half-reaction for hydrogen evolution over the MS photocatalysts.

4 Advanced Design Concept of MS Photocatalysts: 3D Electronic Dimensionality and Photocorrosion Mitigation

Throughout these investigations, the structural dimensionality, spanning from 0 to 3D architectures, has emerged as a governing factor governing PHE efficiency in MS systems [150–154]. This assertion is partially premised upon the fundamental principle that during PHE process, photogenerated electrons must efficiently migrate to active surface sites before recombination with photogenerated holes

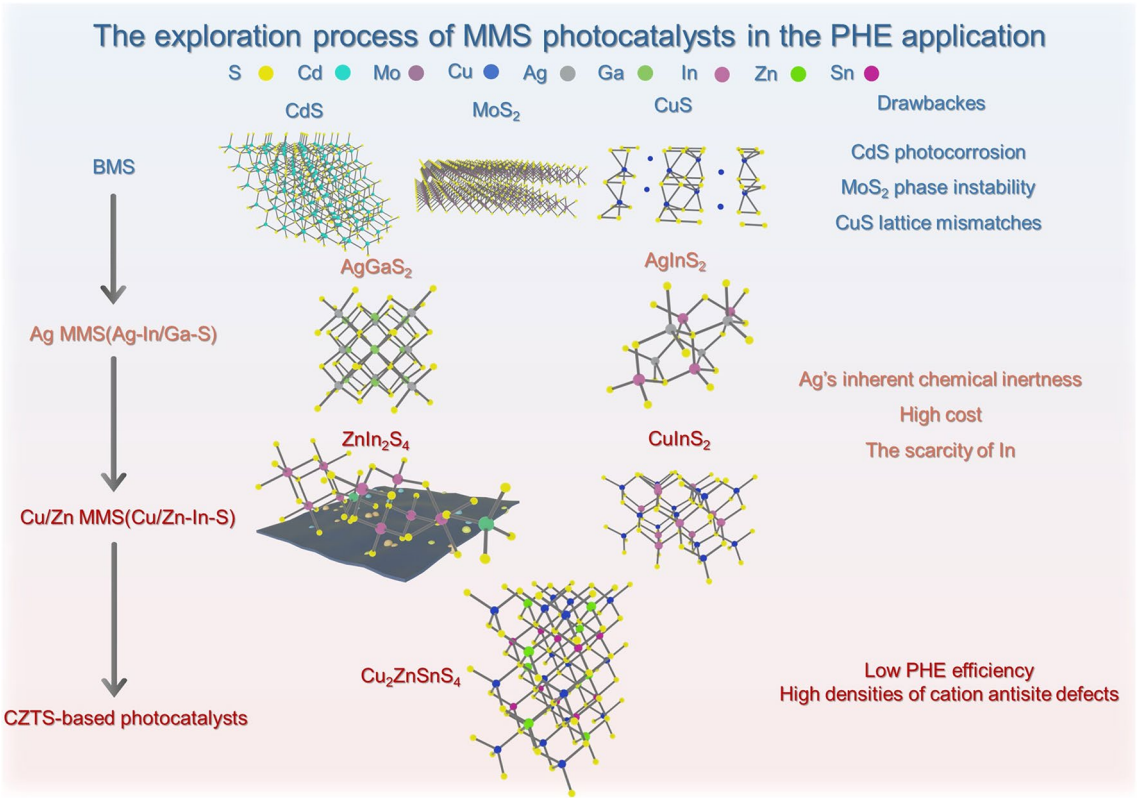

Fig. 3 Major exploration process of MMS photocatalysts in PHE application

https://doi.org/10.1007/s40820-026-02111-0

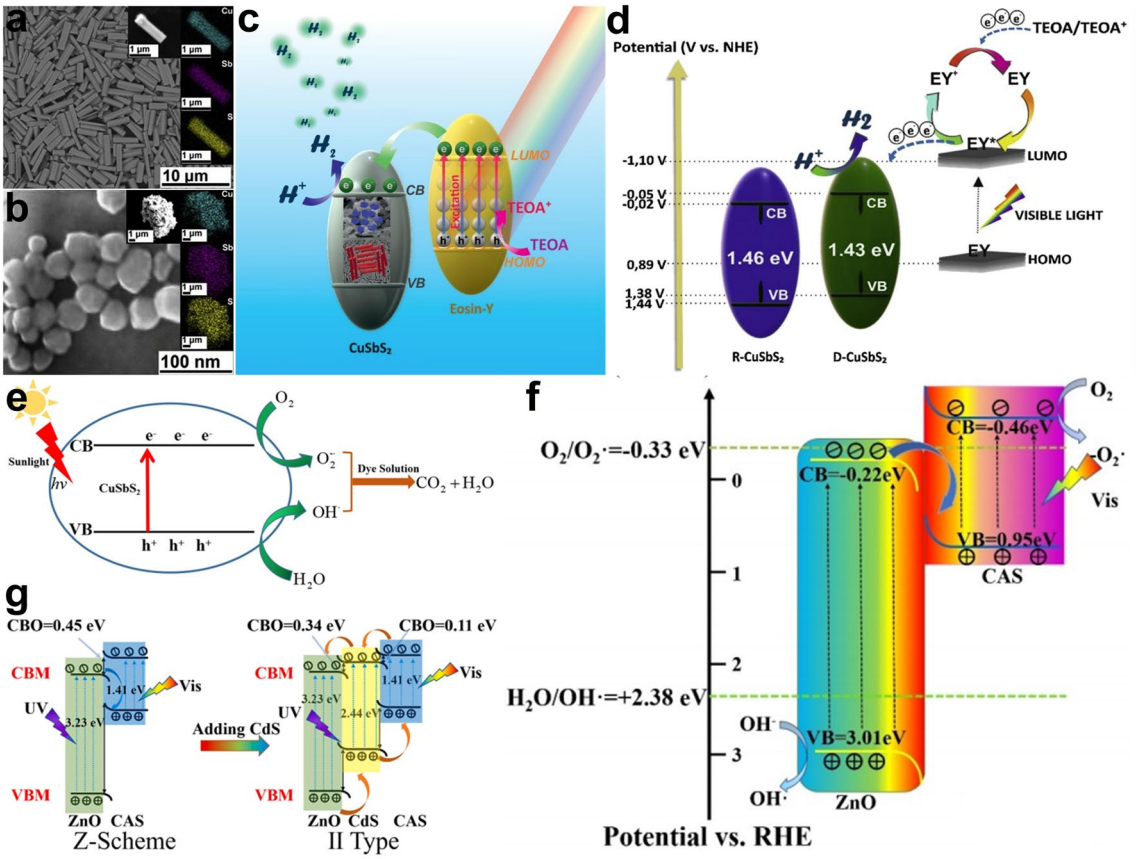

Fig. 4 **a, b** SEM image of synthesized $CuSbS_2$ photocatalyst with nanorod and nanodot morphology. **c, d** Schematic representation of the PHE mechanism mediated by $CuSbS_2$ photocatalyst. Reproduced with the permission of Ref. [139] Copyright 2020, Elsevier. **e** Operando mechanistic pathways of PD for RhB via microwave-synthesized $CuSbS_2$ nanostructures. Reproduced with the permission of Ref. [140] Copyright 2020, Springer. Interfacial charge migration modifications of $CuSbS_2$-based photocatalysts: **f** Charge carrier dynamics of photogenerated electron−hole pairs in ZnO/$CuSbS_2$ heterostructures and formation of reactive oxygen species under solar illumination. Reproduced with the permission of Ref. [142] Copyright 2022, Wiley. **g** Energy band alignment and carrier transport dynamics in $CuSbS_2$ before and after CdS incorporation, illustrating. Reproduced with the permission of Ref. [141] Copyright 2023, Elsevier

[155]. Given the stochastic grain orientation inherent in the semiconductor photocatalysts, isotropic charge migration characteristics significantly enhance the probability of electron migration to the photocatalytic active sites [156]. This section delineates cutting-edge design concept for MS photocatalysts through rigorous analysis of electronic dimensionality, a fundamental descriptor of atomic orbital connectivity forming the CBM and VBM manifolds [81]. This framework elucidates critical photophysical properties including bandgap engineering, charge carrier mobility, and defect state energetics.

4.1 Scientific Illustration of Electronic Dimensionality

Electronic dimensionality describes the degree of connectivity and overlap between the orbitals that form the VBM and CBM. This connectivity governs the spatial delocalization of the charge carriers, thereby directly influencing fundamental electronic properties such as band dispersion, effective mass, optical transition probabilities, and electronic isotropy. A higher electronic dimensionality, particularly 3D electronic network, effectively promotes enhanced carrier mobility and improved charge transport by facilitating overlapping orbital pathways. It is therefore widely recognized, through both theoretical and experimental studies, that materials exhibiting 3D electronic dimensionality generally offer superior

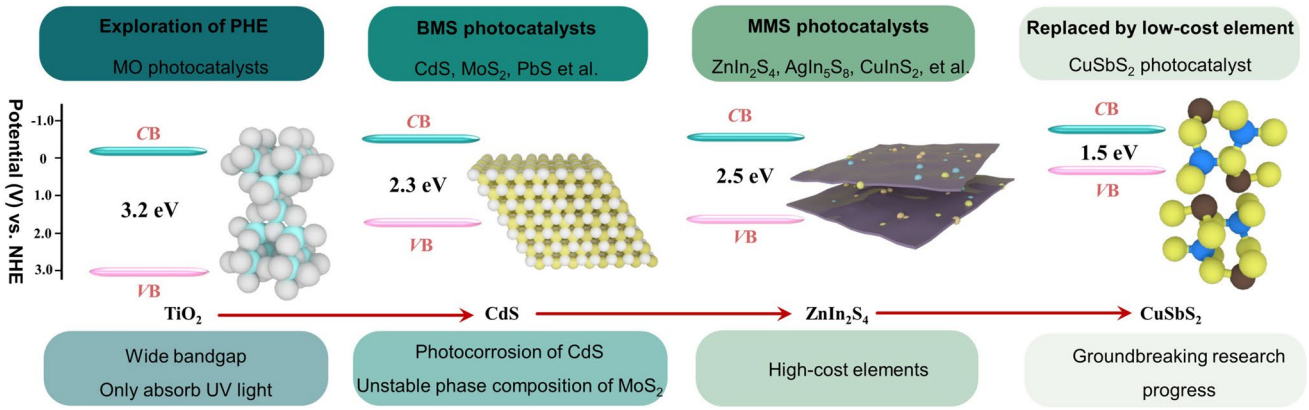

Fig. 5 Exploration route of MS photocatalysts: MO → BMS → MMS → $CuSbS_2$. The examples of each type of photocatalysts listed in the middle are: TiO_2 (MO), CdS (BMS), and $ZnIn_2S_4$ (MMS)

potential for high-performance solar-to-energy conversion. Illustratively, many leading photovoltaic semiconductors, including Si, CdTe, GaAs, Cu(In,Ga)Se_2, and perovskite, possess not only 3D crystal structures but 3D electronic connectivity [157–162], which underpins their excellent optoelectronic performance. Therefore, electronic dimensionality serves as a fundamental and predictive descriptor for understanding and tailoring the optoelectronic behavior of functional semiconductors [163]. Specifically, high electronic dimensionality, approaching 3D behavior, occurs when orbitals hybridize extensively along all crystallographic directions, enabling isotropic band dispersion, low effective carrier masses, and reduced defect-induced recombination. Conversely, low electronic dimensionality manifests as directional orbital confinement, resulting in anisotropic carrier mobility, band tailing, and deep defect states that act as nonradiative recombination centers. Crucially, electronic dimensionality may deviate significantly from structural dimensionality due to chemical substitution or lattice distortion that disrupt orbital overlap without altering the macroscopic crystal lattice topology.

In designing high-performance semiconductors for enhanced STE performance, maximizing electronic dimensionality is paramount to achieve intrinsic optoelectronic superiority. Semiconductors exhibiting high structural but low electronic dimensionality suffer from compromised charge transport (barriers to isotropic current flow) and accelerated carrier recombination [164–169], which cannot be resolved via structural optimization alone (Fig. 6a). The electronic dimensionality framework explains why certain systems exhibit anomalous bandgaps or poor STE efficiencies despite favorable structural metrics: Isolated coordination units (e.g., face-sharing bioctahedra) or cation-induced orbital decoupling impose 0D electronic character, even within nominally 3D structures. To realize efficient STE function, semiconductors should exhibit 3D electronic connectivity, ensuring delocalized band edges, shallow defect levels, and minimized carrier recombination [81]. This strategy requires selecting elements and lattice configurations that promote orbital hybridization continuity across all dimensions, transcending structural classifications to unlock optimal light harvesting and charge extraction in advanced STE materials.

Based on the excellent semiconductor properties corresponding to the 3D electronic dimensionality, Xiao et al [81] selected the perovskite $CsPbI_3$ to elucidate the importance of 3D electronic dimensionality. They systematically compared the electronic and optical properties of cesium lead iodide compounds with progressively reduced structural dimensionality (3D $CsPbI_3$, 2D Cs_2PbI_4, 1D Cs_3PbI_5, and 0D Cs_4PbI_6) and revealed how this directly translates to their respective electronic dimensionality (Fig. 6b–d). Importantly, only the structurally 3D $CsPbI_3$ perovskite exhibits a true 3D electronic dimensionality, characterized by highly dispersive CBM (primarily Pb 6*p* states) and VBM (Pb 6*s*–I 5*p* antibonding states) bands along all crystallographic directions. Consequently, $CsPbI_3$ demonstrates low, isotropic carrier effective masses, high carrier mobility in all directions, and strong, isotropic optical absorption due to the *p*-*p* transition at its 1.48 eV

 https://doi.org/10.1007/s40820-026-02111-0

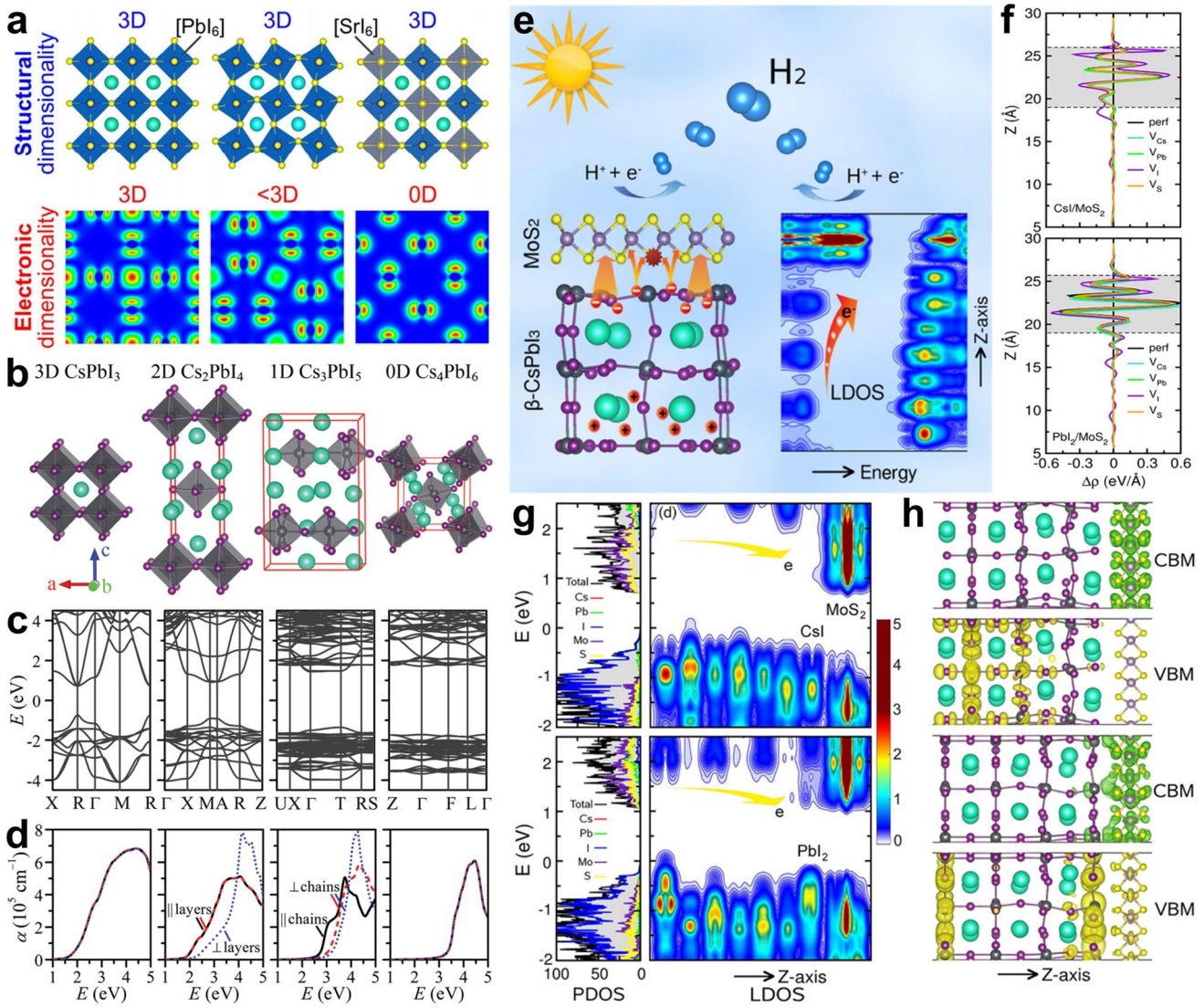

Fig. 6 **a** Visual comparison and display of structural dimensionality (above) and electronic dimensionality (below): Taking the perovskite materials as an example. **b** Theoretical crystal structure models of $CsPbI_3$, Cs_2PbI_4, Cs_3PbI_5, and Cs_4PbI_6. **c** Computed electronic band structures and **d** simulated optical absorption spectra for the corresponding cesium lead iodide model systems. Reproduced with the permission of Ref. [81] Copyright 2017, Royal Society of Chemistry. **e** PHE mechanism, charge migration behavior, and vacancy feature of $CsPbI_3/MoS_2$ heterostructure. **f** Interfacial charge redistribution: Laterally averaged electron density difference across the interfacial axis. **g** Atomic-projected DOS and *z*-axis projected local DOS isolines; **h** VBM/CBM charge density isosurfaces for CsI/MoS_2 (top) and PbI_2/MoS_3 (bottom) interfaces. Reproduced with the permission of Ref. [170] Copyright 2022, American Chemical Society

bandgap. By contrast, the cesium lead iodide compounds with lower structural dimensionality inherently possess lower electronic dimensionality due to restricted orbital connectivity. Specifically, the 2D Cs_2PbI_4 (bandgap 1.90 eV) exhibits pronounced band dispersion within the octahedral layers but negligible dispersion perpendicular thereto, leading to carrier confinement within 2D planes and highly anisotropic optical absorption. Similarly, 1D Cs_3PbI_5 (indirect bandgap 2.80 eV) exhibits dispersion only along the octahedral chains, with poor cross-chain transport. In the case of 0D Cs_4PbI_6 (bandgap 3.44 eV), fully isolated [PbI_6] octahedra, displays completely flat (non-dispersive) bands in all directions, confirming its 0D electronic dimensionality. This fundamental lack of orbital connectivity results in large effective masses, poor carrier mobility, and a significantly widened bandgap. Therefore,

the comparative analysis across 3D $CsPbI_3$, 2D Cs_2PbI_4, 1D Cs_3PbI_5, and 0D Cs_4PbI_6 conclusively demonstrates that electronic dimensionality, defined by the spatial connectivity of the atomic orbitals forming the band edges, which is intrinsically linked to structural dimensionality in these model systems and is the primary factor governing critical STE properties like bandgap size, carrier mobility, and optical absorption anisotropy. Accordingly, the 3D electronic dimensionality $CsPbI_3$-based materials have been recently applicated in efficient PHE [170–173]. Especially, Ri et al. engineered a $CsPbI_3/MoS_2$ heterostructure photocatalyst, achieving enhanced PHE performance through rigorous first-principles analysis of interfacial defect dynamics [170]. The authors reveal that interfacial iodine vacancies in $CsPbI_3/MoS_2$ heterostructures enhance charge separation by amplifying interface dipole moments (Fig. 6e, f), while sulfur vacancies introduce mid-gap traps (Fig. 6g). Type-II band alignment facilitates electron transfer to MoS_2 (Fig. 6h), leveraging the high electronic dimensionality of $CsPbI_3$ for directional carrier migration. Thus, systematic interrogation of $CsPbI_3$'s 3D electronic dimensionality, coupled with its exemplary performance in PHE, provides dual theoretical and experimental guidance for advanced design concept of MS photocatalyst, offering profound implications for next-generation photocatalyst engineering.

On a deeper level, the excellent performance endowed by 3D electronic dimensionality originates from several intertwined microscopic mechanisms that collectively optimize the key steps in PHE at the atomic and orbital levels. Fundamentally, the extension of the orbital hybridization along all crystallographic directions can create spatially delocalized band edges, which directly reduces the effective masses of both photogenerated electrons and holes. This isotropic band dispersion enables rapid and directionally uniformed charge migration, thus minimizing the migration time of photogenerated carriers to surface reaction sites and suppressing bulk/surface recombination. Furthermore, the continuous orbital network inherent to 3D electronic connectivity also favors the formation of shallow defect states, as opposed to deep-level traps (non-radiative recombination centers). Such excellent defect properties are crucial for maintaining high carrier concentrations and longevity during the PHE process. From the dynamic perspective, the highly dispersive VB and CB effectively enhance the optical transition matrix elements, leading to strong and broad light absorption across the visible-light spectrum. Meanwhile, the delocalized charge density at band edges also effectively facilitates efficient interfacial charge transfer by lowering the energy barrier for carrier injection into the reactive sites. Essentially, the 3D electronic dimensionality orchestrates a synergistic interplay among enhanced light harvesting, accelerated bulk charge migration, inhibited recombination, and favorable surface reaction kinetics. These essential factors jointly constitute the fundamental basis for the dramatic improvements in PHE performance observed in MS photocatalysts.

4.2 Quantitative and Semi-Quantitative Parameters for Determining Electronic Dimensionality

While the conceptual framework of electronic dimensionality is powerful for rationalizing the properties of semiconductor material, its actual application greatly relies on clear methodologies for its determination and characterization. Unlike the structural dimensionality directly accessible via diffraction techniques, electronic dimensionality is an emergent quantum property inferred from the accurate electronic structure analysis. Its assessment depends on the multi-faceted suite of computational and experimental descriptors that move beyond qualitative inspection toward the quantitative or semi-quantitative evaluation (Fig. 7) [174–176].

The most fundamental evidence originates from the first-principles calculations of the electronic structure. The spatial delocalization of charge density associated with the VBM and CBM serves as the primary visual indicator: The true 3D electronic connectivity exhibits as continuous, 3D networks of charge density throughout the lattice, whereas lower dimensions exhibit confinement to the planes, chains, and isolated clusters. More quantitatively, the dispersion of key bands, particularly those forming the band edges, is also a critical metric. For instance, in the halide systems, the bandwidth of the σ* CB has been directly correlated with electronic dimensionality, where broader bandwidths signify higher dimensionality and greater orbital overlap [174]. At the same time, this also translates into the effective masses of the carriers. Materials with 3D electronic dimensionality are characterized by low, isotropic effective masses for both electrons and holes, as derived from the band curvature. Significantly anisotropic or high effective masses are the negative factors for reducing the dimensionality, indicating the constrained carrier motion [176]. Moreover, these

 https://doi.org/10.1007/s40820-026-02111-0

calculated and computational parameters have direct experimental correlates. The anisotropy in optical absorption spectra, calculated or measured with the polarized light, directly reflects the underlying electronic anisotropy. As a result, the semiconductor material with 3D electronic connectivity exhibits relatively isotropic absorption above the bandgap, while lower dimensionality leads to the strong polarization dependence, typically strong in-plane versus weak out-of-plane absorption [81]. Furthermore, the photophysical properties of emissive centers can act as the sensitive probes of inter-site coupling and, by extension, electronic dimensionality. On the basis of nominally isolated structural units, the degree of the photoluminescence (PL) concentration quenching, carriers' lifetime, and quantum yield greatly depend on the electronic coupling between these units. The weak coupling (low electronic dimensionality) minimizes concentration quenching, while enhanced coupling (3D electronic dimensionality) facilitates energy transfer and quenching and thus provides an indirect spectroscopic measure of orbital overlap [175].

Beyond accurate density functional theory (DFT) calculations, the innovative crystal structure-based analysis tools also offer rapid, semi-quantitative assessment. Representatively, the Voronoi polyhedron (VP) method, which separates space based on the atomic distances, can quantify noncovalent interactions between the neighboring coordination units. Specifically, by analyzing the faces shared between the VPs of atoms on the neighbor structural units, one can map the strength and dimensionality of the orbital overlap pathways. Significant shared-face areas indicate strong interunit coupling and higher electronic dimensionality, even in 0D structural materials, whereas isolated VPs confirm the true electronic isolation [175]. Therefore, this geometric approach also provides a valuable pre-screening tool independent of demanding the electronic calculations. At the same time, the emerging concept of fractional or non-integer electronic dimensionality is also crucial for understanding the complex systems, typically disordered alloys or imperfect networks. In this case, the electronic connectivity may not be uniformly 3D, 2D, or 1D but exist in a middle state. A comprehensive evaluation demands integrating qualitative orbital connection maps along with quantitative measures of covalent bond strength, such as the integrated crystal orbital Hamilton population (ICOHP) integrated up to the Fermi level (E_F). The distribution and strength of the key bonds, typically the metal-anion, along different crystallographic directions dictate the degree of carrier delocalization and anisotropy in each direction, leading to the map with minor difference that governs properties like directional effective masses and absorption [176].

Therefore, determining the electronic dimensionality of a semiconductor material is not reliant on a single parameter but on a convergent analysis of the multiple indicators: calculated band dispersion and charge density topology → derived effective masses and optical anisotropy → experimentally accessible photophysical responses → insightful geometric analysis of the crystal structure. This multi-faceted characterization framework effectively transforms electronic dimensionality from a qualitative concept into a strong and feasible guideline for predicting and engineering effective charge migration and optoelectronic functionality in advanced MS semiconductors.

4.3 Advanced MS Photocatalyst with 3D Electronic Dimensionality

As detailed in Sect. 3, the $CuSbS_2$ MMS photocatalyst represents a methodological advancement in MS photocatalysts for PHE, emanating from strategic cationic substitution of Sb for In within the $CuInS_2$ lattice (Fig. 8a–c and left part in Fig. 8d) [138, 177]. Notably, lead halide perovskites such as $CH_3NH_3PbI_3$ demonstrate that Pb^{2+} with its $6s^2$ lone pair enables the stabilization of 3D crystal frameworks, giving rise to highly connected electronic structures. This electronic characteristic favors the formation of rocksalt-type structures with octahedral coordination [178–186]. Consistent with this trend, the incorporation of PbS into the layered compound $CuSbS_2$ induces a structural reconstruction, yielding the formation of $CuPbSbS_3$ which adopts a 3D crystalline architecture. This unique attribute facilitates structural reconstruction of layered MS into ternary 3D frameworks through PbS incorporation [187–190]. Exemplifying this paradigm, integration of PbS into the layer $CuSbS_2$ lattice yields 3D bournonite $CuPbSbS_3$ (Fig. 8d), as validated across multiple experimental studies [191–193].

Building upon this foundation, our group systematically interrogate the electronic dimensionality of $CuPbSbS_3$ through DFT calculations [194], a conceptual framework directly extending the 3D electronic dimensionality paradigm established for $CsPbI_3$. Computational analyses unequivocally demonstrate that the $CuPbSbS_3$ exhibits 3D

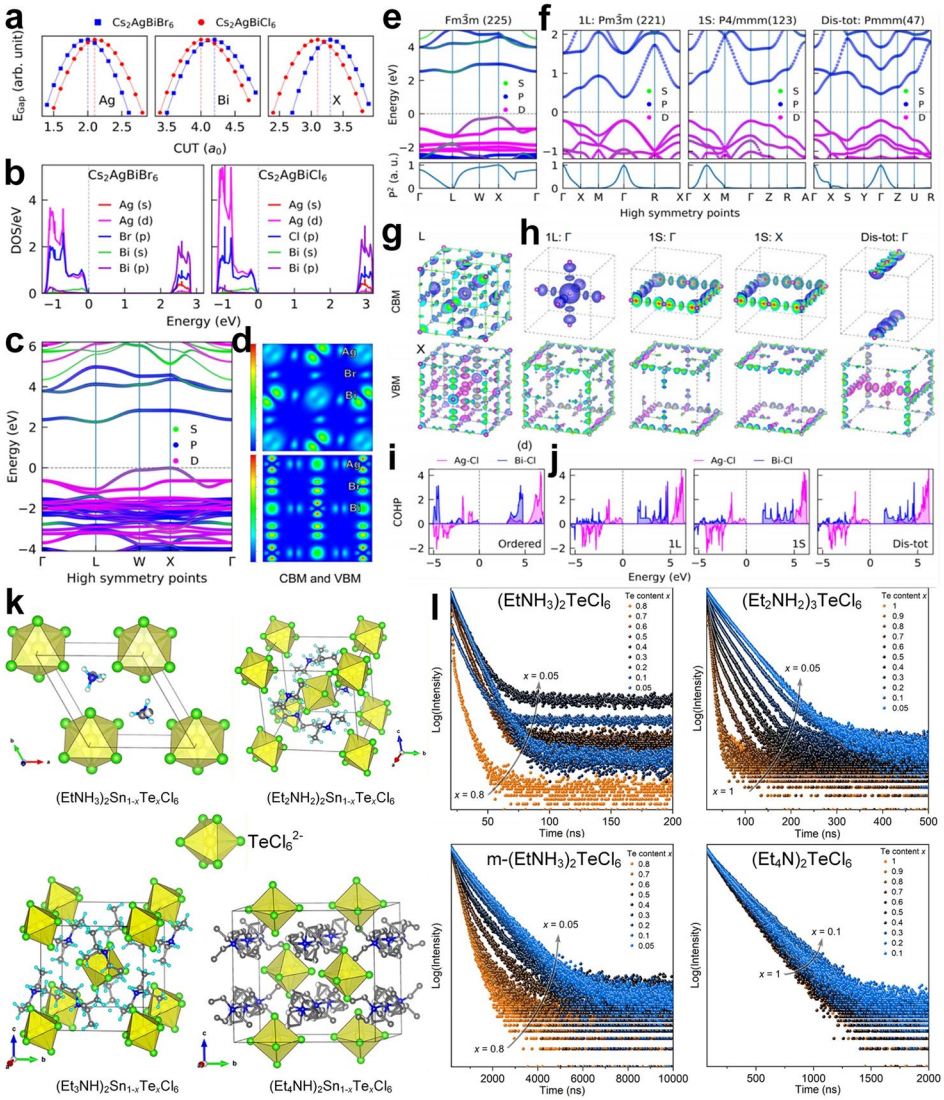

Fig. 7 Computational determination and characterization of electronic dimensionality in the halide double perovskite models, illustrating the key parameters and analyses used to assess the electronic dimensionality of Cs_2AgBiX_6 (X = Br, Cl) systems, and comparing ordered and cation-disordered structures: **a** Determination of the optimal cut-off parameter for self-energy potential corrections in the DFT-1/2 method. **b** DOS and **c** orbital-projected band structure for ordered $Cs_2AgBiBr_6$, calculated with DFT-1/2 method (The VBM is set to zero energy). **d** Iso-surface plots of the orbital densities for the CBM (top) and VBM (bottom) in ordered $Cs_2AgBiBr_6$, viewed along (100) direction of the cubic unit cell, revealing the spatial confinement of charge carriers. Orbital-projected electronic band structures calculated using the DFT-1/2 method for **e** the ordered phase and **f** representative cation-disordered configurations (1L, 1S, Dis-tot) (The E_F is set to 0 eV). **g, h** Corresponding orbital density isosurfaces for the CBM (top) and VBM (bottom) at high-symmetry points, illustrating the spatial distribution of the band-edge states. ICOHP analyses for Ag–Cl and Bi-Cl interactions that dominate the band edges in **i** ordered and **j** disordered systems. Positive ICOHP values denote the antibonding character, whereas negative values indicate the bonding interactions (The VBM is aligned at 0 eV). These plots collectively provide a multi-parameter assessment, including the band dispersion, orbital delocalization, and bond-resolved interaction strengths, to quantify the evolution of electronic dimensionality from a low-dimensional confined state in the ordered material toward enhanced 3D connectivity in disordered variants. Reproduced with the permission of Ref. [176] Copyright 2024, Royal Society of Chemistry. Illustrative overview methods for the determination of the electronic dimensionality in semiconductor materials: **k** Crystal structures of hybrid tellurium halides $(Et_nNH_{4-n})_2TeCl_6$ (n = 1–4), showing isolated $TeCl_6^{2-}$ octahedra (yellow) surrounded by progressively larger organic cations (C: gray, N: blue, H: light blue, Cl: green). The increasing cation size reduces the inter-octahedral orbital overlap, effectively lowering electronic dimensionality. **l** Corresponding TRPL decay profiles of solid solution systems $(Et_nNH_{4-n})_2Sn_{1-x}Te_xCl_6$ under 372 nm excitation. The PL lifetime and quenching behavior vary systematically with organic cation size and Te content, reflecting changes in the electronic coupling between neighboring Te centers. Shorter lifetimes and stronger concentration quenching in systems with smaller cations ($EtNH_3^+$) indicate higher electronic dimensionality and enhanced inter-site energy transfer, whereas larger cations (Et_4N^+) lead to the longer lifetimes and weaker quenching, consistent with the behavior of electronically isolated 0D. Together, these structural and photophysical analyses provide multi-faceted basis for quantifying electronic dimensionality, linking the geometric arrangement, orbital overlap, and optoelectronic response. Reproduced with the permission of Ref. [175] Copyright 2024, American Chemical Society

 https://doi.org/10.1007/s40820-026-02111-0

electronic dimensionality alongside its structural framework, surpassing the optoelectronic limitations inherent to layered $CuSbS_2$. As shown in Fig. 8e, the latter manifests an indirect Heyd–Scuseria–Ernzerhof-calculated (HSE-calculated) bandgap of 1.56 eV, aligning with experimental reports (approximately 1.5 eV) [195–198]. This characteristic, prevalent in lone-pair cation-based layered chalcogenides, impedes efficient carrier transport due to phonon-assisted recombination [199], fundamentally constraining the efficiency of PHE. In stark contrast, the $CuPbSbS_3$ achieves a direct band transition at the Γ point (HSE: 1.61 eV), with VB/CB extrema exhibiting synergistic orbital hybridization. The observed bandgap overestimation relative to experimental values (1.20 − 1.31 eV) stems from methodological exclusion of spin–orbit coupling (SOC), a critical perturbation for heavy post-transition elements. SOC effects intrinsically reduce bandgaps by lifting orbital degeneracies through *j-j* coupling and enhancing VB dispersion via *p*-orbital splitting. Crucially, 3D electronic connectivity in $CuPbSbS_3$ enables isotropic carrier mobility (> 150 $cm^2\ V^{-1}\ s^{-1}$) [194] and attenuates defect-assisted recombination, whereas layered $CuSbS_2$ suffers from anisotropic transport ($\mu < 30\ cm^2\ V^{-1}\ s^{-1}$) [200] and deep-level traps. This electronic dimensionality transition, facilitated by PbS integration, elevates optical absorption coefficients by > 300% across visible spectra while reducing exciton binding energies to < 20 meV, parameters essential for high-efficiency STE conversion. Incorporating SOC reduces the bandgap of $CuPbSbS_3$ to 1.29 eV (Fig. 8f, red arrow), primarily due to degeneracy lifting within Pb 6*p* orbitals that lowers the CBM. Furthermore, the $Pmn2_1$ structure enables significant Rashba splitting under SOC, lifting spin degeneracy and inducing momentum-offset band bifurcation. Consequently, the CB edge experiences minor Γ-point displacement, yielding a weakly indirect fundamental gap of 1.29 eV. Notably, the Rashba effect, implicated in prolonged carrier lifetimes within MS photocatalysts [201–203], suggests analogous benefits for $CuPbSbS_3$ PHE performance. Projected density of states (DOS) analysis (Fig. 8g) reveals VB/CB extrema comprising hybridized antibonding states: S 3*p* coupled with Cu 3*d*/Pb 6*s*/Sb 5*s* orbitals at VBM, versus Cu 4*s*/Pb 6*p*/Sb 6*p* with S 3*p* orbitals at CBM. This pan-lattice orbital involvement confirms 3D electronic connectivity. Consequently, isotropic band dispersion facilitates efficient ambipolar charge transport.

The superior defect properties associated with the 3D electronic dimensionality have also been confirmed in $CuPbSbS_3$. Quaternary compounds such as kesterite CZTS (mentioned in Sect. 1) exhibit propensity for deep-level cation antisite defects due to isomorphic coordination environments among Cu/Zn/Sn. This disorder is mitigated in Cu_2BaSnS_4, in which the steric differentiation between large Ba^+ occupying $[Ba(S/Se)_8]$ polyhedra and tetrahedral SnS_4 units thermodynamically suppresses cation exchange. Analogously, $CuPbSbS_3$ features divergent coordination geometries (Fig. 8d) arising from distinct valence states (Cu^+/Pb^{2+}/Sb^{3+}), consequently eliminating this defect pathway through inherent chemical incompatibility. Figure 9a shows the charge-state transition levels for intrinsic point defects in $CuPbSbS_3$. Six low-formation-energy ($\Delta H_f < 1$ eV) defects dominate: Cu_i, Cu_{Pb}, Pb_{Sb}, Sb_{Pb}, V_{Pb}, and V_{Cu}. Conversely, deep-level defects (V_{Sb}, Pb_i, S_{Pb}, and V_S) exhibit prohibitively high ΔH_f (> 1 eV), limiting concentrations to $10^6\ cm^{-3}$ (room temperature) and $10^{14}\ cm^{-3}$ (600 K quenched). Crucially, all dominant defects are shallow, V_{Pb}, V_{Cu}, Cu_{Pb}, and Pb_{Sb} acting as acceptors; Cu_i and Sb_{Pb} as donors, signifying intrinsic defect tolerance essential for high-efficiency PHE.

The formation enthalpies of intrinsic defects, consequently the equilibrium E_f, exhibit pronounced dependence on synthetic chemical potentials. Figure 9b–d illustrates the ternary chemical space of $\Delta\mu_{Cu}$, $\Delta\mu_{Pb}$, and $\Delta\mu_{Sb}$ under three sulfur regimes: sulfur-rich, sulfur-moderate, and sulfur-poor. Under sulfur-rich conditions, the E_f resides within the *p*-type region. At chemical coordinate 4 (Fig. 9e), E_f stabilizes 0.38 eV above the VBM, a regime conferring optimal weak *p*-type conductivity for photovoltaic operation. Progressive sulfur depletion shifts E_f toward mid-gap (coordinate 1 in Fig. 9f), driven by enhanced formation of *n*-type Sb_{Pb} donors concurrent with suppressed generation of compensating acceptors (Cu_{Pb}, V_{Cu}, and Pb_{Sb}). At intermediate sulfur activity (coordinate 45 in Fig. 9g), E_f traverses mid-gap by a marginal 0.07 eV, yet the resultant electron concentration ($n \approx 10^9\ cm^{-3}$) falls below Hall-effect detection thresholds. Further reduction to sulfur-poor conditions fails to induce measurable *n*-type conduction; instead, E_f reverts to 0.62 eV above VBM (Fig. 9h) due to the thermodynamic inhibition of Sb_{Pb} formation. This defect chemistry landscape reveals tunable semiconducting behavior: weak *p*-type (sulfur-rich) transitions to intrinsic character under sulfur-moderate/sulfur-poor conditions. Crucially, sulfur-rich synthesis emerges as the singular pathway to achieve technologically viable

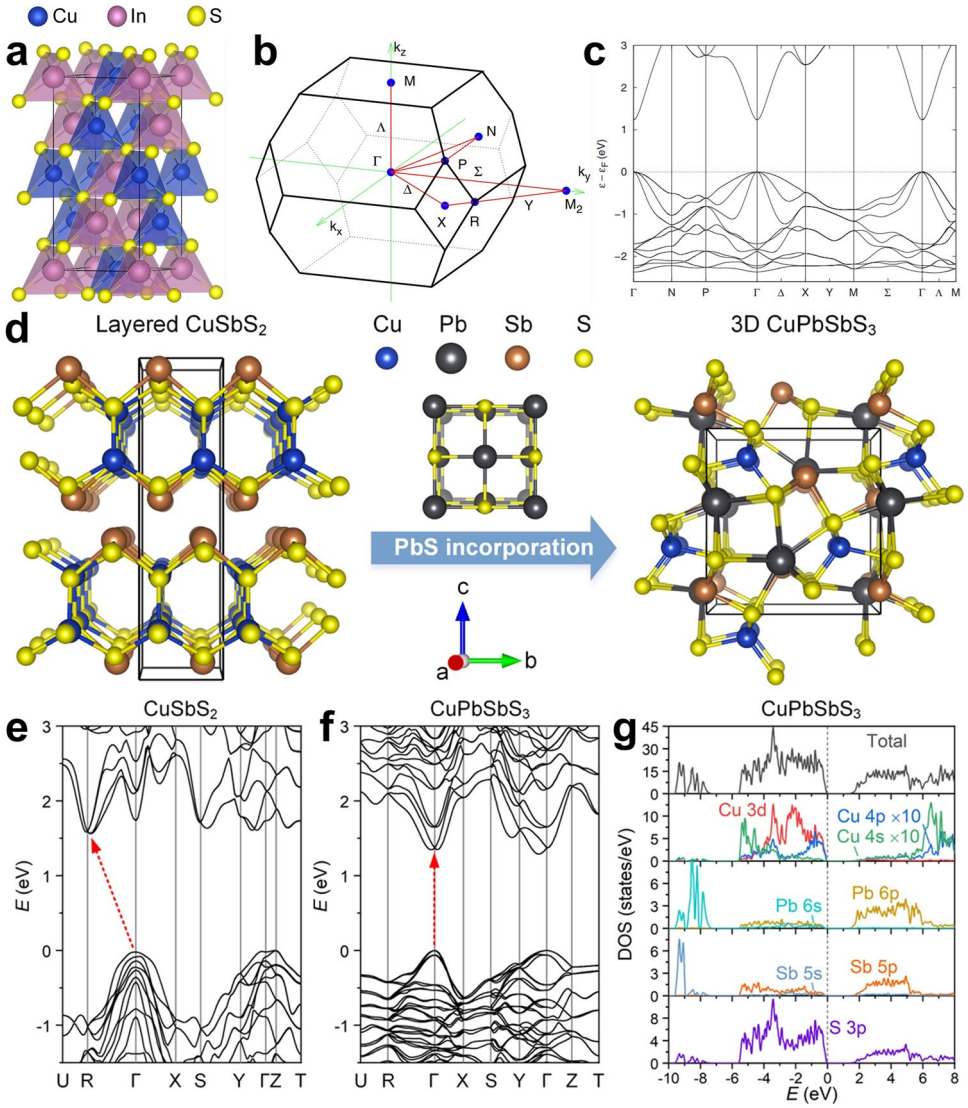

Fig. 8 **a** Crystal structure of $CuInS_2$ with typical tetragonal chalcopyrite phase. Reproduced with the permission of Ref. [87] Copyright 2023, Elsevier. **b** Brillouin zone, and **c** theoretical calculated band structure of $CuInS_2$. Reproduced with the permission of Ref. [177] Copyright 2015, American Physical Society. **d** Structural evolution from layered $CuSbS_2$ (left part) to 3D $CuPbSbS_3$ (right part) via PbS intercalation (middle part). **e** HSE-calculated band dispersion of $CuSbS_2$. **f** SOC-HSE band structure of $CuPbSbS_3$. **g** Total/projected DOS for $CuPbSbS_3$ under HSE + SOC formalism (Cu 4*s*/4*p* orbitals amplified 10×). Reproduced with the permission of Ref. [194] Copyright 2020, Elsevier

hole concentrations ($p \approx 10^{16}$ cm^{-3}) while maintaining high hole mobility. Such defect feature, suppressing deep traps while enabling shallow acceptor dominance, constitutes a critical enabler for efficient PHE in $CuPbSbS_3$-based photocatalysts.

4.4 General Photocorrosion of MS Photocatalysts

Based on the above discussion, it has been ascertained that the advanced design concept of the 3D electronic dimensionality can effectively guide the design and development of MS photocatalysts with superior PHE performance. Despite significant advances in the rational design of MS photocatalysts through 3D electronic dimensionality (especially $CuPbSbS_3$), these materials remain intrinsically susceptible to photocorrosion issue, a critical degradation

 https://doi.org/10.1007/s40820-026-02111-0

pathway wherein photogenerated holes oxidize lattice S^{2-} ions [204–208]. Specifically, photocorrosion represents a pervasive challenge that severely compromises the structural integrity and catalytic durability of MS photocatalysts. This issue primarily arises from two interrelated pathways: oxidation by photogenerated holes and reaction with the surrounding medium. Upon light irradiation during PHE, photogenerated holes accumulate on the surface of MS, where they oxidize S^{2-} to elemental sulfur or soluble sulfate species, thereby destroying the material. As a representative instance, in CdS, this process can be described as $CdS + 2\ h^+ \rightarrow Cd^{2+} + S$. Concurrently, dissolved oxygen in the aqueous environment acts as an aggressive oxidant, reacting with the photocatalyst to form metal ions and sulfate, further accelerating the destruction. The corresponding key reactions include $CdS + O_2 + 4\ h^+ + 2H_2O \rightarrow Cd^{2+} + S$

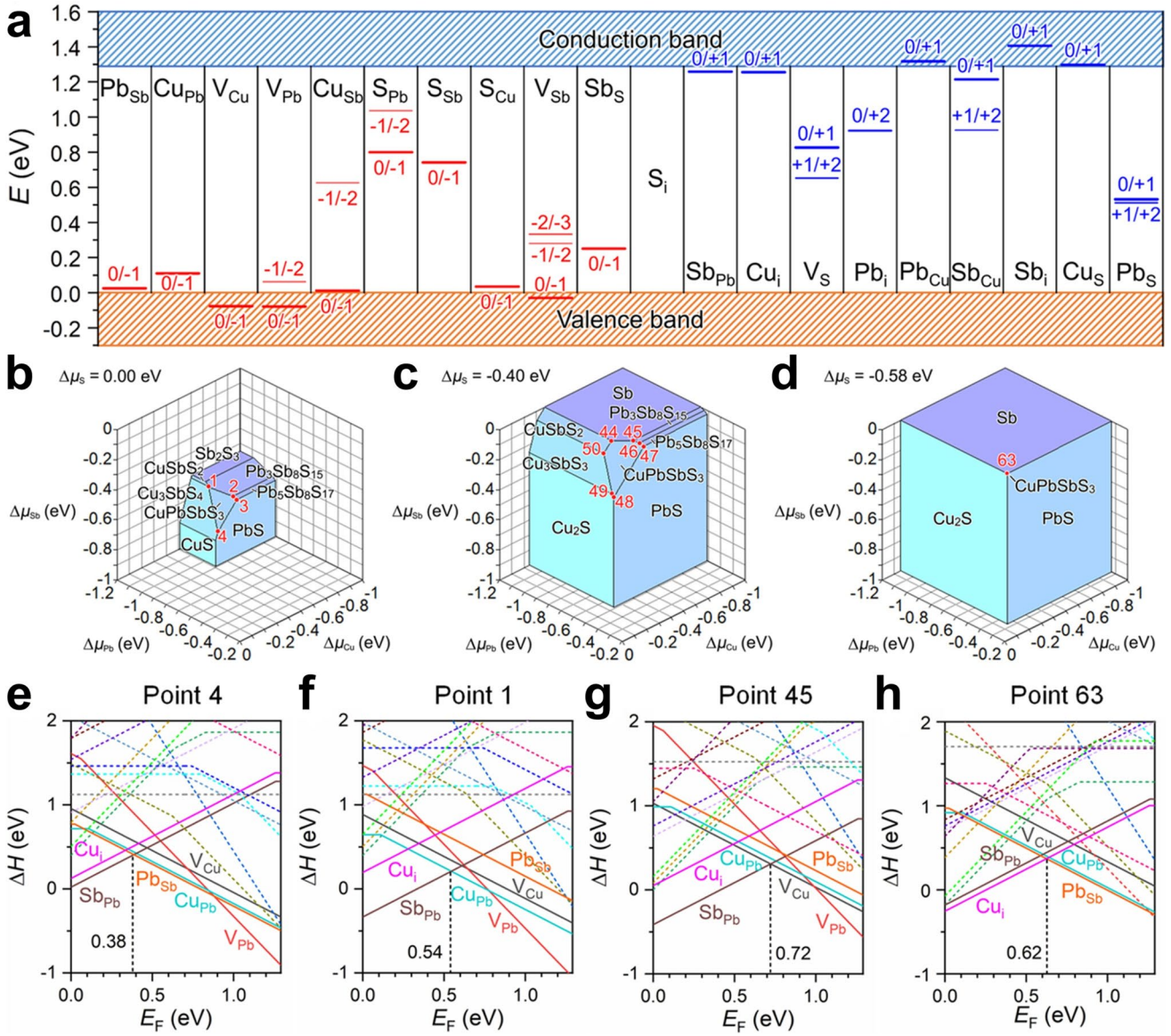

Fig. 9 **a** Charge-state transition levels of intrinsic defects in $CuPbSbS_3$, derived from DFT calculation. **b–d** 3D visualizations of chemical potentials of $\Delta\mu_{Cu}$, $\Delta\mu_{Pb}$, and $\Delta\mu_{Sb}$ across the Cu–Pb–Sb–S quaternary system, evaluated under discrete $\Delta\mu_{Sb}$ values corresponding to sulfur-rich, sulfur-moderate, and sulfur-poor regimes. **e–h** Formation enthalpies of intrinsic defects in $CuPbSbS_3$ as functions of E_f, computed at designated chemical potential points 4, 1, 45, and 63. Reproduced with the permission of Ref. [194] Copyright 2020, Elsevier

$O_4^{2-} + 4H^+$. The synergistic effect of hole-induced oxidation and oxygen-mediated corrosion leads to irreversible structural damage, metal leaching, and significant loss of photocatalytic activity. A profound understanding of these dual mechanisms is essential for designing advanced MS photocatalyst with long-term operational stability. While electronic dimensionality optimization enhances charge separation kinetics and spectral responsiveness, it does not inherently resolve the thermodynamic instability of metal–sulfur (M–S) bonds under photoexcitation. Consequently, even state-of-the-art architectures experience performance decay, undermining their viability for scalable solar fuel production where operational longevity is paramount. Current reliance on sacrificial electron donors (Na_2S/Na_2SO_3, methanol, and triethanolamine) represents a pragmatic yet fundamentally limited approach [201, 209]: Although hole scavenging temporarily stabilizes sulfides, it forfeits energy-storing potential by producing solar energy into chemically inert oxidation products instead of value-added reductants.

This intrinsic trade-off between photostability and PHE efficiency underscores the necessity for innovative stabilization strategies beyond conventional sacrificial chemistry. Merely suppressing photogenerated hole-induced photocorrosion through thermodynamic downhill reactions represents a suboptimal utilization of photonic energy input. To fully harness the benefits conferred by advanced electronic dimensionality control, including enhanced carrier mobility and tailored band alignment, complementary approaches must be developed to either kinetically inhibit sulfur oxidation or thermodynamically redirect hole consumption toward productive reactions. Such methodologies should ideally operate without compromising the redox potential required for target processes like hydrogen evolution. The pursuit of corrosion-mitigating interfaces, kinetic passivation layers, or selective photogenerated hole-transfer pathways thus emerges as an essential frontier in MS photocatalyst engineering. Only by synergistically integrating electronic structure design and corrosion suppression mechanisms can these materials achieve the dual benchmarks of long-term operational robustness and maximal solar energy conversion efficiency demanded by industrial implementation.

5 Advanced MS Photocatalysts in PHE Application

Based on the preceding discussion and summarization, the unique 3D electronic dimensionality characteristics of $CuPbSbS_3$ have been rigorously established and validated in prior research. Consequently, leveraging this advanced electronic dimensionality design concept, the transition from $CuSbS_2$ to $CuPbSbS_3$ represents a landmark leap in the development of MS photocatalysts. More recently, our group has implemented the synthesized advanced MS photocatalyst of $CuPbSbS_3$ to PHE through a concerted theoretical/experimental approach. Concurrently, addressing the inherent challenge of photocorrosion in MS photocatalysts, we have pioneered the development of corresponding mitigation strategies. In this section, we systematically review the recent advances in the PHE application of state-of-the-art 3D electronic dimensionality $CuPbSbS_3$ photocatalyst, alongside effective solutions to the photocorrosion issue in MS photocatalysts. This will serve to precisely delineate the design concept and practical implementation of advanced MS photocatalysts.

5.1 Application of 3D Electronic Dimensionality: The Case of $CuPbSbS_3$

The exploration and development of bournonite $CuPbSbS_3$ represent a milestone in the rational design of MS photocatalysts with 3D electronic dimensionality. This section systematically outlines the synthesis, structural characteristics, and PHE performance of $CuPbSbS_3$, followed by its innovative integration with ferroelectric materials to enable efficient piezo-photocatalytic degradation (piezo-PD), thereby illustrating the versatility of 3D electronic dimensionality in multifunctional photocatalytic systems.

5.1.1 Synthesis, Structural Integrity, and PHE Performance

The experimental $CuPbSbS_3$ photocatalyst was successfully synthesized via a butyldithiocarbamate acid (BDCA) solution method (Fig. 10a), yielding phase-pure powders with a predominant (002) crystal orientation [210]. Structural characterization by transmission electron microscopy

 https://doi.org/10.1007/s40820-026-02111-0

(TEM) and high-resolution TEM (HRTEM) revealed a stacked-flake morphology and well-defined lattice fringes consistent with the bournonite structure. Energy-dispersive X-ray spectroscopy (EDS) mappings confirmed homogeneous distribution of all constituent elements, underscoring excellent stoichiometric control. Under simulated solar irradiation, the 3D electronic dimensionality $CuPbSbS_3$ exhibited a remarkable PHE rate of 250.8 μmol g^{-1} h^{-1} in the absence of cocatalysts, a performance surpassing that of established MS photocatalysts such as CZTS nanorods and $ZnIn_2S_4$, and competitive with state-of-the-art heterojunctions like $ZnIn_2S_4/TiO_2$ (Fig. 10b). More importantly, the material demonstrated exceptional photostability, with only about 18% decline in activity over 12 h of continuous PHE process, attributable to its robust 3D electronic structure and minimized photocorrosion. The electronic band structure of $CuPbSbS_3$, as probed by X-ray photoelectron spectroscopy VB (XPS-VB) and UV–vis spectra, revealed the VB potential of 0.54 eV vs. NHE and a direct bandgap of 1.38 eV, positioning the CB at − 0.84 eV, thermodynamically favorable for proton reduction (Fig. 10c). DFT calculations further elucidated the 3D electronic connectivity within the bournonite framework, characterized by corner-sharing $[MX_6]$ octahedra (Fig. 10d). The ΔG_{H^*} calculations on the (002) surface identified several sulfur sites (S1 and S4) with near-ideal ΔG_{H^*} values (− 0.06 to − 0.08 eV), facilitating the efficient HER kinetics (Fig. 10e–g).

Guided by the electronic dimensionality design paradigm, this study not only establishes $CuPbSbS_3$ as a promising photocatalyst for PHE but highlights the critical roles of electronic dimensionality and surface engineering in optimizing catalytic performance. The electronically 3D nature of $CuPbSbS_3$ ensures robust charge carrier mobility, while the exposed (002) facet with abundant low-energy catalytic sites enables efficient PHE. These findings pave the way for developing $CuPbSbS_3$-based heterojunctions and composite systems, holding great promise for advancing sustainable hydrogen production technologies.

5.1.2 Integration with $BaTiO_3$ for Enhanced Piezo-Photocatalysis

Ferroelectric materials are characterized by their noncentrosymmetric crystal structures and the presence of the spontaneous polarization [211–215]. This intrinsic property allows the polarization direction to be switched under the influence of external condition, typically electric field or mechanical stress [216–218]. As a result, these materials offer unique advantages in the electronic and optoelectronic applications. Recently, low-dimensional ferroelectrics have garnered significant research attention due to the synergistic coupling between their piezoelectric/ferroelectric behavior and semiconductor properties, positioning them as promising candidates for semiconductor-based photocatalysis [219]. A representative example is perovskite-type $BaTiO_3$, which has been widely investigated owing to its inherent piezoelectric and pyroelectric characteristics [220–222]. Recently, increasing efforts have been devoted to leveraging the cooperative effects between $BaTiO_3$ and MS semiconductor photocatalysts [223–227]. Such heterostructures enable the enhancement of optoelectronic carrier dynamics through the modulation of interfacial temperature or the application of mechanical deformation. The spontaneous polarization in ferroelectric materials further induces a built-in electric field, offering a viable strategy for designing advanced photocatalytic systems that harness piezoelectric and thermoelectric optoelectronic effects.

The successful exploration of $CuPbSbS_3$ based on 3D electronic dimensionality design concept, coupled with its demonstrated efficacy in PHE, has catalyzed significant research interest in its broader photocatalytic applications. Building upon the foundational synthesis of $CuPbSbS_3$ via the BDCA solution process and unique features of natural piezoelectric and pyroelectric of $BaTiO_3$, Chen et al. further realized the strategic integration of ferroelectric material of $BaTiO_3$ through hydrothermal processing [228]. This methodology enabled the construction of hierarchically structured $BaTiO_3/CuPbSbS_3$ heterostructure, wherein the synergistic interplay between $BaTiO_3$'s piezoelectric polarization and $CuPbSbS_3$'s exceptional optoelectronic properties facilitates efficient piezo-PD of Rhodamine B (RhB). In detail, the $BaTiO_3/CuPbSbS_3$ heterostructures were fabricated via a hydrothermal method using pre-synthesized $CuPbSbS_3$ nanoflakes (Fig. 11a). The resulting composite exhibited well-defined interfaces and preserved crystallinity, as confirmed by X-ray diffraction (XRD), scanning electron microscope (SEM), and TEM.

Piezoelectric response force microscopy (PFM) revealed the pronounced ferroelectric behavior in the $BaTiO_3/CuPbSbS_3$ heterostructure, with 180° phase contrast and butterfly-shaped amplitude loops under bias (Fig. 11b-g). The

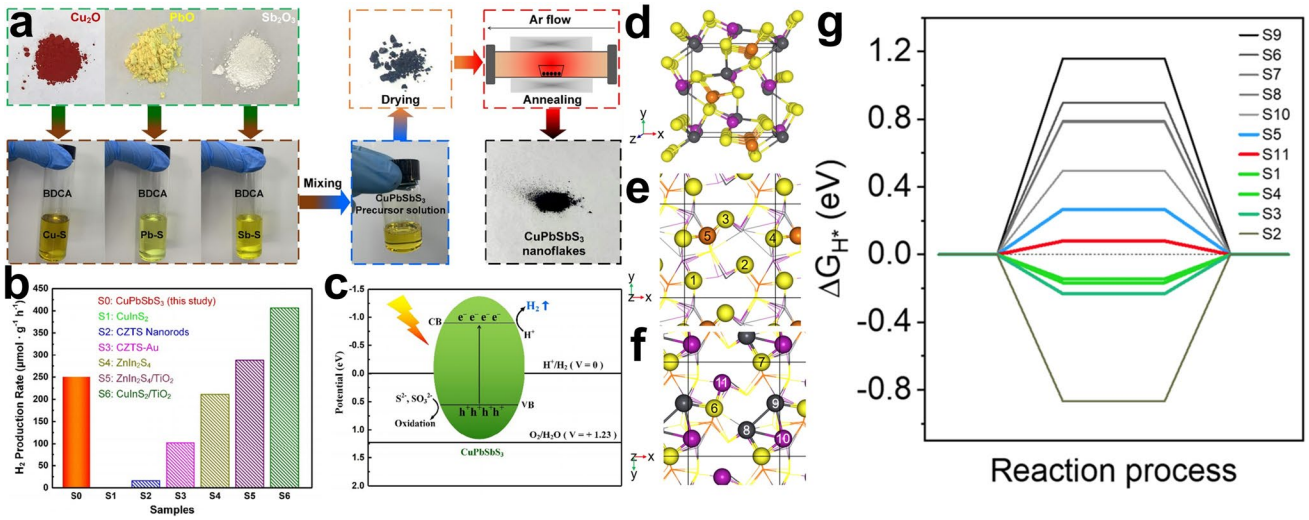

Fig. 10 **a** Schematic of the BDCA solution-processing route for bournonite $CuPbSbS_3$ nanoflake synthesis. Electron microscopy characterization of BDCA-synthesized $CuPbSbS_3$ nanoflakes: **b** Comparative PHE rates under standardized conditions, demonstrating superiority over benchmark sulfides. **c** Proposed mechanistic framework for charge transfer and redox processes. The sequential PHE process involves the steps of (i) electrons' transfer under light irradiation from the VB (+0.54 eV vs. NHE) to the CB (−0.84 eV vs. NHE), resulting in the formation of photogenerated electron−hole pairs; (ii) efficient separation and migration of photogenerated electrons and holes, facilitated by the 3D electronic dimensionality of $CuPbSbS_3$, minimizes the bulk recombination; (iii) photogenerated holes are scavenged by the sacrificial reagents of Na_2S/Na_2SO_3, which concurrently mitigates photocorrosion; (iv) photogenerated electrons in the CB of $CuPbSbS_3$, possessing sufficient thermodynamic overpotential, drive the HER via proton reduction. DFT-derived adsorption energetics: **d** crystal structure highlighting corner-sharing octahedra. **e, f** Atomic configuration of (002) facet adsorption sites (1–11); **g** computed hydrogen adsorption ΔG_{H^*} relative to the thermodynamic optimum (dashed line). Atom color scheme: Cu = orange, S = yellow, Sb = purple, Pb = teal, and H = white. Reproduced with the permission of Ref. [210] Copyright 2022, Elsevier

effective piezoelectric coefficient (d_{33}) of the composite reached 12.1 pm V^{-1}, a 135% enhancement over pristine $BaTiO_3$, indicating strong polarization coupling at the interface. Under the concurrent ultrasonic and visible-light irradiation, the $BaTiO_3$/$CuPbSbS_3$ heterostructure achieved a 90.56% degradation of RhB within 30 min, significantly outperforming individual components (Fig. 11h). The optimal loading of 300 mg $CuPbSbS_3$ (B300) yielded a first-order rate constant of 9.33×10^{-2} min^{-1}, underscoring the synergistic piezo-photocatalytic effect. Time-resolved PL (TRPL) spectroscopy corroborated progressive RhB degradation, with near-complete signal quenching after 60 min (Fig. 11i). Meanwhile, the $BaTiO_3$/$CuPbSbS_3$ heterostructure also demonstrated excellent recyclability, retaining over 80% of its initial activity after multiple cycles. A proposed mechanism (Fig. 11j, k) attributes the enhanced performance to the synergistic interplay between $BaTiO_3$'s piezoelectric polarization and $CuPbSbS_3$'s semiconductor optoelectronic properties: Visible-light excites electron−hole pairs in $CuPbSbS_3$; ultrasonic-induced polarization in $BaTiO_3$ creates an internal electric field, facilitating the charge separation; suitable band alignment promotes electron transfer to $BaTiO_3$ and hole retention in $CuPbSbS_3$; the separated carriers drive radical generation of •OH and $\bullet O_2^-$ and direct oxidation, enabling efficient degradation of RhB.

Building upon the pioneering demonstration of 3D electronically dimensional $CuPbSbS_3$ for PHE, this work innovatively integrates $CuPbSbS_3$ with ferroelectric material of $BaTiO_3$ to construct the $BaTiO_3$/$CuPbSbS_3$ heterostructure. This synergy achieves exceptional visible-light piezo-PD via enhanced charge separation driven by $BaTiO_3$'s polarization field. Therefore, it pioneers $CuPbSbS_3$ application in mechano-opto-catalysis and provides a crucial scientific roadmap for designing advanced $CuPbSbS_3$-based systems toward more efficient PHE.

5.2 Effective Inhibition of Photocorrosion Issue

As established in Sects. 2.3 and 4.3, the photostability of MS photocatalysts is critically compromised by the

 https://doi.org/10.1007/s40820-026-02111-0

photocorrosion issue, a phenomenon driven by surface accumulation of photogenerated holes and extensively documented in prior reviews. Throughout the evolution of MS-based PHE systems, significant research efforts have focused on stabilizing vulnerable lattice S^{2-} ions. Key mitigation strategies encompass defect engineering [229], elemental doping [230], cocatalyst deposition [57, 231], and heterostructure engineering [65, 232], which are also the approaches concurrently employed to enhance overall PHE efficiency of MS photocatalysts (Figs. 12 and 13). Within this context, we first consolidate established methodologies for suppressing photocorrosion in MS photocatalysts and then highlight the emerging paradigm of "controllable-photocorrosion" paradigm for designing ultra-stable MS photocatalysts with precision-engineered degradation pathways.

5.2.1 Conventional Routes for the Solution of Photocorrosion

Defect engineering constitutes a strategic modification approach for extending the optical absorption range of MS and reducing the adsorption and activation energies of reactive intermediates [240–247]. Typically, due to their lower formation energy compared to cation vacancies, surface sulfur vacancies are preferentially employed to modulate the local coordination environment, thereby enhancing PHE activity. However, such vacancies are often insufficient for stabilizing lattice S^{2-} ions, primarily attributed to inefficient photogenerated hole extraction dynamics. Conversely, the introduction of cation vacancies can elevate the VB position through the formation of defect levels above the VBM. This elevation effectively diminishes the oxidizing power of photogenerated holes, offering a pathway toward enhanced the stability of MS photocatalyst. This principle has been

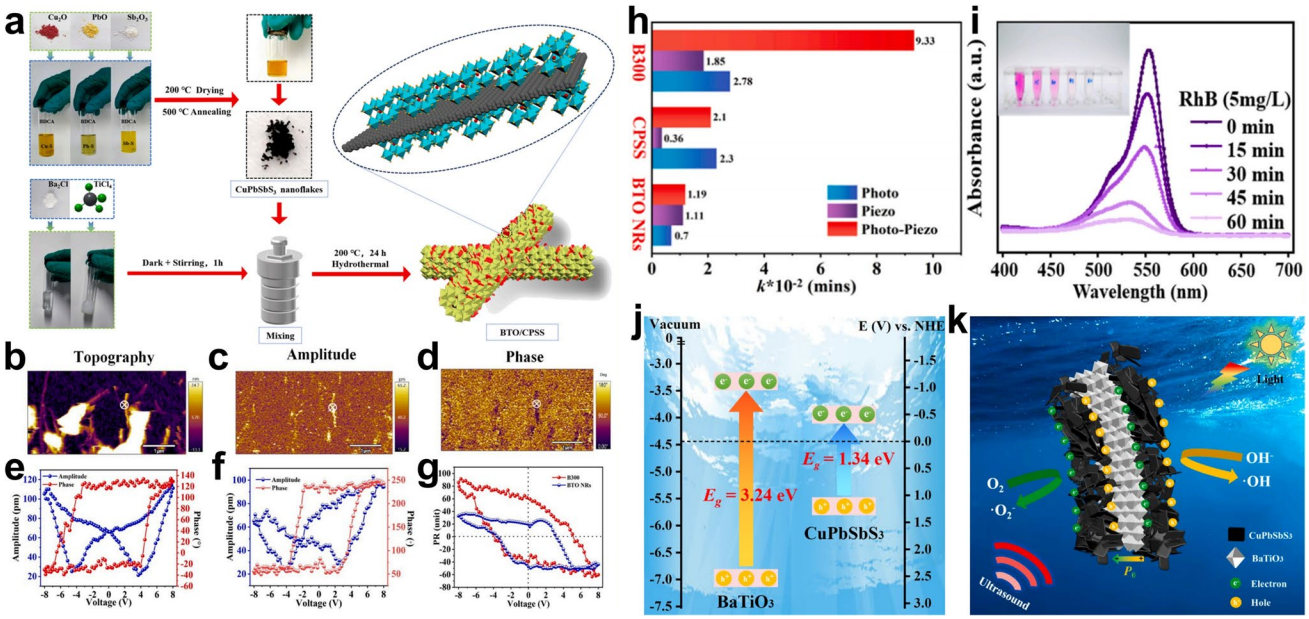

Fig. 11 Synthesis, characterization, and enhanced piezo-PD performance of the $BaTiO_3$/$CuPbSbS_3$ heterostructure. **a** Schematic illustrating the synthesis procedure for the $BaTiO_3$/$CuPbSbS_3$ heterostructure photocatalyst. Ferroelectric properties were characterized via PFM, presenting: **b** topography, **c** phase, and **d** amplitude images. Corresponding **e** phase hysteresis loops, **f** amplitude loops ("butterfly-shaped"), and **g** calculated piezo-response hysteresis loops are shown for both $BaTiO_3$/$CuPbSbS_3$ and pristine $BaTiO_3$. **h** Comparative analysis of *k* value for RhB degradation across the piezo-PD. **i** Temporal evolution of RhB under piezo-PD conditions, monitored via PL spectra for $BaTiO_3$/$CuPbSbS_3$. **j** Calculated water redox potentials (E vs. NHE) for the $BaTiO_3$/$CuPbSbS_3$ heterostructure. **k** Proposed mechanism depicting the enhanced piezo-PD activity within the $BaTiO_3$/$CuPbSbS_3$ heterostructure. The whole process can be summarized as five steps: (i) Generation of electron−hole pairs in $CuPbSbS_3$ by visible-light excitation. (ii) Ultrasonic stress induces piezoelectric polarization in $BaTiO_3$ and creates a built-in electric field. (iii) The built-in electric field drives photogenerated electrons to $BaTiO_3$ and holes to $CuPbSbS_3$ via type-II heterojunction alignment. (iv) Photogenerated holes oxidize adsorbed H_2O/OH^- to •OH, while photogenerated electrons reduce O_2 to $\bullet O_2^-$. (v) Radicals (h^+, •OH, $\bullet O_2^-$) collectively mineralize RhB. The synergy effects of $BaTiO_3$/$CuPbSbS_3$ heterostructure enhances charge separation and suppresses recombination. Reproduced with the permission of Ref. [228] Copyright 2024, Elsevier

exemplified in zinc-deficient ZnS systems, where deliberate fabrication via sulfur source control generates Zn vacancies [233]. These vacancies demonstrably attenuate hole oxidation capacity, significantly mitigating the inherent photocorrosion tendency of ZnS. To synergistically harness the benefits of defect engineering for concurrent activity and stability enhancement, the strategic integration of both cation and anion vacancies within MS photocatalysts has emerged as a promising direction. Supporting this concept, contemporary research has successfully engineered surfaces rich in both zinc and sulfur vacancies on ZnS [234]. Within this dual-vacancy configuration, sulfur vacancies primarily facilitate the tailoring of surface electronic properties to activate adsorbed water molecules, whereas zinc vacancies contribute critically to stability by modulating the VB position upward.

Elemental doping, encompassing both cationic and anionic substitutions, represents a pivotal strategy for modulating the energy band structure of MS photocatalyst [248–254]. Specifically, the introduction of foreign atoms can effectively regulate the oxidation potential of photogenerated holes by establishing impurity energy levels within the bandgap or by forming solid solutions, thereby constituting a highly promising approach for enhancing the PHE stability of MS photocatalysts. Illustrative of this principle, gradient phosphorus doping within CdS nanostructures has been demonstrated to induce an oriented built-in electric field [235]. This internal field facilitates the efficient extraction of photogenerated holes from the bulk to the surface. Consequently, a significant suppression of photocorrosion is realized, as sulfur sites located in the interior are effectively shielded, while photogenerated holes are proficiently extracted and consumed. Such architectural design provides a valuable paradigm for engineering stable and high-performance MS photocatalysts to meet scale-up application requirements. As anticipated, the P-doped CdS exhibited substantially enhanced PHE activity, maintaining robust performance over multiple reaction cycles without significant decreasing. Similarly, the incorporation of transition metal cations (like Zn, Co, Mn, Fe etc.) has also proven effective in mitigating the inherent photocorrosion susceptibility of CdS to varying extents [255].

Cocatalyst deposition has been extensively explored as a strategic approach to divert photogenerated holes away from MS, thereby mitigating oxidative degradation of these semiconductor materials [256–266]. Specifically, oxidative cocatalysts fulfill the fundamental role of photogenerated hole extraction. For instance, Lei et al. demonstrated that the photodeposited cobalt-modified amorphous molybdenum sulfide (Co-MoS_x) acts as an effective cocatalyst on ZnCdS, significantly enhancing visible-light PHE (551.48 μmol h^{-1}, AQE = 21.7%) [236]. Crucially, the Co-MoS_x layer synergistically suppresses ZnCdS photocorrosion by facilitating charge separation and forming a stabilized heterointerface, thus addressing a major stability limitation while boosting activity. At the same time, Liu et al. presented a robust strategy to concurrently enhance the PHE activity and photostability of CdS by constructing a stacked nanostructure with reduced graphene oxide (rGO) supporters and metallic MoS_2 overlayers [237]. Critically, this design effectively mitigates the inherent photocorrosion of CdS, through a dual protective mechanism: the MoS_2 cocatalyst extracts photogenerated holes, preventing oxidative consumption of S^{2-}, while the rGO rapidly shuttles excess electrons to MoS_2 for efficient proton reduction. This synergistic cocatalyst integration yields exceptional PHE rates (14.4 mmol g^{-1} h^{-1}) and remarkable cyclic stability due to the effective inhibition of photocorrosion, underscoring the pivotal role of tailored cocatalyst deposition in overcoming stability challenges in MS-based photocatalysis.

Beyond the aforementioned-approaches, heterojunction engineering represents a well-established and critical methodology meriting particular emphasis [267–273]. To date, primary heterojunction configurations encompass type-I, type-II, $p-n$, Z-scheme, and S-scheme architectures [274–280]. Illustratively, the intrinsic photocorrosion susceptibility of $ZnIn_2S_4$ has been successfully addressed through constructing a ternary Z-scheme system comprising TiO_2, Au, and $ZnIn_2S_4$ [238]. This configuration facilitates interfacial recombination of holes from $ZnIn_2S_4$ with electrons from TiO_2 via the Au electron mediator. Liu et al. demonstrated that constructing S-scheme heterojunctions by integrating WO_3 with MS (typical maple leaf-shaped CdS) significantly enhances PHE activity [239]. The optimized 0D WO_3/CdS S-scheme heterojunction achieves an exceptional PHE rate of 34.12 mmol g^{-1} h^{-1}, attributed to synergistic morphology effects and interfacial charge dynamics. Critically, the S-scheme mechanism effectively mitigates photocorrosion in sulfides by directing photogenerated holes from sulfides to WO_3, thereby preserving structural

 https://doi.org/10.1007/s40820-026-02111-0

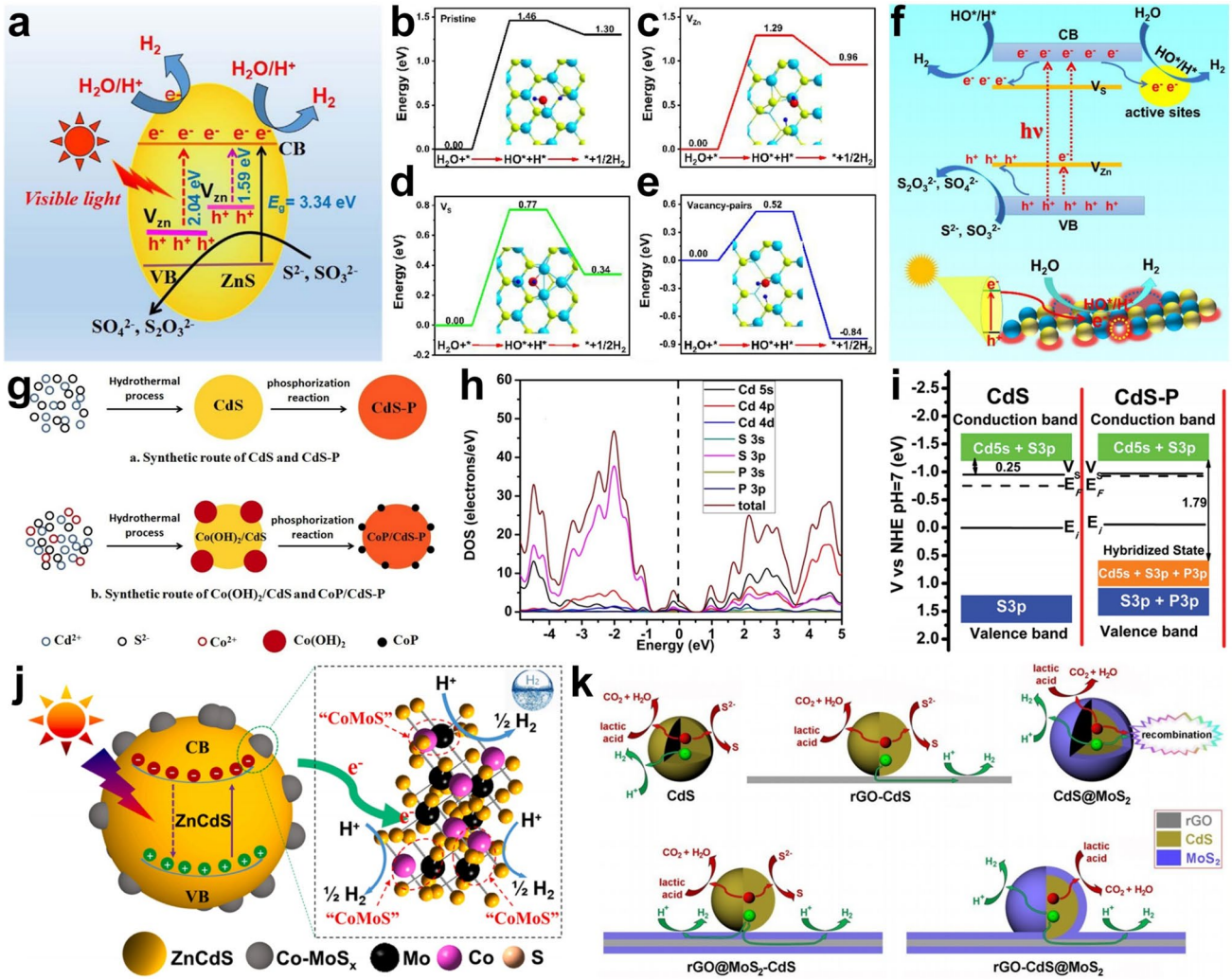

Fig. 12 Conventional routes for the solution of MS's photocorrosion: **a-f** defect engineering; **g-i** elemental doping; **j, k** cocatalyst deposition. **a** Synergistic PHE mechanism of defect-engineered ZnS under visible-light irradiation, illustrating Zn vacancies as multifunctional centers that extend visible-light harvesting, facilitate charge separation, and critically attenuate oxidative photocorrosion through VB modulation. Reproduced with the permission of Ref. [233] Copyright 2018, Elsevier. **b–e** Schematic depiction of the potential energy profile governing PHE, highlighting distinct transition-state geometries on pristine versus vacancy-defective ZnS surfaces. Atomic species are color-coded (Zn: light blue; S: green). **f** Proposed mechanisms for solar-driven photocatalytic hydrogen generation and charge migration over ZnS featuring abundant surface vacancies. Reproduced with the permission of Ref. [234] Copyright 2021, American Chemical Society. **g** Synthesis procedure for $Co(OH)_2$/CdS composites (composition tuned via cobalt precursor) and derived CoP/CdS-P, modified from CdS preparation. **h** Room-temperature TRPL decay dynamics of acetone-dispersed nanostructures. **i** Schematic band alignment and E_f shifts in CdS and CdS-P. Reproduced with the permission of Ref. [235] Copyright 2018, Wiley. **j** Schematic PHE over ZnCdS/$CoMoS_x$ heterostructures under visible-light illumination. Reproduced with the permission of Ref. [236] Copyright 2021, Elsevier. **k** Schematic PHE over CdS-derived nanostructures with cocatalysts under visible-light. Reproduced with the permission of Ref. [237] Copyright 2021, Royal Society of Chemistry

integrity. Concurrently, efficient electron−hole separation via the S-scheme pathway and exposure of high-activity (100) crystal facets collectively boost hydrogen generation.

Conventional MS photocatalysts modifications partially suppress photocorrosion but still face two major challenges: (i) synthesis complexity involving demanding operational protocols hinders industrial scalability; (ii) predominant reliance on hole extraction mechanisms fails to prevent lattice S^{2-} oxidation by electron/oxygen-derived superoxide radicals, necessitating co-extraction of both charge carriers. Consequently, the exploration of advanced processes to

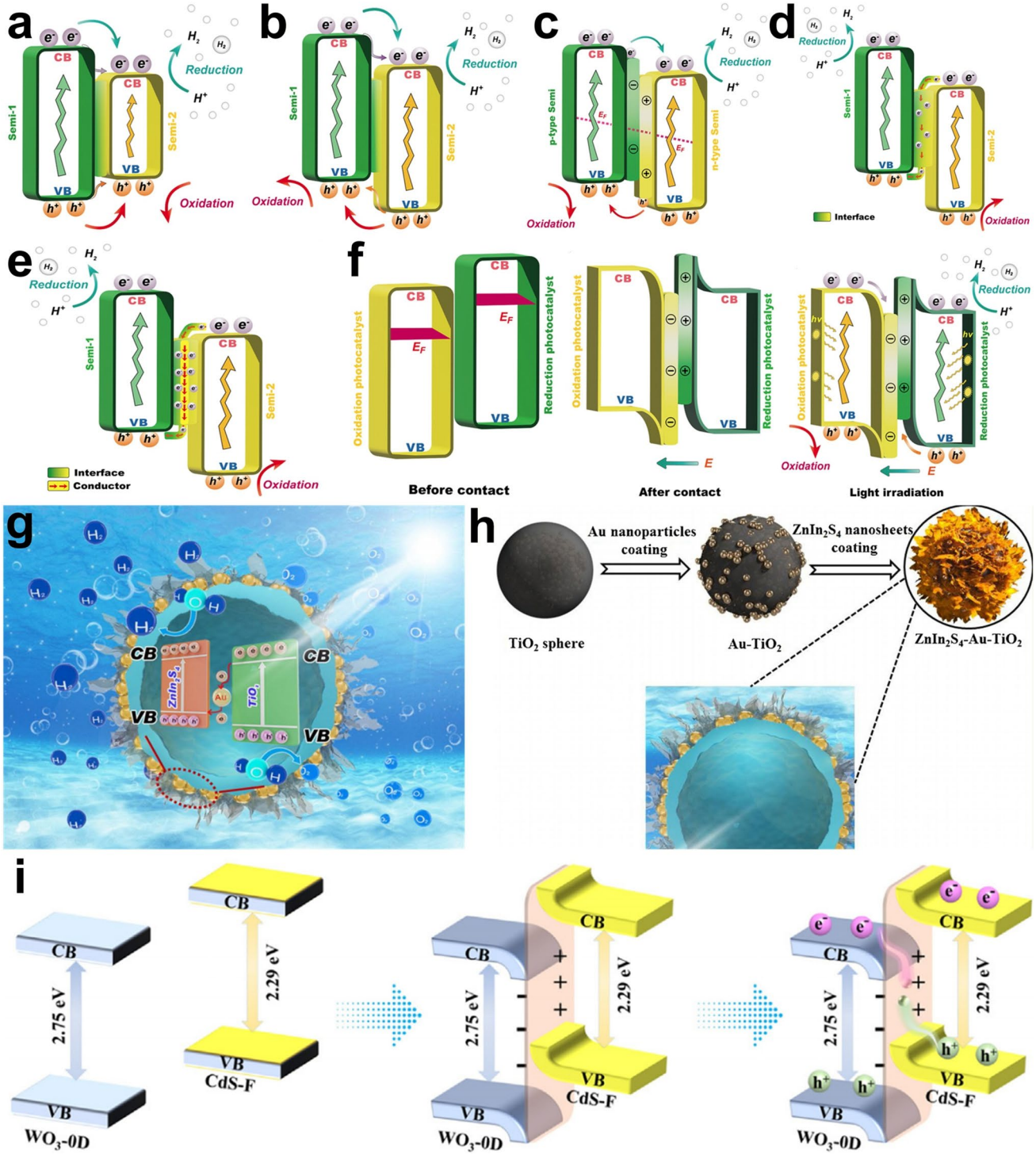

Fig. 13 Conventional routes for the solution of MS's photocorrosion: heterostructure engineering. Charge transfer schematics in heterojunction photocatalysts: **a** type-I, **b** type-II, **c** *p*−*n*, **d** mediator-free Z-scheme, and **e** mediator-assisted Z-scheme. **f** S-scheme interfacial dynamics (pre-contact, post-contact, illuminated states). Reproduced with the permission of Ref. [63] Copyright 2025, Elsevier. **g** Proposed Z-scheme heterojunction in the $ZnIn_2S_4/Au/TiO_2$ heterostructure for PHE. **h** Two-step fabrication of the photocatalyst: chemical deposition of Au/TiO_2 followed by solvothermal growth of $ZnIn_2S_4$. Reproduced with the permission of Ref. [238]. Copyright 2018, Elsevier. **i** S-scheme heterojunction mechanism in CdS/WO_3, showing band alignment and charge separation under illumination. Reproduced with the permission of Ref. [239]. Copyright 2024, Elsevier

 https://doi.org/10.1007/s40820-026-02111-0

overcome the photocorrosion issue is of great importance for the design concept of advanced MS photocatalysts.

5.2.2 *Advanced Design Concept of Photocorrosion Inhibition*

Existing photocorrosion mitigation strategies for MS photocatalysts (Sect. 5.2.1), are largely post-synthesis modifications that do not tackle the root causes of photocorrosion. Furthermore, conventional synthetic routes overwhelmingly rely on the introduction of extraneous sulfur sources, such as thioacetamide, sodium sulfide, and thiourea, which both hinder corrosion suppression and generate high-density sulfur vacancies. These high-density vacancies significantly diminish the concentration of photogenerated electrons available for the HER, thereby substantially compromising hydrogen production efficiency. Consequently, the development of advanced synthetic methods capable of fundamentally suppressing MS photocorrosion issue while maintaining rigorous phase purity represents a sophisticated and promising design concept.

As detailed in Sect. 5.1.1, $CuPbSbS_3$ photocatalysts have been successfully synthesized by the BDCA solution method and applied to PHE. Originally developed depositing absorber layers in thin-film solar cells, typically Sb_2S_3, $Sb_2(S, Se)_3$, $Cu(In,Ga)(S,Se)_2$, and CZTS thin films' deposition [281–287], the BDCA solution process lacks targeted mechanistic analysis in the MS context. To address this gap, our group has conducted a focused investigation into the microscopic evolution of the BDCA solution process formation and its corresponding synthesis pathway for MS semiconductor materials (especially the MS photocatalyst) (Fig. 14) [288], revealing its intrinsic "sulfur-coordination-directed" mechanism. This fundamental understanding thereby provides a rigorous scientific foundation for developing advanced synthesis process underpinned by intrinsic sulfur-coordination directionality, offering a promising route toward substantially suppressing MS photocorrosion issue [84]. Specifically, BDCA synthesis proceeds via the reaction of carbon disulfide (CS_2) with *n*-butylamine ($CH_3(CH_2)_3NH_2$) [281]. During this chemical transformation, homolytic cleavage of one C = S bond in CS_2 generates a reactive S = C–S• radical intermediate. Subsequently, the unsaturated carbon and sulfur atoms within this intermediate undergo concerted reactions with the nitrogen and hydrogen atoms of *n*-butylamine, respectively, culminating in the formation of BDCA ($C_5H_{11}NS_2$). Within the $C_5H_{11}NS_2$ structure, the dithiocarbamate moiety (−NH−CSS−) exhibits dual functionality, serving concurrently as a sulfur donor and a metal-chelating ligand. This bifunctional nature fosters a dynamic coordination equilibrium involving metal–sulfur interactions at the molecular level, endowing the system with its distinctive intrinsic sulfur-coordination directionality property. Furthermore, the thionothiolic acid group (−CSSH) in BDCA undergoes facile deprotonation in ethanolic solution, yielding H^+ and $S_2CNHC_4H_9^-$ ions. The liberated protons promote the dissolution of MO (or metal hydroxide) precursors, forming an organometallic complex, $M(S_2CNHC_4H_9)_x$, with water (xH_2O) as a byproduct. Following drying and pyrolysis, the MS photocatalyst is ultimately formed via the thermal decomposition pathway: $M(S_2CNHC_4H_9)_x \rightarrow M_yS_x + x(S_2CNHC_4H_9)$. Therefore, based on the deep analysis of the BDCA solution formation mechanism and the microscopic evolution of MS synthesis via the BDCA method, it can be revealed that the −NH−CSS− organic group within BDCA molecular exhibits dual functionality, concurrently serving as both the sulfur source and a metal-chelating ligand. This inherent bifunctionality enables the direct synthesis of MS semiconductor materials (especially MS photocatalysts) without requiring extraneous sulfur sources, thereby significantly streamlining the synthetic protocol while concurrently enhancing phase purity. More significantly, the intrinsic sulfur-coordination directionality property of the BDCA solution facilitates the construction of a molecular-scale metal–sulfur dynamic equilibrium system. This system effectively enhances the M-S bond stability within MS photocatalysts, leading to a substantial suppression of the oxidation reaction between S^{2-} anions and photogenerated holes under light illumination. Consequently, this mechanism provides an effective pathway for mitigating the inherent photocorrosion issue intrinsic to MS photocatalyst. To date, the intrinsic sulfur-coordination directionality property of the BDCA solution method has been effectively validated in the MS photocatalysts of CdS and ZnCdS, demonstrating its substantial efficacy in suppressing the photocorrosion issue. Notably, the deep research on ZnCdS photocatalysts synthesized via this approach has further enabled the proposal of an advanced "controllable-photocorrosion" concept. This paradigm shift strategically transforms the inherent

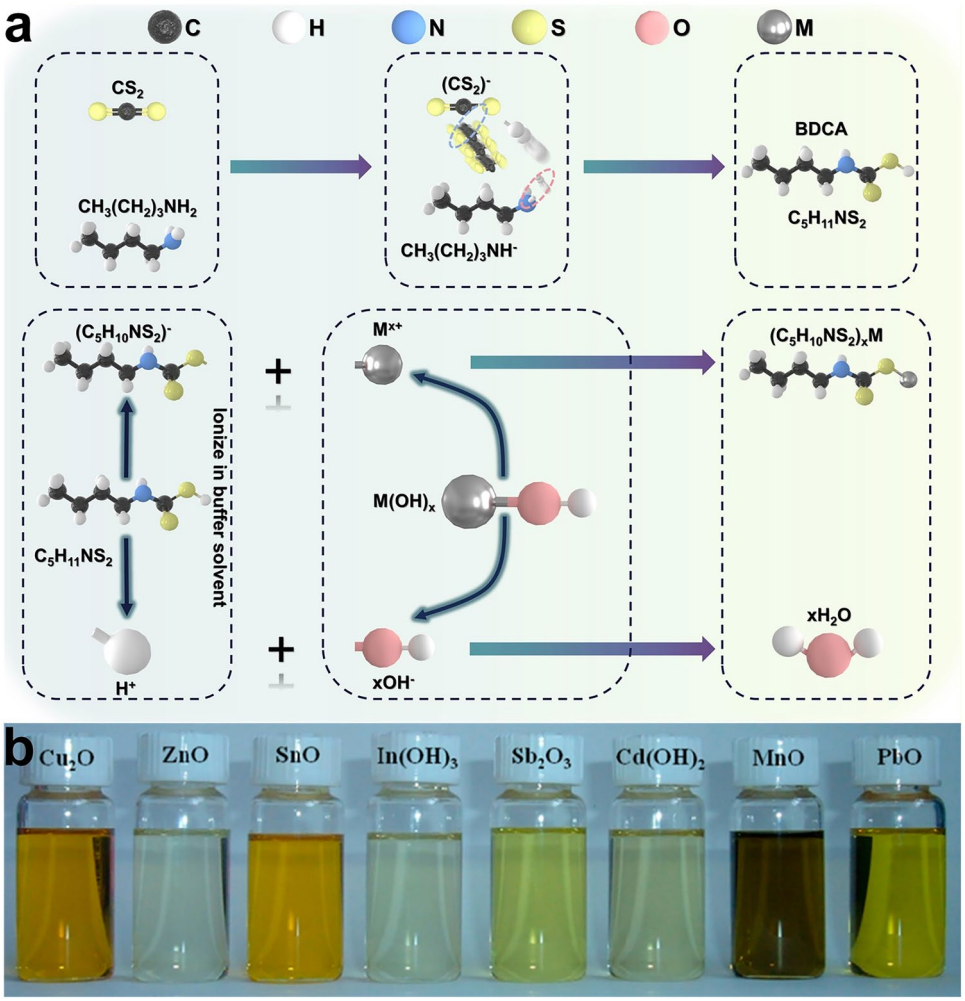

Fig. 14 **a** Reaction mechanism for intrinsic sulfur-coordination directionality BDCA solution generation (top) and ambient-temperature dissolution dynamics of MOs/hydroxides in BDCA (bottom). **b** Optical images of BDCA solution after dissolving several representative MOs or metal hydroxides. Reproduced with the permission of Ref. [287] Copyright 2012, American Chemical Society

detrimental effects of photocorrosion into a functionally advantageous process [84].

CdS, an archetypal BMS photocatalyst, possesses an optimal bandgap (~2.4 eV) and sufficiently negative CB potential, rendering it highly effective for visible-light-driven PHE [289]. To date, CdS-based photocatalytic systems have achieved significant and noteworthy progress in this domain [289–294], and several comprehensive reviews have extensively documented the research trajectory and future prospects for CdS photocatalysts [295–298]. Notably, the vast majority of both primary research and review articles concerning CdS explicitly acknowledge its severe susceptibility to photocorrosion issue. Consequently, the proposed mitigation strategies predominantly align with the conventional approaches to suppressing photocorrosion, as detailed in Sect. 5.2.1. In light of this persistent challenge, our group pioneered the application of the BDCA solution method to CdS photocatalyst synthesis in 2023, concurrently initiating a preliminary investigation into its underlying mechanism for photocorrosion suppression [299]. Specifically, CdS synthesis initiates with the dissolution of $Cd(OH)_2$ in BDCA solution (also shown in Fig. 14b), forming the Cd–S precursor complex. The subsequent thermal treatment involves precise drying at low temperature to remove volatile solvents and annealing at high temperature to crystallize CdS. Crucially, the BDCA serves a dual function: the sole sulfur

 https://doi.org/10.1007/s40820-026-02111-0

source, eliminating the need for toxic external sulfur precursors; the metal-chelating ligand, facilitating molecular-scale control over Cd–S bond formation. This inherent intrinsic sulfur-coordination directionality property is central to suppressing high-density sulfur vacancy formation, also the key initiator of photocorrosion issue. XRD analysis (Fig. 15a) confirmed the formation of crystalline CdS across annealing temperatures from 300 to 600 °C. While a mixture of cubic (c-CdS) and hexagonal (h-CdS) phases spontaneously formed, the ratio evolved with temperature: Higher annealing temperatures favored the hexagonal phase. At the same time, the absence of impurity peaks underscores the high phase-purity achievable with BDCA, a direct consequence of its integrated sulfur supply, and chelation capability, mitigating defect-induced instability. The HRTEM provided direct evidence of interfacial regions between c-CdS and h-CdS domains within individual nanoparticles (Fig. 15b). While this phase junction (incidentally formed during synthesis) contributes to charge separation, the primary focus here is the structural integrity. The clean interface and well-defined lattices observed suggest minimal crystallographic defects, attributable to the controlled precursor decomposition of BDCA solution method. This defect suppression is intrinsically linked to enhanced photocorrosion resistance.

Photocatalytic evaluation revealed a strong dependence of PHE rate on annealing temperature. The CdS-500 sample (annealed at 500 °C) achieved a remarkable PHE rate of 7.294 mmol g^{-1} h^{-1} under visible-light without loading of any cocatalysts, surpassing many reported CdS-based systems [296]. Significantly, over four consecutive 4-h cycles (960 min total irradiation), the CdS photocatalyst maintained robust activity with negligible decay and even exhibited a rate increase in the third cycle, indicative of surface activation rather than degradation. This sustained performance starkly contrasts the rapid deactivation typical of bare CdS and directly validates the efficacy of BDCA solution method in mitigating photocorrosion issue of MS, along with other kinds of MS photocatalysts. The inherent sulfur richness and optimized Cd–S bonding environment provided by the BDCA-derived precursor minimize the oxidation of lattice S^{2-} by photogenerated holes, the core mechanism of photocorrosion issue mentioned in Sect. 4.3. DFT models of c-CdS, h-CdS, and their phase junction (Fig. 15c) were analyzed for ΔG_{H^*} on sulfur sites (Fig. 15d), revealing that the sulfur sites in pure c-CdS ($\Delta G_{H^*} = +1.22$ to 2.30 eV) and h-CdS ($\Delta G_{H^*} = -1.35$ to -2.44 eV) exhibited overly weak or strong hydrogen binding, respectively, hindering efficient HER. Obviously, specific sulfur sites near the c-CdS/h-CdS interface achieved near-optimal ΔG_{H^*} (nearly 0 eV). The charge density redistribution at the junction modulates the reactivity of these interfacial sulfur atoms. Crucially, beyond promoting HER kinetics, the BDCA-derived synthesis likely stabilizes these interfacial sulfur sites. The precise sulfur-coordination during precursor formation and decomposition minimizes undercoordinated or vacancy-associated sulfur sites, which are particularly vulnerable to oxidative attack by photogenerated holes. This inherent stabilization, coupled with thermoneutral ΔG_{H^*}, underpins both high activity and suppressed photocorrosion issue. Under illumination, photogenerated electrons in the higher-lying c-CdS CB migrate to h-CdS, while holes move in the opposite direction across the VB. This spatial separation reduces charge recombination. More importantly, the BDCA-synthesized structure promotes efficient hole consumption at the interface or within the h-CdS domain, likely facilitating their reaction with sacrificial agents (S^{2-}/SO_3^{2-}) before they can oxidize the vulnerable lattice S^{2-}. Furthermore, the robust Cd–S bonding environment, inherent to the BDCA-derived lattice, intrinsically raises the activation barrier for the photocorrosion reaction ($2\,h^+ + CdS \rightarrow Cd^{2+} + S^0$).

Based on the above-mentioned analyses, this research pioneers the intrinsic sulfur-coordination directionality BDCA solution method as a transformative strategy for synthesizing the traditional MS photocatalysts of CdS with intrinsically suppressed the general photocorrosion issue. By utilizing BDCA's dual role as a sulfur source and chelating ligand, this method ensures the solution of the following four aspects: (i) High phase-purity and reduced defects: Eliminating extrinsic sulfur sources minimizes sulfur vacancies, a primary photocorrosion initiation site. (ii) Optimized Cd–S bonding: The intrinsic sulfur-coordination directionality feature fosters a stable sulfide lattice less susceptible to oxidative hole attack. (iii) Inherent interfacial stability: The naturally formed phase junction, while aiding charge separation, also hosts sulfur sites stabilized by charge redistribution, exhibiting both high HER activity and resistance to oxidation. (iv) Simplified synthesis complexity: The method avoids complex heterostructuring or capping agents. Therefore, it is foreseeable that the BDCA solution method may hold promise in addressing the photocorrosion issue of other types of MS photocatalysts. Building upon the established success of the BDCA solution method in

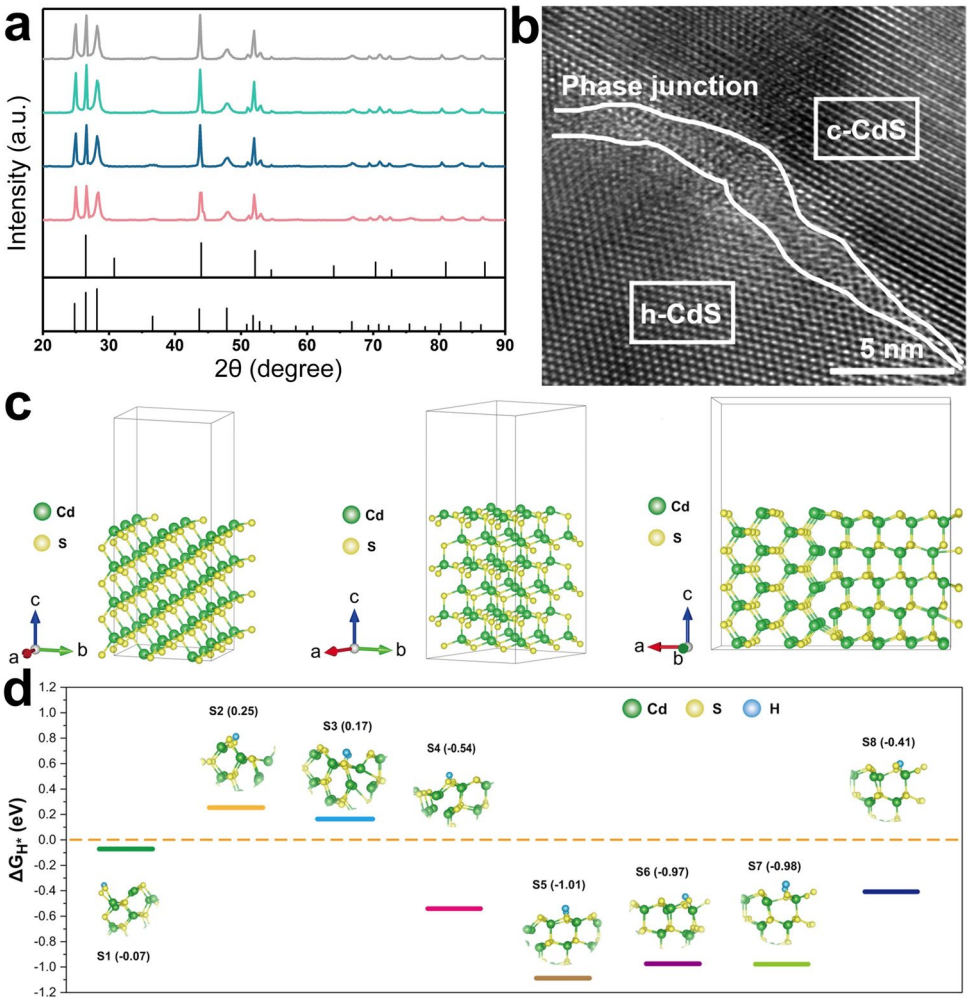

Fig. 15 Characterization, and DFT-calculated theoretical insights of BDCA-synthesized CdS photocatalysts: **a** XRD patterns confirming the crystalline phases of CdS samples synthesized following thermal treatment at various temperatures. **b** HRTEM image providing direct evidence of the h-CdS/c-CdS phase junction microstructure. **c** Computational models depicting the atomic configurations of cubic CdS (left), hexagonal CdS (middle), and the constructed phase junction interface (right). **d** Comprehensive mapping of the calculated ΔG_{H^*} across all sulfur sites identified at the CdS phase junction interface. Reproduced with the permission of Ref. [299] Copyright 2023, Wiley

effectively suppressing the photocorrosion issue of CdS, our group subsequently synthesized ZnCdS solid solution photocatalysts employing this methodology [84]. Significantly, we pioneered the novel concept of "controllable-photocorrosion" in this research. This conceptual breakthrough represents a paradigm shift, effectively transforming photocorrosion from a detrimental phenomenon impeding material stability into a strategically leveraged functional attribute. Compared with CdS, ZnS demonstrates markedly superior photostability, attributable to its stronger Zn–S bonding. Nevertheless, its wide bandgap (about 3.4 eV), exceeding even that of TiO_2, fundamentally constrains visible-light PHE utility [234]. The strategic formation of ZnCdS solid solution effectively addresses this limitation, synergistically combining the visible-light responsiveness of CdS with the durability of ZnS, along with the tunable bandgap (Fig. 16) [300–303]. This alloying approach yields an efficient visible-light photocatalyst for HER, harmonizing tunable bandgap energetics with enhanced photocorrosion resistance [304]. Contemporary reviews have extensively documented these distinctive advantages and the developmental trajectory of ZnCdS in PHE [55, 300]. Notably, such analyses consistently emphasize resolving ZnCdS photocorrosion as a critical research priority. Prevailing mitigation strategies, as cataloged in prior syntheses (Sect. 5.2.1), primarily encompass defensive paradigms: bandgap tuning via Zn/Cd

 https://doi.org/10.1007/s40820-026-02111-0

stoichiometric control, morphological optimization, sulfur vacancy engineering, cocatalyst functionalization, and heterojunction construction.

Building upon the BDCA solution-based methodology for synthesizing CdS (involving the dissolution of $Cd(OH)_2$ in BDCA solution), this research extended this methodology to incorporate ZnO dissolved within the BDCA solution, ultimately resulting in the successful fabrication of ZnCdS photocatalyst, possessing a uniquely engineered structure compared with the ZnCdS fabricated by the conventional extra sulfur source method: a sulfur-rich surface layer and a strategically positioned Zn-subsurface distribution (Fig. 17a). HRTEM confirmed the nanoparticle morphology and crystallinity, while high-angle annular dark-field scanning TEM (HAADF-STEM) elemental mapping and STEM-EDS line scanning (Fig. 17b) provide direct evidence of the critical subsurface Zn enrichment beneath the Cd-rich surface. The initial sulfur-rich surface acted as a sacrificial hole scavenger and provides abundant active sites for the HER, which has also been proved by FT-IR in this work. This specific architecture, subsurface Zn and a sacrificial S-rich surface, forms the foundation for controllable-photocorrosion. In detail, contrary to conventional photocorrosion leading to degradation of MS photocatalysts, the BDCA-ZnCdS exhibited increasing PHE activity during extended illumination. The PHE rate surged 2.5-fold over the first five cycles (reaching 30.12 mmol g^{-1} h^{-1}) and stabilized thereafter. This phenomenon stems from a self-optimizing mechanism: During the initial PHE, photogenerated holes oxidize the sacrificial sulfur-rich surface and the outermost CdS layer. The photocorrosion generates reactive sulfur species that accumulate in situ, forming a new catalytically active sulfur-rich surface. DFT calculations (Fig. 17c) proved these newly formed sulfur sites (S3: $\Delta G_{H^*} = 0.16$ eV; S4: $\Delta G_{H^*} = 0.30$ eV) exhibit near-optimal ΔG_{H^*}, significantly enhancing HER kinetics compared to pristine CdS or ZnCdS surfaces ($\Delta G_{H^*} > 1.0$ eV). Simultaneously, the strong Zn–S bonds reflected by the ICOHP (ICOHP = − 1.27 to − 1.28 vs. Cd–S ICOHP = − 1.15) act as an intrinsic barrier, confining further corrosion to the Cd-rich upper layers once the Zn-subsurface is reached. This confinement prevents bulk degradation, establishing a dynamic equilibrium between sacrificial corrosion (providing new active S-sites) and structural preservation (enabled by subsurface Zn).

Based on the above results, we redefine the photocorrosion of MS photocatalyst (Fig. 17d–f): uncontrolled photocorrosion rapidly oxidizes S^{2-} and dissolves Cd, degrading CdS, whereas the BDCA-ZnCdS deliberately employs a controlled corrosion process. The initial S-rich surface and subsurface Zn distribution transform a typically detrimental phenomenon into a functional strategy: (i) The initial sulfur-rich layer sacrificially scavenges holes, mitigating hole-induced bulk damage; (ii) the controlled corrosion of the cadmium-rich surface generates highly active in situ S-sites and thus boosts HER activity; (iii) the robust Zn–S subsurface layer terminates corrosion progression, ensuring long-term structural integrity. This controllable-photocorrosion mechanism creates a self-sustaining system where corrosion product (sulfur) becomes the functional site, and corrosion depth is physically limited, resulting in both rising and sustained high activity. It represents a fundamental shift that leveraging photocorrosion productively for enhanced functionality and stability, rather than merely seeking its suppression.

5.2.3 Thermodynamic and Kinetic Foundations of Controllable-Photocorrosion

Beyond the above-mentioned phenomena description, the fundamental of controllable-photocorrosion can be also strictly explained through coupled thermodynamic and kinetic analyses. Thermodynamically, the resistance of MS photocatalysts to oxidative destruction is governed by the bond dissociation energy (BDE) of M–S bonds [208]. Representatively, in ZnCdS solid solutions, the Zn–S bond exhibits an obviously higher BDE (2.7 eV) compared to Cd–S (2.3 eV), as also evidenced by ICOHP calculations (− 1.32 of Zn–S and − 1.15 of Cd–S). This obvious energy difference creates a thermodynamic sink that confines the anodic corrosion to the Cd-rich surface layer, while the underlying Zn–S network simultaneously acts as an intrinsic barrier against the bulk destruction of the entire photocatalyst [84]. At the same time, such bond energy gradients can be quantitatively mapped via DFT-based ICOHP analysis, which provides a predictive parameter for designing corrosion-resistant layered architectures. Kinetically, the self-limiting feature of controllable-photocorrosion arises from the dynamic balance between the hole-induced oxidation and in situ passivation. The real-time detecting using in situ Raman spectroscopy and electrochemical impedance spectroscopy reveals that

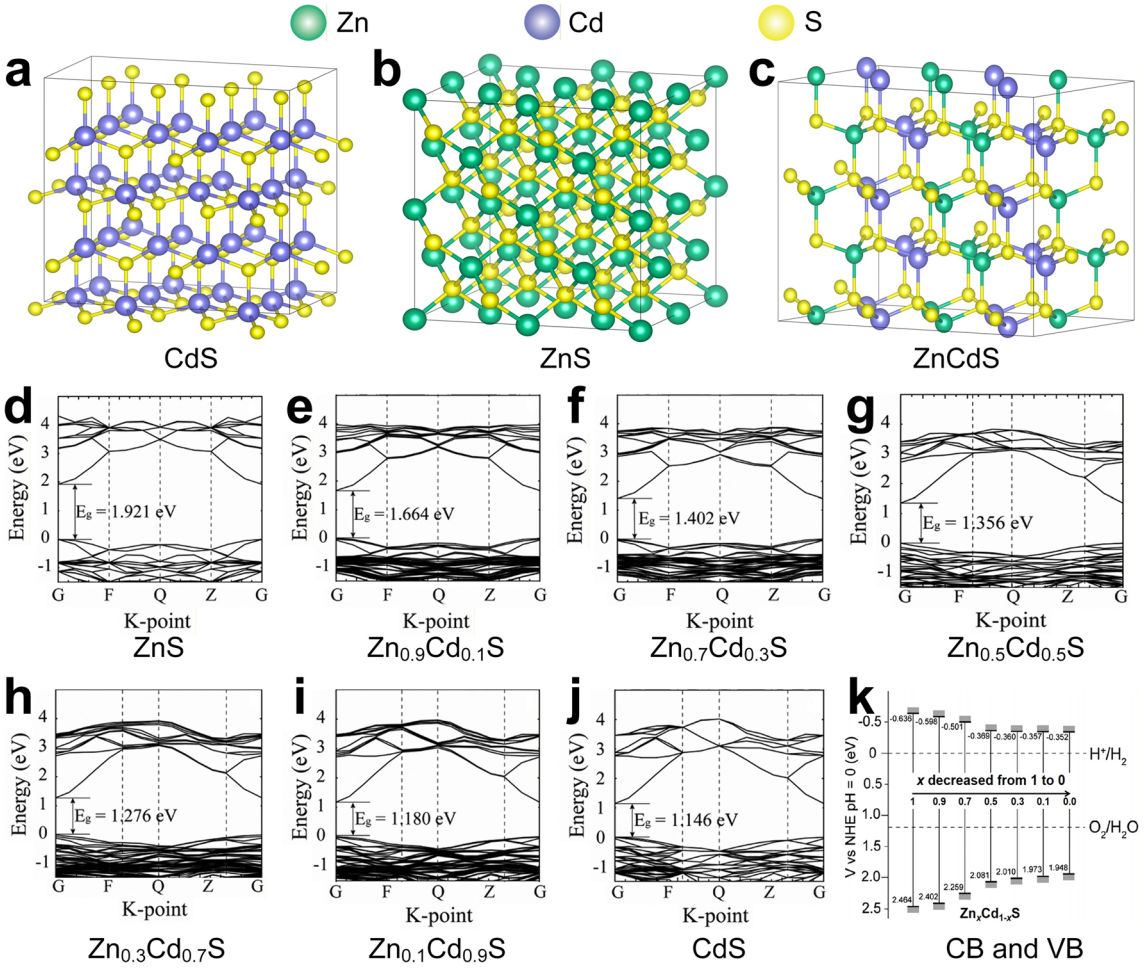

Fig. 16 Properties of ZnCdS solid solution, illustrated by crystal structure, DFT-calculated band structure, and CB/VB positions: Crystal structures of **a** CdS, **b** ZnS, and **c** ZnCdS solid solution with Zn/Cd ration of 1:1. Reproduced with the permission of Ref. [65] Copyright 2024, Wiley. DFT-calculated band structures of ZnCdS photocatalysts with different Zn/Cd ratios: **d** 1:0, **e** 9:1, **f** 7:3, **g** 1:1, **h** 3:7, **i** 1:9, and **j** 0:1. **k** CB and VB positions of ZnCdS with different Zn/Cd ratios. Reproduced with the permission of Ref. [301] Copyright 2013, American Chemical Society

the initial photocorrosion rate of the sulfur-rich surface ($k_{\text{initial-corrosion}} \approx 10^{-3}$ s^{-1}) decelerates by over an order of magnitude after the formation of reactive-sulfur overlayer ($k$steady-corrosion $\approx 10^{-4}$ s^{-1}) [305]. This kinetic transition is accompanied by a progressive anodic shift in the flat-band potential ($\approx +0.15$ V), indicating the increasing of a hole-blocking interfacial dipole [306]. Quantitatively, the photocorrosion inhibition efficiency (η_{PI}) can be expressed as: $\eta_{\text{PI}} = (1 - j_{\text{modified}}/j_{\text{pristine}}) \times 100\%$, where j_{modified} and j_{pristine} are the photocorrosion-current densities of engineered and pristine MS photocatalyst, respectively. Taking the BDCA-ZnCdS as the example, η_{PI} exceeds 80% after five PHE cycles, a metric that relates directly with the preservation of PHE activity. Such quantitative parameters, combining bond-energy mapping, photocorrosion rate spectroscopy, and interfacial kinetic profiling, transform the controllable-photocorrosion from a descriptive concept into an advanced design concept rooted in MS photocatalysts' thermodynamics and reaction dynamics.

5.2.4 *Quantitative Superiority of BDCA in Photocorrosion Suppression*

To quantitatively evaluate the superiority of BDCA solution method in mitigating photocorrosion issue and enhancing

https://doi.org/10.1007/s40820-026-02111-0

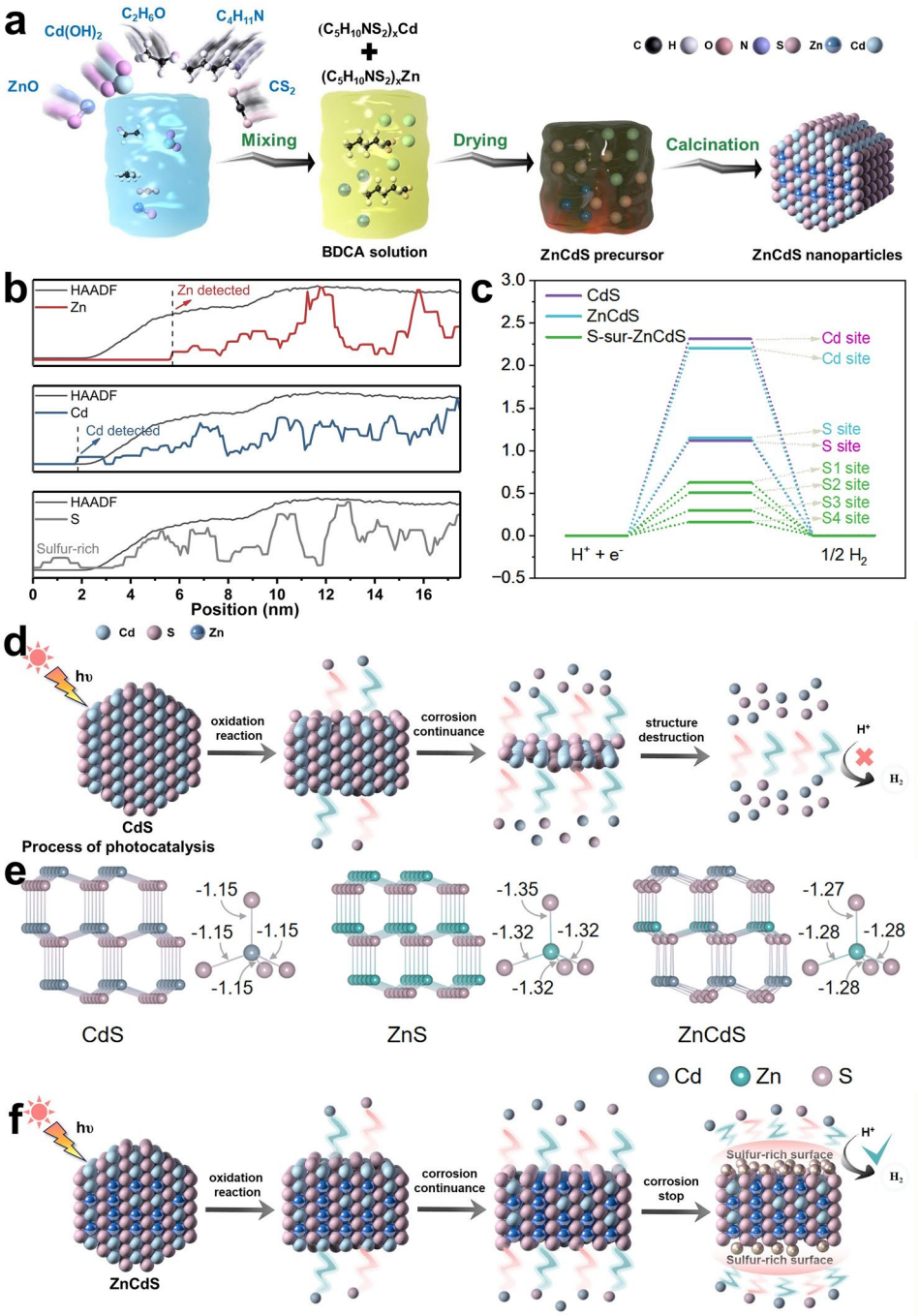

Fig. 17 Synthesis and multiscale characterization of BDCA-synthesized ZnCdS solid solution photocatalyst with unique controllable-photocorrosion feature. **a** Schematic illustration of the ZnCdS solid solution synthesis via the BDCA solution process. **b** Compositional line-scan profile acquired by STEM-EDS. **c** Computational evaluation of ΔG_{H^*} for CdS, ZnCdS, and sulfur-enriched ZnCdS surfaces (S-sur-ZnCdS). **d** Comparative schematic depicting the photocorrosion pathway in pristine CdS. **e** Bulk structural analysis: Atomic configurations and computed crystal orbital ICOHP values for Cd–S and Zn–S bonds in CdS, ZnS, and ZnCdS. **f** Integrated mechanistic model of the photocorrosion process in BDCA-synthesized ZnCdS: (i) Under illumination, photogenerated holes oxidize the sacrificial sulfur-rich surface and the underlying Cd-rich layer, resulting in the generation of reactive sulfur species. (ii) Photocorrosion progresses inward but is confined to the upper Cd-rich region. (iii) Photocorrosion terminates upon reaching the subsurface Zn–S layer, where stronger Zn–S bonds (evidenced by more negative ICOHP values) act as the kinetic barrier. (iv) Establishing of dynamic equilibrium: sacrificial corrosion continuously regenerates catalytically active sulfur sites at the surface, while the robust Zn–S subsurface preserves structural integrity, leading to self-optimized and stable PHE activity. Reproduced with the permission of Ref. [84] Copyright 2025, Wiley

PHE performance of MS photocatalyst, we also systematically compare key metrics of defect density, photocorrosion resistance, and photostability between BDCA-synthesized and conventionally synthesized MS photocatalysts (Table 1). As illustrated in Fig. 15d, e, BDCA-synthesized CdS (CdS-500) exhibits a remarkable PHE rate of 7.294 mmol g^{-1} h^{-1} under visible light, surpassing most conventional CdS-based systems. More importantly, it maintains over 95% of its initial activity after 960 min of continuous illumination, demonstrating exceptional photostability. In contrast, conventionally synthesized CdS typically suffers from rapid PHE activity decay (generally > 50% loss within a few hours) due to severe photocorrosion. The enhanced photostability is attributed to the intrinsic sulfur-coordination directionality of the BDCA process, which minimizes S-vacancy defects, a primary initiation site for photocorrosion. DFT analyses (Fig. 15f–i) reveal that BDCA-synthesized CdS possesses a more robust Cd–S bonding environment and favorable ΔG_{H^*} at interfacial S-sites, further promoting HER kinetics while resisting oxidative degradation. Similarly, for ZnCdS solid solutions, the BDCA method enables the unique controllable-photocorrosion mechanism (Fig. 17l–n), where a sacrificial sulfur-rich surface and a Zn-enriched subsurface work synergistically to enhance both activity and durability. As also shown in Fig. 17i, BDCA-ZnCdS exhibits a 2.5-fold increase in PHE rate over initial cycles, reaching 30.12 mmol g^{-1} h^{-1}, and stabilizes thereafter, a behavior unattainable with conventional extra sulfur source methods.

Therefore, the BDCA solution method is indeed a superior synthesis method for suppressing the photocorrosion issue of MS photocatalysts, which has been strictly proved in CdS and ZnCdS. This intrinsic sulfur-coordination directionality synthesis method not only suppresses defect formation and photocorrosion but enables novel corrosion-mediated activation pathways, establishing it as a superior synthesis strategy for developing highly stable and efficient MS photocatalysts.

5.2.5 Scope and Fundamental Preconditions of the Controllable-Photocorrosion

The advanced controllable-photocorrosion concept, as exemplified by BDCA-synthesized MS photocatalyst of ZnCdS, represents a paradigm shift from perceiving photocorrosion as a purely detrimental process to harnessing it for the functional enhancement. A critical factor that arises is the generalizability of this strategy across broader the variety of MS photocatalysts. The viability of this concept is not universal but hinges upon the fulfillment of several fundamental material prerequisites, which can be speculated from the mechanistic model established for ZnCdS. First, a sacrificial and dynamically renewable surface layer is essential. The initial sulfur-rich surface in BDCA-ZnCdS acts as the designable hole scavenger. This layer is consumed in a controlled path, generating in situ reactive sulfur species that serve as highly active sites for the HER, as confirmed by their near-optimal ΔG_{H^*}. For this mechanism to be replicable in other MS systems, the photocatalyst should either possess or be engineered to develop a surface that can undergo a similar transformation, yielding photocorrosion products that are catalytically beneficial rather than passivating. Second, an intrinsic corrosion-inhibiting barrier is also essential. Specifically, the robust Zn–S bonds in the subsurface region of ZnCdS function as a physical and energetic barrier that confines the corrosive process to the upper layer, which prevents the uncontrolled bulk degradation that plagues conventional MS like CdS. Therefore, extending the advanced concept of controllable-photocorrosion requires the MS photocatalyst to have an inherent structural or compositional feature, such as subsurface layer with significantly stronger metal–sulfur bonds, different crystal phase, or stable secondary compound, that can definitively terminate the corrosion front. For instance, while CdS itself lacks such a barrier, engineering a core–shell or gradient structure with a stable ZnS or Sb_2S_3 core could potentially introduce one. Conversely, materials like MoS_2, with their layered van der Waals structures and inherent stability in reducing environments, may not readily form a sacrificial surface layer, presenting a different set of challenges.

Therefore, the advanced concept of controllable-photocorrosion is most promising for MS photocatalysts whose composition and structure can be facilely and precisely engineered to satisfy the dual criteria: a sacrificially active surface and a structurally robust, corrosion-confining subsurface. This advanced design concept opens a new avenue for a wide range of MS photocatalysts where elemental segregation or gradient synthesis can be exploited. Future research should focus on illustrating the thermodynamic and kinetic boundaries of this phenomenon through coupled theoretical and experimental studies, paving the way for its rational deployment beyond ZnCdS.

https://doi.org/10.1007/s40820-026-02111-0

6 Discussion and Outlooks

The development of photocatalysts combining with exceptional semiconductor properties with high photostability is critical for efficient PHE via water splitting. MS photocatalysts with the narrow-bandgaps, enable visible-light-driven PHE, yet research has largely overlooked a fundamental semiconductor characteristic, electronic dimensionality. MS semiconductors with 3D electronic dimensionality offer lower carrier effective mass, high light absorption coefficient, and unique defect tolerance, collectively boosting the concentration of HER-participating photogenerated electrons, thereby enabling a qualitative leap in PHE efficiency. Equally vital, effectively addressing the persistent challenge of photocorrosion in MS photocatalysts is crucial for ensuring their long-term operational stability. Consequently, building upon the overall summarization of the development route of MS photocatalysts, this review provides a comprehensive analysis of advanced design concept centered on harnessing 3D electronic dimensionality and mitigating photocorrosion, especially controllable-photocorrosion. Key research advancements are systematically examined, encompassing the rational design and PHE application of 3D electronic dimensionality materials exemplified by $CuPbSbS_3$ and innovative synthesis approaches, notably the intrinsic sulfur-coordination-directed method, designed to fundamentally resolve the photocorrosion issue of MS photocatalyst. To quantitatively benchmark the PHE performance advantages conferred by the advanced design concepts, Table 2 comprehensively compares the PHE performance of BDCA-synthesized MS photocatalysts with other state-of-the-art systems, including single-atom-supported MSs, metal–organic frameworks (MOFs), and covalent organic frameworks (COFs). Notably, while certain single-atom, MOFs, or COFs systems exhibit the higher maximum rates, these often require noble-metal cocatalysts (typically Pt) or represent outcomes of extensive, long-term optimization. In contrast, the BDCA-derived MSs, achieving high performance without noble metals in their early development stage, exhibit immense potential. Their unique combination of 3D electronic dimensionality and controllable-photocorrosion mechanisms provides a foundational platform for the rapid, efficient, and stable PHE, positioning them as the highly promising candidates for scale-up solar fuel production. While commendable initial progress has been achieved through these advanced design concepts, considerable room for enhancement remains to realize the ultimate goal of commercially viable PHE technology. Current challenges and future perspectives based on this design concept mainly include the following aspects:

(i) Prioritizing the low-toxic MMS photocatalysts. Current researches have substantiated that the MMS photocatalysts offered superior compositional tunability compared to conventional BMS photocatalysts. This inherent flexibility facilitates the exploration of superior semiconductor properties. Building upon this foundation, the innovative integration of the electronic dimensionality concept has led to the development of $CuPbSbS_3$, a defect-tolerant semiconductor with 3D electronic dimensionality, demonstrating remarkable efficiency in both PHE and Piezo-PD. However, the significant Pb content in $CuPbSbS_3$ raises substantial toxicity concerns, presenting critical impediments to its large-scale PHE implementation. As discussed in Sect. 4.1, the representative 3D electronic dimensionality photocatalyst of $CsPbI_3$ has been extensively explored for PHE application; substitution with Sn produces non-toxic $CsSnI_3$ but sacrifices 3D connectivity (due to Sn valence instability), degrading photocatalytic efficacy [307–310]. In this case, future research is suggested to extend beyond straightforward elemental substitution. A more profound unresolved issue emerges: Can researchers simultaneously achieve environmental sustainability and superior 3D electronic dimensionality by designing novel crystal architectures or exploring specific elemental combinations? This includes, for instance, stabilizing low- or non-toxic elements with similar lone-pair effects or developing entirely Pb-free 3D chalcogenide frameworks. Addressing this challenge needs a fundamental approach rooted in the principles of the atomic orbital interaction. Continuously, combining advanced theoretical calculation methods with high-throughput screening will be further essential to identify low- or non-toxic elements and their corresponding crystal configurations capable of supporting stable, spatially continuous orbital hybridization across all three dimensions. Therefore, the solution of this pivotal issue represents an indispensable step toward translating high-performance, environmen-

Table 1 Comparative performance metrics of BDCA-synthesized and conventional synthesized MS photocatalysts

Photocatalyst	Synthesis method	Defect density (approximate)	PHE rate (mmol g^{-1} h^{-1})	Stability (Cycles/duration)	Key Observations	References
CdS	BDCA	Low (S-vacancy minimized)	7.294	> 95% after 960 min	High phase purity, robust Cd–S bonds	[299]
CdS	Conventional	High (S-vacancy rich)	About 1–4	< 50% after 4–6 h	Rapid photocorrosion, activity decay	[296]
ZnCdS	BDCA	Moderate (engineered)	30.12	2.5 times increase then stable	Controllable-photocorrosion, self-optimizing surface	[84]
ZnCdS	Conventional	High	About 5–15	Gradual decay	Uncontrolled corrosion, bulk degradation	[300]
$CuPbSbS_3$	BDCA	Low (defect-tolerant)	0.2508	~ 82% after 12 h	3D electronic dimensionality, high mobility	[210]

tally benign advanced MS photocatalysts into scale-up applications.

(ii) Development of machine learning (ML) on the design of advanced MS photocatalysts. Advancing photocatalyst design methodologies and deepening the mechanistic comprehension of photocatalytic phenomena are paramount for enhancing photocatalyst efficacy [311–315]. Equally critical is the elucidation of reaction mechanisms and optimization pathways for semiconductor photocatalysts to achieve superior PHE performance. Beyond conventional DFT calculations and experimental refinements, the systematic exploration of materials chemistry space via ML offers a potent strategy for accelerating the discovery and development of advanced semiconductor photocatalysts, a paradigm increasingly validated by contemporary data science research [316–322]. In 2022, Mai et al. highlighted transformative role of ML in advancing photocatalyst discovery, particularly for PHE and PD [323]. Specifically, ML techniques accelerate the screening of complex material spaces by establishing structure–property relationships beyond conventional trial-and-error approaches. For photocatalytic polymers, gradient boosting and random forest models identify critical descriptors like frontier orbital energies and bandgaps, enabling rapid optimization of hydrogen evolution rates. In oxide photocatalysts, ML integrates with DFT and experimental data to optimize bandgap engineering and reaction kinetics in TiO_2 and perovskites, though data scarcity remains a constraint. Significantly, the analysis of BMS and other 2D/3D materials driven by the ML revealed the pivotal influence of structural dimensionality, governing charge carrier mobility, interfacial electron transfer, and light absorption depth. Therefore, future efforts can prioritize machine models incorporating 3D electronic dimensionality descriptors, focusing on orbital overlap or DOS anisotropy, to enable precise design of advanced MS photocatalysts, along with standardizing high-throughput data generation and extending ML to dynamic reaction mechanisms.

(iii) Diversifying MMS photocatalysts synthesis via BDCA. Current researches have demonstrated that the intrinsic sulfur-coordination directionality BDCA solution method can effectively mitigates the photocorrosion issue in traditional BMS photocatalyst of CdS. Building upon this success, the synthesis was extended to MMS photocatalyst of ZnCdS and established the controllable-photocorrosion mechanism that harnesses the beneficial aspects of this typically detrimental phenomenon. Therefore, the versatile solubility of BDCA solution toward various MO and metal hydroxides (Fig. 14b) theoretically enables the synthesis of diverse MMS photocatalysts. To date, only three kinds of MS photocatalysts of $CuPbSbS_3$, CdS, and ZnCdS have been developed for PHE using this approach. Other BMS/MMS materials remain unexplored. Given the intrinsic sulfur-coordination directionality nature of BDCA and the differential solubility of various MO (or metal hydroxides) within it, it is postulated that other BMS/MMS systems fabricated through this route may possess superior band structure characteristics. Consequently, future research should prioritize the diversified synthesis of BMS/MMS photocatalysts

https://doi.org/10.1007/s40820-026-02111-0

Table 2 PHE performance comparison between BDCA-synthesized MS photocatalysts and other representative advanced photocatalysts

Category	Specific photocatalysts	Synthesis method	Bandgap (eV)	PHE rate (mmol g^{-1} h^{-1})	Stability (cycles/duration)	Key Observations	References
Advanced design of MS photocatalysts for PHE	$CuPbSbS_3$	BDCA	1.38	0.2508	~82% after 12 h	3D electronic dimensionality, high mobility	[210]
	CdS	BDCA	~2.4	7.294	> 95% after 960 min	High phase purity, robust Cd–S bonds	[299]
	ZnCdS	BDCA	tunable	30.12	2.5 times increase then stable	Controllable-photocorrosion, self-optimizing surface	[84]
SA[a] supported MS photocatalysts	Ni-SA/$ZnIn_2S_4$	Electrostatic adsorption	~2.5	1.788	6 cycles no decay	Ni-SA anchored on S-vacancy enriched surface; Ni acts as electron trapping center	[362]
	CoP-SA-V_P[b]/$Cd_{0.5}Zn_{0.5}S$	Hydrothermal & phosphorylation	~2.41	68.33	5 cycles (30 h), negligible decay	P-SA vacancies boost charge separation	[363]
	Co-SA/CdS	In situ photochemical anchoring	~2.4	60.10	Stable over 12 h; robust HER durability	Co-SA anchored at V_{Cd}; enhanced H_2O dissociation	[364]
	Pt-SA/$CdIn_2S_4$-V	Impregnation & annealing	~2.16	0.8272	4 cycles stable	Synergy of Pt-SA and V_S enhances charge separation	[365]
	Rh-SA-@MoS_2/ZnCdS-V_S	Hydrothermal & low-temp calcination	2.3	39.827	Slight decay after cycling	Rh-SA & V_S synergistically promote charge separation	[366]
	Rh-SA-ZnCdS-V_S	Hydrothermal & low-temp calcination	~2.3	30.512	~82% after 4 cycles	Rh SA & V_S synergistically promote charge separation	[367]
MOF-based photocatalysts	MoO_3/MIL-125-NH_2	Impregnation	2.65 (MOF)	0.399	5 cycles no decay	First demonstration of band bending in MOFs	[368]
	Pt-SA@Pd-PCN-222-NH_2	Precoordination confinement	~1.96	16.59	7 cycles stable	Synergy of Pt-SA and Pd-porphyrin; high atom utilization	[369]
	COK-47 (Ti-MOF)	Microwave-assisted solvothermal	2.85	4.3	Structure preserved after 14 h irradiation	2D SBU[c] promotes charge separation, LMCT[d] mechanism	[370]
	Au@NH_2-UiO-66/CdS	Self-assembly growth	Visible-light responsive	0.6649	6 cycles stable	LSPR[e]-induced hot electron transfer prolongs carrier lifetime	[371]

Table 2 (continued)

Category	Specific photocatalysts	Synthesis method	Bandgap (eV)	PHE rate (mmol g^{-1} h^{-1})	Stability (cycles/duration)	Key Observations	References
	$Fe_{0.25}Ni_{1.75}$DMBD[f]-NS@CdS	Hydrothermal	1.35 (MOF) 2.41 (CdS)	12.15	3 cycles no decay	Fe/Ni bimetallic synergy, heterojunction-enhanced charge separation	[372]
	C_{60}@NU-901 [g]	Adsorption encapsulation	~1.8	22.3	16 h continuous illumination	Host–guest enhanced built-in electric field	[373]
	HE-MOF-NS[h]	Solvothermal	2.37	13.24	Stable over 4 cycles	High-entropy MOF nanosheets and *p*-type, stable	[374]
	Trimetallic MOF (Cd/Ni/Ho)	One-pot solvothermal by sulfurization	~2.41	40.06	20 h	Synergy of uniformly dispersed photosensitive photothermal sites	[375]
	MIP-209(Ti-Cr)-NO_2[i]	Green solvothermal	3.34	1.1624	4 cycles retained activity	Ti_{12} oxo-cluster, Cr-doped, no noble-metal cocatalyst	[376]
	UiO-66-NM[j]	Post-synthetic modification	-	0.381	Crystallinity retained after 5 cycles	NAD(P)H-mimicking enhances PCET[k] for hydrogen evolution	[377]
	Cu–BCA–Hf–O (MOF)	Stepwise solvothermal	1.42	49.83	No obvious decrease in 5 cycles	Record high activity among pristine MOF, ultra-stable framework	[378]
MOF-based photocatalysts	Sp^2-C-linked triazine-based COF	Gradient heating strategy	1.95	107.38 (with 12 wt% Pt)	89.4% after 5 cycles	Sp^2–C linkage enhances π-delocalization and charge transfer	[379]
	COF-OH-3	Solvothermal	2.28	9.89	30 h stable in 6 cycles	Proton tautomerism tunes band structure	[380]
	Pt clusters on PY-DHBD-COF	In situ photodeposition	2.28	42.432	60 h no significant decay	Uniform Pt clusters via hydroxyl/imine sites	[381]
	TpPa-Cu(II)-COF[m]	Solvothermal synthesis & Cu(II) coordination	~2.0	14.72	Stable for 24 h irradiation	Enantioselective combination enhances hole's extraction	[382]
	Ni-COF-SCAU-1	Acid-catalyzed Schiff reaction	~1.99	197.46 (with 3% Pt)	Excellent stability during reaction	Ni intercalation enhances exciton dissociation and charge transfer	[383]

https://doi.org/10.1007/s40820-026-02111-0

Table 2 (continued)

Category	Specific photocatalysts	Synthesis method	Bandgap (eV)	PHE rate (mmol g^{-1} h^{-1})	Stability (cycles/duration)	Key Observations	References
	Co/Zn-Salen-COF	Schiff-base condensation & metalation	~2.45	1.378	Sustained activity over 20 h	Salen-Co sites in COF framework enable efficient charge transfer	[384]
	TpBpy-Ni2% (Ni-COF)	Solvothermal coordination	1.84	51.3	12 cycles (48 h)	Panchromatic response and efficient MLCT	[385]
	Enaminone-linked COF	Solvothermal method	–	2.396	4 cycles negligible drop	Superior exciton dissociation and high chemical stability	[386]
	Cobaloxime-integrated COF	Covalent click reaction	~1.74–1.95	19	4 cycles stable	Alcohols act as hole scavengers, enhancing charge separation	[387]
	TCDA[o)]-COF	Schiff-base condensation	2.12	23.6	5 cycles ~ 70% activity retained	Partially conjugated linkage; D-π-A structure; High surface area	[388]
	COF-954 (Pt co-catalyst)	Schiff-base condensation	1.97	137.23	Stable over 20 h continuous test	Kagome lattice enhances charge separation	[389]
	Nano-COF	Surfactant-assisted aqueous synthesis	~2.99–2.90	392.0	Sustained H_2 production up to 42 h (rate decline after 20 h)	Nanoscale COFs with enhanced light harvesting and reverse concentration dependence	[390]

a) *SA* singe atom, b) *V*: vacancies (defects), c) *SBU*: secondary building unit, d) *LMCT* ligand to metal charge transfer, e) *LSPR* localized surface plasmon resonance; f) *DMBD* 2,5-dimercapto-1,4-benzenedicarboxylic acid; g) *NU-901* nano-sized zirconium-based MOF, h) *HE-MOF-NS* high-entropy MOF nanosheets, i) *MIP*: materials from institute of porous materials of Paris, j) *NM* nicotinic acid and 3-carboxy-1-methylpyridinium iodide, k) *PCET* proton-coupled electron transfer, l) *PY-DHBD-COF* an adjacent hydroxyl group and imine bond in each constitutional unit (PY: 1,3,6,8-tetra(4-formylphenyl)pyrene and DHBD: 1,4-dihydroxybenzidine), m) *TpPa-Cu(II)-COF* containing phenyl as linker applying as a representative to investigate the coordination structure of the photocatalyst; n) *Ni-COF-SCAU-1* Ni-intercalated fluorenone-based COF, o) *TCDA* three-component donor-π-acceptor

using the BDCA solution method, coupled with joint theoretical–experimental studies to elucidate critical properties such as elemental distribution profiles and carrier transport mechanisms. This approach holds dual promise: substantially suppressing photocorrosion while unlocking the distinctive properties inherent to BDCA-synthesized MS photocatalysts, ultimately advancing highly efficient PHE.

(iv) Further widening the advanced synthesis method with intrinsic sulfur-coordination directionality. Existing research has confirmed that the BDCA solution possesses an intrinsic sulfur-coordination directionality property, which significantly suppresses photocorrosion in MS photocatalysts and substantially enhances their long-term photostability. Notably, the formation and preparation of BDCA solution involve a highly exothermic reaction between CS_2 and $C_4H_{11}N$, necessitating meticulous dropwise addition at approximately one drop per second to mitigate uncontrolled heat release [194]. This procedural constraint, widely documented in studies on BDCA-assisted MS thin-film deposition, imposes inherent limitations on scalability. Consequently, while the BDCA method offers distinct advantages for photocorrosion mitigation, its practical implementation for large-scale PHE is constrained by the vigorous reaction kinetics and slow preparation protocol. Thus, methodological refinements addressing these synthesis challenges remain imperative to unlock the full potential of BDCA-synthesized MS photocatalysts in commercial applications. For instance, Koskela et al. [191] "alkahest" thiol-amine solvent system dissolves diverse metals and chalcogenides, broadening solution-processing flexibility for MS thin films. Nevertheless, analogous to the highly toxic and hazardous hydrazine-based solution methods, the thiol-based solvent systems exhibit significant toxicity and volatility. These inherent drawbacks substantially impede their scalable adoption for synthesizing advanced MS photocatalysts. Therefore, future research on advanced synthetic methodologies should prioritize the exploration of safer and more efficient solution processes while preserving the critical intrinsic sulfur-coordination directionality property. Such developments would concurrently enhance the mitigation of photocorrosion and the strategic utilization of its beneficial aspects, ultimately advancing the efficiency of PHE systems.

(v) Strategic combination of advanced MS photocatalysts with functional materials. Building upon the rational design of advanced MS photocatalysts, further performance enhancements may be achieved through strategic combination with emerging functional materials such as MOFs, COFs, MXenes, and graphitic carbon nitride (g-C_3N_4). These materials offer complementary advantages in PHE applications, as demonstrated in various studies: MOFs and COFs provide ultrahigh surface area, tunable pore structures, and well-defined active sites, which facilitate mass transport and adsorption of reaction intermediates [324–331]. MXenes exhibit metallic conductivity, rich surface chemistry, and excellent charge carrier mobility, enabling efficient electron extraction and transfer [332–337]. Meanwhile, g-C_3N_4 possesses a suitable band structure, high chemical stability, and facile synthesis, making it an attractive component for constructing heterostructures that enhance visible-light absorption and promote charge separation [338–348]. Integrating advanced MS photocatalysts with these functional materials offers a promising pathway toward constructing hierarchical or heterojunction systems with synergistic effects. Such composite architectures could simultaneously enhance light harvesting, improve charge separation efficiency, suppress charge recombination, and increase active sites, collectively contributing to superior PHE performance. In this case, future efforts should focus on the interface engineering, precise band alignment, and understanding the underlying charge transfer mechanisms in these complex systems to unlock their full potential for scale-up PHE applications.

(vi) Focusing on PHE via overall water splitting (PHE-v-OWS). PHE-v-OWS represents the ideal pathway for sustainable hydrogen production, whereas its current efficient realization faces formidable scientific issues [95]. Thermodynamically, PHE-v-OWS is an energetically uphill process ($\Delta G = +237$ kJ mol^{-1}), requiring the photocatalyst with a bandgap that simultaneously straddles the proton reduction (0 V vs. NHE) and water oxidation potentials (1.23 V vs. NHE). Kinetically, this process is severely hampered by the sluggish OER, a complex 4-hole migration process with inherently high activation barriers and slow reaction rates compared to HER. This kinetic difference often leads to the accumulation of photogenerated holes, accelerating charge recombination and undermining PHE-v-OWS efficiency. A further critical challenge is the existence of dissolved oxygen, which acts as an efficient electron scavenger, generating superoxide radicals that not only compete with proton reduction but initiate detrimental side

 https://doi.org/10.1007/s40820-026-02111-0

reactions. At the same time, the most negative factor is the rapid backward reaction, wherein the co-evolved hydrogen and oxygen readily recombine to form water, especially on the surfaces of cocatalysts. This recombination is exacerbated in confined nanosystems and leads to a serious waste of photogenerated charge carriers. Therefore, achieving high PHE-v-OWS efficiency necessitates sophisticated designs for spatial gas separation and meticulous management of reaction microenvironments to suppress these parasitic pathways, making efficient PHE-v-OWS enormously difficult to achieve with current material systems and configurations. The challenges inherent to PHE-v-OWS underscore the necessity for photocatalysts that simultaneously exhibit superior charge transport dynamics and exceptional operational stability. In this case, the strategic construction of 3D electronic dimensionality directly addresses the kinetic limitations of PHE-v-OWS to a large extent. Materials like $CuPbSbS_3$, characterized by isotropic band dispersion and high carrier mobility, facilitate the rapid and balanced extraction of both photogenerated electrons and holes to the surface. This is crucial for PHE-v-OWS, where the slow OER kinetics demand efficient hole delivery to active sites. Meanwhile, resolving the pervasive photocorrosion issue of MS photocatalysts is paramount for long-term viability. Advanced design concepts, such as the controllable-photocorrosion mechanism or synthesis methods fostering intrinsic sulfur-coordination directionality, prevent the oxidative degradation of the lattice of MS photocatalysts. When integrated, a photocatalyst endowed with a robust 3D electronic network and corrosion-resistant architecture ensures sustained charge flux for both HER and OER while maintaining structural integrity under prolonged illumination. This synergistic combination of efficient bulk charge transport and durable surface chemistry represents a critical foundational step toward developing viable MS photocatalysts for efficient and stable PHE-v-OWS.

(vii) Toward practical hydrogen production: Natural sunlight and seawater splitting. Although significant research progresses have been achieved in the advanced design of MS photocatalysts, their evaluation mainly performs under the ideal laboratory conditions, using simulated sunlight and pure water with sacrificial reagents. Further, translating these advancements to practical and scale-up PHE needs facing the complexities of real-condition operation: the uncertain spectrum and intensity of natural sunlight and the challenging chemical environment of seawater [349–356]. Specifically, the utilization of natural sunlight introduces the dynamic variables beyond the simulation sunlight of standardized AM 1.5G. The diurnal/seasonal differences in irradiance intensity and spectral composition directly impact the reaction kinetics and stability of PHE [354]. Practical PHE application demonstrations, such as the 100 m^2 panel reactor array employing $SrTiO_3$:Al, demonstrate the engineering challenges and efficiency penalties associated with outdoor operation, where the achieved the solar-to-hydrogen (STH) efficiencies are often sigificantly lower than peak lab-based values [352]. For the advanced MS photocatalysts, whose photocatalytic performance and photostability are sensitive to photon flux and local temperature, designing systems that maintain optimal function under these uncertain conditions is crucial. Strategies may include the adaptive thermal management, harnessing infrared radiation for beneficial temperature control as demonstrated with the InGaN/GaN systems [357], and developing photocatalysts with broad spectral response to the maximize energy harvesting across the solar spectrum. At the same time, direct PHE via seawater splitting (PHE-v-SS) represents a strong yet highly desirable pathway, given the abundance of seawater resources in the Earth [353, 354]. However, the high ionic strength, existence of corrosive chloride ions, and dissolved organic matter generally lead to the photocatalyst poisoning, accelerated photocorrosion of MS, and competitive side reactions. Recent advances have highlighted both the challenges and opportunities of PHE-v-SS. For instance, ions like Na^+ can enhance interfacial processes or scavenge holes to a certain extent, while others like Mg^{2+} or Ca^{2+} may precipitate with common sacrificial reagents, stabilizing the photocatalytic system [351]. Innovative and advanced photocatalyst design is key to overcoming these issues. Typically, the construction of Schottky junctions with plasmonic metals on vacancy-engineered sulfides has proven effective, not only enhancing charge separation via hot electron injection but forming a protective layer that mitigates chloride-induced corrosion, enabling remarkable PHE rates in simulated seawater [353]. This result proves a move beyond mere corrosion suppression toward the functional integration of protective and photocatalytic components. Therefore, future research direction for MS photocatalysts can bridge the gap between idealized conditions and application-ready performance,

which involves several key factors: developing photocatalytic measurement conditions that account for real sunlight variability and complex aqueous matrices like real seawater, moving beyond standard sacrificial reagents systems in pure water; designing the stable composite architectures that synergize 3D electronic dimensionality for efficient charge migration with specifically engineered interfaces, such as corrosion-resistant cocatalysts or selective films, to maintain the photocatalytic performance in the harsh chemical environments and suppress ion poisoning; integrating system-level engineering, including efficient gas separation films and strategies to manage the salinity gradients in seawater, as pioneered in scale-up panel reactors. By coupling advanced design concepts of 3D electronic dimensionality and controllable-photocorrosion with solutions addressing these practical constraints, advanced MS-based photocatalytic systems have great potential to evolving from a promising laboratory phenomenon into a viable technology for sustainable PHE application using natural resources.

(viii) Extending design principles to photocatalytic CO_2 reduction. In parallel to the advancements in PHE, the advanced design concept of MS photocatalysts emphasizing on 3D electronic dimensionality and controllable-photocorrosion are also demonstrating profound applicability in photocatalytic CO_2 conversion, opening a new avenue for sustainable fuel and chemical production. The construction of 3D electronic dimensionality, as exemplified in perovskite-inspired systems and tailored MMS photocatalyst, facilitates isotropic charge transport and minimized carrier effective mass, which are equally critical for activating inert CO_2 molecules and stabilizing multi-electron intermediates required for C–C coupling. Recent breakthroughs in photocatalyst design for photocatalytic CO_2 reduction, including the Co^0–$Co^{\delta+}$ double-site interfaces for photothermal C–C coupling into light olefins and electron-enriched Bi active sites in BiOCl atomic layers for CO_2 splitting [358, 359], alongside advancements in electronic restructuring of RuCu alloys for methanol selectivity [360], collectively validate that engineered electronic structures, akin to 3D electronic dimensionality, are essential in guiding the reaction pathways and lowering energy barriers for CO_2 conversion to multi-carbon products and oxygenates [361]. Moreover, the emerging controllable-photocorrosion paradigm, initially developed for MS-based PHE, also offers a transformative strategy to harness surface dynamics in CO_2 conversion, where in situ formed sulfur-rich layers or defect-engineered surfaces can act as self-optimizing active sites rather than degradation centers. This synergy between 3D electronic connectivity and controllable-photocorrosion strategies not only addresses the inherent instability of MSs under photo-oxidative conditions but unlocks new reaction pathways of photocatalytic CO_2 reduction to methanol or long-chain hydrocarbons. Integrating these advanced design concepts into photocatalytic CO_2 reduction systems can thus accelerate the development of stable, efficient, and scalable MS-based photocatalysts for solar-to-chemical energy conversion, bridging the gap between hydrogen evolution and carbon–neutral synthesis.

Acknowledgements This work was supported by the National Natural Science Foundation of China (22469007, 22202053, 52304326, 22309037, 22305055, 52362010, 22462006, 22462008), the Start-up Research Foundation of Hainan University (KYQD(ZR)-21065, XJ2500008500), the Collaborative Innovation Center of Tropical Marine Science and Technology, Hainan University (XTCX2022HYC21, XTCX2022HYC05), the first batch of "Nanhai New Star" industrial innovation talent platform project (NHXXRCXM202309006), and the specific research fund of The Innovation Platform for Academicians of Hainan Province. The numerical computations were performed at the Hefei Advanced Computing Center. The authors acknowledge the support for comprehensive characterizations by Pico Election Microscopy Center of Hainan University.

Author Contributions Qizhi Gao involved in conceptualization, investigation, writing—original draft; Xinlong Zheng took part in writing—original draft; Jiaxin Lin carried out writing—original draft; Jiadi, Zhai took part in supervision; Fan Yang took part in supervision; Xinjie Chen took part in supervision; Minghui Wang involved in supervision; Miaomiao Yang took part in supervision; Jing Li took part in supervision; Xiaodong Shi took part in supervision; Yonghao Xiao carried out conceptualization, project administration, investigation, writing—original draft, writing—review & editing; Xinlong Tian took part in conceptualization, funding acquisition, investigation, project administration, supervision, writing—original draft, writing—review & editing; Yuhao Liu took part in conceptualization, funding acquisition, investigation, project administration, supervision, writing—original draft, writing—review & editing.

Declarations

Conflict of interest The authors declare no conflict of interest. They have no known competing financial interests or personal relationships that could have influenced the work reported in this paper.

https://doi.org/10.1007/s40820-026-02111-0

References

1. T. Huang, B. Gao, S. Zhao, H. Zhang, X. Li et al., All-MXenes zinc ion hybrid micro-supercapacitor with wide voltage window based on V_2CTx cathode and $Ti_3C_2T_x$ anode. Nano Energy **111**, 108383 (2023). https://doi.org/10.1016/j.nanoen.2023.108383
2. J. Liu, Y. Jiang, X. Zhang, L. Fu, M. Deng, Performance optimization of an HT-PEMFC and PSA integrated system with impure hydrogen containing CO_2. Appl. Therm. Eng. **214**, 118859 (2022). https://doi.org/10.1016/j.applthermaleng.2022.118859
3. Y. Zhang, Y. Cheng, Q. Zhang, W. He, Y. Wang et al., Hyperstable low-tortuosity fast ion nanochannels for MXene electrodes. Energy Storage Mater. **73**, 103829 (2024). https://doi.org/10.1016/j.ensm.2024.103829
4. J. Du, F. Jin, Y. Li, G. Jiang, Z. Jin, *In situ* Mo doping in NiS_2: enhancing electron density and stimulating electronic conductivity of Cu_3P–GDY for efficient photocatalytic hydrogen evolution. J. Mater. Chem. A **13**(7), 4994–5006 (2025). https://doi.org/10.1039/d4ta07562e
5. W. Yin, H. Luo, L. Yuan, Y. Sun, X. Yang et al., Hydrophobic interface layer improves the moisture tolerance and efficiency of ambient air-processed perovskite solar cells. Fundam. Res. (2024). https://doi.org/10.1016/j.fmre.2024.12.013
6. T. Gao, D. Jiao, L. Wang, X. Ge, X. Wen et al., Switchable acidic oxygen evolution mechanisms on atomic skin of ruthenium metallene oxides. J. Am. Chem. Soc. **147**(5), 4159–4166 (2025). https://doi.org/10.1021/jacs.4c13656
7. X. Wang, S. Xue, T. Shi, Z. Zhao, A. Song et al., Localized phosphorization manipulating internal electric field orientation in carbon nitride homojunction for efficient photocatalytic hydrogen evolution. Adv. Funct. Mater. **35**(35), 2424853 (2025). https://doi.org/10.1002/adfm.202424853
8. Y. Zhao, M. Hu, H. Li, B. Chu, Y. Huang et al., The role of adsorbed hydroxide reduction in hydrogen evolution and nitrogen reduction reactions in aqueous solution. J. Mater. Chem. A **10**(36), 18609–18615 (2022). https://doi.org/10.1039/D2TA04867A
9. S. Chen, W. Liu, M. Xu, P. Shi, M. Zhu, Electrospray prepared flexible $CsPbBr_3$ perovskite film for efficient X-ray detection. J. Mater. Chem. C **11**(25), 8431–8437 (2023). https://doi.org/10.1039/d3tc01347b
10. Z. Xie, H. Luo, Q.-S. Jiang, Y. Zhao, Y. Peng et al., A universal reverse-cool annealing strategy makes two-dimensional Ruddlesden-popper perovskite solar cells stable and highly efficient with V_{oc} exceeding 1.2 V. EcoMat **6**(12), e12501 (2024). https://doi.org/10.1002/eom2.12501
11. M. Li, S. Yu, H. Huang, Emerging polynary bismuth-based photocatalysts: structural classification, preparation, modification and applications. Chin. J. Catal. **57**, 18–50 (2024). https://doi.org/10.1016/S1872-2067(23)64593-0
12. C. Cheng, B. He, J. Fan, B. Cheng, S. Cao et al., An inorganic/organic S-scheme heterojunction H_2-production photocatalyst and its charge transfer mechanism. Adv. Mater. **33**(22), 2100317 (2021). https://doi.org/10.1002/adma.202100317
13. W. He, L. Xu, G. Yu, K. Wang, D. Bao et al., Linear enhanced 3D nanofluid force-electric conversion device. Adv. Mater. **37**(8), e2417498 (2025). https://doi.org/10.1002/adma.202417498
14. Y. Gao, T. Song, X. Guo, Y. Zhang, Y. Yang, Electronic interaction and oxygen vacancy engineering of g-C_3N_4/α-Bi_2O_3 Z-scheme heterojunction for enhanced photocatalytic aerobic oxidative *homo-*/ hetero-coupling of amines to imines in aqueous phase. Green Carbon **1**(2), 105–117 (2023). https://doi.org/10.1016/j.greenca.2023.09.004
15. J. Chen, X. Shi, S. Feng, J. Li, X. Gao et al., Design of highly active and durable oxygen evolution catalyst with intrinsic chlorine inhibition property for seawater electrolysis. Nano Mater. Sci. **6**(4), 413–418 (2024). https://doi.org/10.1016/j.nanoms.2023.10.003
16. X. Sun, S. Jiang, H. Huang, H. Li, B. Jia et al., Solar energy catalysis. Angew. Chem. Int. Ed. **61**(29), e202204880 (2022). https://doi.org/10.1002/anie.202204880
17. X. Wang, T. Shi, X. Wang, A. Song, G. Li et al., Insight into the synergistic effect of defect and strong interface coupling on $ZnIn_2S_4$/$CoIn_2S_4$ heterostructure for boosting photocatalytic H_2 evolution. J. Energy Chem. **92**, 151–161 (2024). https://doi.org/10.1016/j.jechem.2023.12.040
18. D. Liu, Y. Zhao, C. Wu, W. Xu, S. Xi et al., Triggering electronic coupling between neighboring hetero-diatomic metal sites promotes hydrogen evolution reaction kinetics. Nano Energy **98**, 107296 (2022). https://doi.org/10.1016/j.nanoen.2022.107296
19. M. Xu, X. Ruan, D. Meng, G. Fang, D. Jiao et al., Modulation of sulfur vacancies in $ZnIn_2S_4$/MXene Schottky heterojunction photocatalyst promotes hydrogen evolution. Adv. Funct. Mater. **34**(37), 2402330 (2024). https://doi.org/10.1002/adfm.202402330
20. B. Xu, Y. Li, P. Hong, P. Zhang, J. Han et al., Pressure-controlled free exciton and self-trapped exciton emission in quasi-one-dimensional hybrid lead bromides. Nat. Commun. **15**(1), 7403 (2024). https://doi.org/10.1038/s41467-024-51836-2

21. T. Chen, F. Chen, C. Wang, C. Hu, N. Tian et al., Identifying polar and non-polar octahedron units in isomorphic layered perovskites towards efficient piezocatalytic H_2 evolution. Nano Energy **131**, 110334 (2024). https://doi.org/10.1016/j.nanoen.2024.110334
22. S. Cao, H. Li, T. Tong, H.-C. Chen, A. Yu et al., Photocatalysis: single-atom engineering of directional charge transfer channels and active sites for photocatalytic hydrogen evolution. Adv. Funct. Mater. **28**(32), 1870224 (2018). https://doi.org/10.1002/adfm.201870224
23. Z. Zhu, J. Hu, C. Hu, Y. Lu, S. Chu et al., Oriented crystal polarization tuning bulk charge and single-site chemical state for exceptional hydrogen photo-production. Adv. Mater. **36**(47), 2411339 (2024). https://doi.org/10.1002/adma.202411339
24. M. Wang, C. Chen, Y. Zhang, Y. Ma, L. Xu et al., Flexible monolithic 3D-integrated self-powered tactile sensing array based on holey MXene paste. Nano-Micro Lett. **18**(1), 68 (2025). https://doi.org/10.1007/s40820-025-01924-9
25. T. Hisatomi, K. Takanabe, K. Domen, Photocatalytic water-splitting reaction from catalytic and kinetic perspectives. Catal. Lett. **145**(1), 95–108 (2015). https://doi.org/10.1007/s10562-014-1397-z
26. R. Changotra, A.K. Ray, Q. He, Establishing a water-to-energy platform *via* dual-functional photocatalytic and photoelectrocatalytic systems: a comparative and perspective review. Adv. Colloid Interface Sci. **309**, 102793 (2022). https://doi.org/10.1016/j.cis.2022.102793
27. X. Li, X. Wu, Y. Zhao, Y. Lin, J. Zhao et al., Promoting oxygen reduction reaction by inducing out-of-plane polarization in a metal phthalocyanine catalyst. Adv. Mater. **35**(30), e2302467 (2023). https://doi.org/10.1002/adma.202302467
28. Y. Xiao, C. Yao, C. Su, B. Liu, Nanoclusters for photoelectrochemical water splitting: bridging the photosensitizer and carrier transporter. EcoEnergy **1**(1), 60–84 (2023). https://doi.org/10.1002/ece2.6
29. H. Su, W. Wang, R. Shi, H. Tang, L. Sun et al., Recent advances in quantum dot catalysts for hydrogen evolution: synthesis, characterization, and photocatalytic application. Carbon Energy **5**(9), e280 (2023). https://doi.org/10.1002/cey2.280
30. Y. Guo, X. Tong, N. Yang, Photocatalytic and electrocatalytic generation of hydrogen peroxide: principles, catalyst design and performance. Nano-Micro Lett. **15**(1), 77 (2023). https://doi.org/10.1007/s40820-023-01052-2
31. A. Fujishima, K. Honda, Electrochemical photolysis of water at a semiconductor electrode. Nature **238**(5358), 37–38 (1972). https://doi.org/10.1038/238037a0
32. J. Schneider, M. Matsuoka, M. Takeuchi, J. Zhang, Y. Horiuchi et al., Understanding TiO_2 photocatalysis: mechanisms and materials. Chem. Rev. **114**(19), 9919–9986 (2014). https://doi.org/10.1021/cr5001892
33. B. Wei, M. Calatayud, Hydrogen activation on Anatase TiO_2: effect of surface termination. Catal. Today **397**, 113–120 (2022). https://doi.org/10.1016/j.cattod.2021.11.020
34. A. Kubacka, M. Fernández-García, G. Colón, Advanced nanoarchitectures for solar photocatalytic applications. Chem. Rev. **112**(3), 1555–1614 (2012). https://doi.org/10.1021/cr100454n
35. X. Ruan, S. Li, C. Huang, W. Zheng, X. Cui et al., Catalyzing artificial photosynthesis with TiO_2 heterostructures and hybrids: emerging trends in a classical yet contemporary photocatalyst. Adv. Mater. **36**(17), e2305285 (2024). https://doi.org/10.1002/adma.202305285
36. Y. Pan, W. Liang, Z. Wang, J. Gong, Y. Wang et al., Facile synthesis of Pt clusters decorated TiO_2 nanoparticles for efficient photocatalytic degradation of antibiotics. Interdiscip. Mater. **3**(6), 935–945 (2024). https://doi.org/10.1002/idm2.12203
37. W. Liu, P. Shi, X. Tian, X. He, L. Li, High-performance asymmetric pseudocapacitor based on $NiCo_2O_4$@MnO_2 cathode and N-doped graphene anode. J. Electroanal. Chem. **960**, 118216 (2024). https://doi.org/10.1016/j.jelechem.2024.118216
38. Z. Zhou, Z. Jin, Designed of dual direct band gap graphdiyne/Co_2VO_4 S-scheme heterojunction: enhance the bonding stability of Co active sites to promote photocatalytic hydrogen evolution. Chem. Eng. J. **500**, 157514 (2024). https://doi.org/10.1016/j.cej.2024.157514
39. C. Ding, X. Ruan, M. Xu, D. Meng, G. Fang et al., Step-scheme SnO_2/$Zn_3In_2S_6$ catalysts for solar production of hydrogen peroxide from seawater. Small **20**(50), e2406959 (2024). https://doi.org/10.1002/smll.202406959
40. P. Su, D. Zhang, M. Zhu, T. Liang, N. Yang et al., Reusable $Cd_{0.9}Zn_{0.1}S$-ZnO@C/PVDF piezo-photocatalytic film with exceptional hydrogen evolution capability triggered by the synergetic advantages of piezoelectricity and S-Scheme heterojunction. J. Energy Chem. **96**, 164–176 (2024). https://doi.org/10.1016/j.jechem.2024.04.027
41. P. Wang, R. Shi, Y. Zhao, Z. Li, J. Zhao et al., Selective photocatalytic oxidative coupling of methane *via* regulating methyl intermediates over metal/ZnO nanoparticles. Angew. Chem. Int. Ed. **62**(23), e202304301 (2023). https://doi.org/10.1002/anie.202304301
42. J. Liu, Q. Zhang, X. Tian, Y. Hong, Y. Nie et al., Highly efficient photocatalytic degradation of oil pollutants by oxygen deficient SnO_2 quantum dots for water remediation. Chem. Eng. J. **404**, 127146 (2021). https://doi.org/10.1016/j.cej.2020.127146
43. S. Qin, Q. Chen, C. Huang, J. Li, Y. Shi et al., Construction of 3D/2D CeO_2/Bi_2MoO_6 S-scheme heterojunction for photocatalytic cascade reactions of secondary amines synthesis. Rare Met. (2025). https://doi.org/10.1007/s12598-025-03648-6
44. Y. Shi, P. Li, H. Chen, Z. Wang, Y. Song et al., Photocatalytic toluene oxidation with nickel-mediated cascaded active units over Ni/Bi_2WO_6 monolayers. Nat. Commun. **15**(1), 4641 (2024). https://doi.org/10.1038/s41467-024-49005-6
45. T. Hang, L. Wu, W. Liu, L. Yang, T. Zhang, Research progress of bifunctional photocatalysts for biomass conversion

 https://doi.org/10.1007/s40820-026-02111-0

and fuel production. Adv. Energy Sustain. Res. **5**(10), 2400069 (2024). https://doi.org/10.1002/aesr.202400069

46. H. Cao, F. Su, L. Wang, Y. Zhang, Y. Xiao et al., Deficient MoO_2 facilitating photothermal synergetic catalytic CO_2 reduction selectively to CO over P-doped g-C_3N_4. Vacuum **238**, 114262 (2025). https://doi.org/10.1016/j.vacuum.2025.114262
47. T. Xiang, T. Liu, T. Ouyang, S. Zhao, Z.-Q. Liu, Tuning the selectivity of CO_2 conversion to CO on partially reduced Cu_2O/ZnO heterogeneous interface. Interdiscip. Mater. **3**(3), 380–388 (2024). https://doi.org/10.1002/idm2.12157
48. X. Chen, S. Shen, L. Guo, S.S. Mao, Semiconductor-based photocatalytic hydrogen generation. Chem. Rev. **110**(11), 6503–6570 (2010). https://doi.org/10.1021/cr1001645
49. L. Fu, H. Liu, J. Liu, Z. Hua, H. Lin, Research on the effect of connected cable-type channel structure and flow field arrangement on the performance of SOFC. Int. J. Hydrog. Energy **78**, 169–179 (2024). https://doi.org/10.1016/j.ijhydene.2024.06.159
50. X. Tu, X. Liu, Y. Zhang, J. Zhu, H. Jiang, Advances in Sn-based oxide catalysts for the electroreduction of CO_2 to formate. Green Carbon **2**(2), 131–148 (2024). https://doi.org/10.1016/j.greenca.2024.03.006
51. Z. Liang, Y. Xue, X. Wang, X. Zhang, J. Tian et al., The incorporation of cocatalyst cobalt sulfide into graphitic carbon nitride: boosted photocatalytic hydrogen evolution performance and mechanism exploration. Nano Mater. Sci. **5**(2), 202–209 (2023). https://doi.org/10.1016/j.nanoms.2022.03.001
52. D. Gao, W. Zhong, X. Zhang, P. Wang, H. Yu, Free-electron inversive modulation to charge antibonding orbital of ReS_2 cocatalyst for efficient photocatalytic hydrogen generation. Small **20**(13), e2309123 (2024). https://doi.org/10.1002/smll.202309123
53. W. Wang, Y. Li, J. Zhu, B. Cheng, S. Zhang et al., Organic-inorganic CdS/CBT S-scheme heterojunction with enhanced charge transfer for efficient photocatalytic hydrogen production. InfoScience **2**(1), e70000 (2025). https://doi.org/10.1002/inc2.70000
54. H. Hu, X. Zhang, K. Zhang, Y. Ma, H. Wang et al., Construction of a 2D/2D crystalline porous materials based S-scheme heterojunction for efficient photocatalytic H_2 production. Adv. Energy Mater. **14**(11), 2303638 (2024). https://doi.org/10.1002/aenm.202303638
55. D. Huang, M. Wen, C. Zhou, Z. Li, M. Cheng et al., $Zn_xCd_{1-x}S$ based materials for photocatalytic hydrogen evolution, pollutants degradation and carbon dioxide reduction. Appl. Catal. B Environ. **267**, 118651 (2020). https://doi.org/10.1016/j.apcatb.2020.118651
56. X. Zheng, Y. Yang, Y. Song, Z. Ma, Q. Gao et al., Recent advances in photocatalytic hydrogen evolution of AgIn5S8-based photocatalysts. Interdiscip. Mater. **2**(5), 669–688 (2023). https://doi.org/10.1002/idm2.12120
57. M. Li, H. Li, H. Fan, Q. Liu, Z. Yan et al., Engineering interfacial sulfur migration in transition-metal sulfide enables low overpotential for durable hydrogen evolution in seawater. Nat. Commun. **15**(1), 6154 (2024). https://doi.org/10.1038/s41467-024-50535-2
58. R. Pan, M. Hu, J. Liu, D. Li, X. Wan et al., Two-dimensional all-in-one sulfide monolayers driving photocatalytic overall water splitting. Nano Lett. **21**(14), 6228–6236 (2021). https://doi.org/10.1021/acs.nanolett.1c02008
59. B. Ge, C. Li, W. Lu, H. Ye, R. Li et al., Dynamic phase transition leading to extraordinary plastic deformability of thermoelectric $SnSe_2$ single crystal. Adv. Energy Mater. **13**(27), 2300965 (2023). https://doi.org/10.1002/aenm.202300965
60. W. Zhong, J. Xu, X. Zhang, J. Zhang, X. Wang et al., Charging d-orbital electron of ReS_{2+x} cocatalyst enables splendid alkaline photocatalytic H_2 evolution. Adv. Funct. Mater. **33**(36), 2302325 (2023). https://doi.org/10.1002/adfm.202302325
61. T. Fatima, S. Husain, M. Khanuja, Novel ternary Z scheme carbon quantum dots (CQDs) decorated WS_2/PANI ((CQDs@WS_2/PANI): 0D: 2D: 1D) nanocomposite for the photocatalytic degradation and electrochemical detection of pharmaceutical drugs. Nano Mater. Sci. **7**(2), 259–275 (2025). https://doi.org/10.1016/j.nanoms.2024.04.005
62. X. Ruan, S. Zhao, M. Xu, D. Jiao, J. Leng et al., Iso-elemental $ZnIn_2S_4$/$Zn_3In_2S_6$ heterojunction with low contact energy barrier boosts artificial photosynthesis of hydrogen peroxide. Adv. Energy Mater. **14**(36), 2401744 (2024). https://doi.org/10.1002/aenm.202401744
63. X. Zheng, Y. Song, C. Wang, Q. Gao, Z. Shao et al., Properties, applications, and challenges of copper- and zinc-based multinary metal sulfide photocatalysts for photocatalytic hydrogen evolution. Chin. J. Catal. **74**, 22–70 (2025). https://doi.org/10.1016/S1872-2067(25)64720-6
64. X.-L. Zheng, Y.-J. Yang, Y.-H. Liu, P.-L. Deng, J. Li et al., Fundamentals and photocatalytic hydrogen evolution applications of quaternary chalcogenide semiconductor: Cu_2ZnSnS_4. Rare Met. **41**(7), 2153–2168 (2022). https://doi.org/10.1007/s12598-021-01955-2
65. Y. Song, X. Zheng, Y. Yang, Y. Liu, J. Li et al., Heterojunction engineering of multinary metal sulfide-based photocatalysts for efficient photocatalytic hydrogen evolution. Adv. Mater. **36**(11), e2305835 (2024). https://doi.org/10.1002/adma.202305835
66. F. Gao, W.-G. Cui, X. Wang, Z. Li, Y. Chen et al., Harnessing hydrogen spillover by lattice strain for enhanced photocatalytic hydrogen evolution of $ZnIn_2S_4$. ACS Catal. **15**(3), 2367–2379 (2025). https://doi.org/10.1021/acscatal.4c07308
67. W. Yang, G. Ma, Y. Fu, K. Peng, H. Yang, X. Zhan, W. Yang, L. Wang, H. Hou, Rationally designed Ti_3C_2 MXene@ TiO_2/$CuInS_2$ Schottky/S-scheme integrated heterojunction for enhanced photocatalytic hydrogen evolution. Chem. Eng. J. **429**, 132381 (2022). https://doi.org/10.1016/j.cej.2021.132381
68. M. Abbas, S. Chen, Z. Li, M. Ishaq, Z. Zheng et al., Highest solar-to-hydrogen conversion efficiency in Cu_2ZnSnS_4 photocathodes and its directly unbiased solar seawater splitting. Nano-Micro Lett. **17**(1), 257 (2025). https://doi.org/10.1007/s40820-025-01755-8

69. Y. Xie, X. Wang, Thermal conductivity of carbon-based nanomaterials: deep understanding of the structural effects. Green Carbon **1**(1), 47–57 (2023). https://doi.org/10.1016/j.greenca.2023.08.004
70. Y. Xiao, M. Wang, D. Liu, J. Gao, J. Ding et al., Selective photoelectrochemical oxidation of glycerol to glyceric acid on (002) facets exposed WO_3 nanosheets. Angew. Chem. Int. Ed. **63**(11), e202319685 (2024). https://doi.org/10.1002/anie.202319685
71. J. Wu, M. Liu, J. Fan, Y. Qiu, W. Lu et al., Amorphization-driven RhRu bimetallene enhances water dissociation kinetics. Adv. Funct. Mater. **34**(51), 2409825 (2024). https://doi.org/10.1002/adfm.202409825
72. X. Wang, T. Shi, X. Wang, G. Li, L. Wang et al., Low-valent cation doping and leaching to construct single-atom Cu decorated Cu-$ZnIn_2S_4$ with multiple defects for boosting photocatalytic H_2 evolution. Appl. Catal. B Environ. Energy **348**, 123807 (2024). https://doi.org/10.1016/j.apcatb.2024.123807
73. D. Zhang, P. Chen, R. Qin, H. Li, X. Pu et al., Effect of surface carbon layer on hydrogen evolution activity of $NiFe_2O_4$@C/$Cd_{0.9}Zn_{0.1}S$ S-scheme heterojunction photocatalyst. Appl. Catal. B Environ. Energy **361**, 124690 (2025). https://doi.org/10.1016/j.apcatb.2024.124690
74. C. Zhu, J. Yang, J. Zhang, X. Wang, Y. Gao et al., Single-atom materials: the application in energy conversion. Interdiscipl. Mater. **3**(1), 74–86 (2024). https://doi.org/10.1002/idm2.12141
75. Y. Jin, D. Zheng, Z. Fang, Z. Pan, S. Wang et al., Salt-melt synthesis of poly(heptazine imide) in binary alkali metal bromides for enhanced visible-light photocatalytic hydrogen production. Interdiscip. Mater. **3**(3), 389–399 (2024). https://doi.org/10.1002/idm2.12159
76. Y.-Y. Cheng, X.-T. Li, C.-L. Yang, X. Li, W. Zhao et al., Tunable Z-scheme photocatalytic activity in $Sc_2CBrX/MoTe_2$ (X = Br, Cl) heterostructures: a combined electronic and nonadiabatic dynamics study. J. Mater. Chem. A **13**(43), 37385–37395 (2025). https://doi.org/10.1039/D5TA05410A
77. S.U. Rehman, J. Wang, G. Wu, S. Ali, J. Xian et al., Unraveling the photocatalytic potential of transition metal sulfide and selenide monolayers for overall water splitting and photocorrosion inhibition. J. Mater. Chem. A **12**(11), 6693–6702 (2024). https://doi.org/10.1039/D3TA07106E
78. W. Cai, Z. Qian, C. Hu, W. Zheng, L. Luo et al., Systematic investigation of MoS_2-metal sulfides (Metal = In, Sn, Cu, Cd) heterostructure *via* metal-sulfur bond for photocatalytic CO_2 reduction. Chem. Eng. J. **479**, 147718 (2024). https://doi.org/10.1016/j.cej.2023.147718
79. M.A. Rehan, H. Liang, G. Li, Synergistic role of plasmonic Au-doped MOF with $ZnIn_2S_4/MoS_2$ nanosheets for boosted photocatalytic hydrogen evolution. Nano Mater. Sci. **7**(4), 482–492 (2025). https://doi.org/10.1016/j.nanoms.2024.06.001
80. J. Xu, W. Zhong, X. Zhang, X. Wang, X. Hong et al., Triggering the channel-sulfur sites in 1T′- ReS_2 cocatalyst toward splendid photocatalytic hydrogen generation. Small **19**(45), 2303960 (2023). https://doi.org/10.1002/smll.202303960
81. Z. Xiao, W. Meng, J. Wang, D.B. Mitzi, Y. Yan, Searching for promising new perovskite-based photovoltaic absorbers: the importance of electronic dimensionality. Mater. Horiz. **4**(2), 206–216 (2017). https://doi.org/10.1039/c6mh00519e
82. J. Hoffman, X. Che, S. Sidhik, X. Li, I. Hadar et al., From 2D to 1D electronic dimensionality in halide perovskites with stepped and flat layers using propylammonium as a spacer. J. Am. Chem. Soc. **141**(27), 10661–10676 (2019). https://doi.org/10.1021/jacs.9b02846
83. Q. Luo, D. Xie, Y. Tian, C. Zhang, D. Cao et al., Unravelling phase-dependent electronic dimensionality and optoelectronic properties in lead-free layered $A_3B_2X_9$ perovskites for photovoltaic applications. J. Mater. Chem. C **12**(33), 13061–13072 (2024). https://doi.org/10.1039/D4TC01803F
84. X. Zheng, Y. Song, Q. Gao, J. Lin, J. Zhai et al., Controllable-photocorrosion balance endows ZnCdS stable photocatalytic hydrogen evolution. Adv. Funct. Mater. **35**(39), 2506159 (2025). https://doi.org/10.1002/adfm.202506159
85. S. Chandrasekaran, L. Yao, L. Deng, C. Bowen, Y. Zhang et al., Recent advances in metal sulfides: from controlled fabrication to electrocatalytic, photocatalytic and photoelectrochemical water splitting and beyond. Chem. Soc. Rev. **48**(15), 4178–4280 (2019). https://doi.org/10.1039/C8CS00664D
86. X. Zheng, Y. Song, Y. Liu, Y. Yang, D. Wu et al., $ZnIn_2S_4$-based photocatalysts for photocatalytic hydrogen evolution *via* water splitting. Coord. Chem. Rev. **475**, 214898 (2023). https://doi.org/10.1016/j.ccr.2022.214898
87. Y. Yang, X. Zheng, Y. Song, Y. Liu, D. Wu et al., $CuInS_2$-based photocatalysts for photocatalytic hydrogen evolution *via* water splitting. Int. J. Hydrog. Energy **48**(10), 3791–3806 (2023). https://doi.org/10.1016/j.ijhydene.2022.10.253
88. R. Yang, L. Mei, Y. Fan, Q. Zhang, R. Zhu et al., $ZnIn_2S_4$-based photocatalysts for energy and environmental applications. Small Methods **5**(10), 2100887 (2021). https://doi.org/10.1002/smtd.202100887
89. J. Wang, S. Sun, R. Zhou, Y. Li, Z. He et al., A review: synthesis, modification and photocatalytic applications of $ZnIn_2S_4$. J. Mater. Sci. Technol. **78**, 1–19 (2021). https://doi.org/10.1016/j.jmst.2020.09.045
90. Y. Ma, Z. Feng, Y. Dong, Z. Yan, H. Wang et al., Harnessing the interfacial sulfur-edge and metal-edge sites in $ZnIn_2S_4$/MnS heterojunctions boosts charge transfer for photocatalytic hydrogen production. Chin. Chem. Lett. **36**(6), 110922 (2025). https://doi.org/10.1016/j.cclet.2025.110922
91. A.J. Esswein, D.G. Nocera, Hydrogen production by molecular photocatalysis. Chem. Rev. **107**(10), 4022–4047 (2007). https://doi.org/10.1021/cr050193e
92. J. Ran, J. Zhang, J. Yu, M. Jaroniec, S.Z. Qiao, Earth-abundant cocatalysts for semiconductor-based photocatalytic water splitting. Chem. Soc. Rev. **43**(22), 7787–7812 (2014). https://doi.org/10.1039/c3cs60425j
93. A. Kudo, Y. Miseki, Heterogeneous photocatalyst materials for water splitting. Chem. Soc. Rev. **38**(1), 253–278 (2009). https://doi.org/10.1039/b800489g

 https://doi.org/10.1007/s40820-026-02111-0

94. D. Ma, J. Chen, J. Li, X. Ji, J.-W. Shi, A review on passivation engineering for improving photocatalytic hydrogen evolution performance. J. Mater. Chem. A **12**(21), 12293–12324 (2024). https://doi.org/10.1039/D4TA00411F
95. C. Bie, L. Wang, J. Yu, Challenges for photocatalytic overall water splitting. Chem **8**(6), 1567–1574 (2022). https://doi.org/10.1016/j.chempr.2022.04.013
96. C. Gao, J. Low, R. Long, T. Kong, J. Zhu et al., Heterogeneous single-atom photocatalysts: fundamentals and applications. Chem. Rev. **120**(21), 12175–12216 (2020). https://doi.org/10.1021/acs.chemrev.9b00840
97. Z. Xie, Q. Gao, X. Shang, X. Fu, J. Yang et al., Mini review on electron mediator in artificial photosynthesis: design, fabrication, and perspectives based on energy level matching. Green Carbon **2**(4), 366–382 (2024). https://doi.org/10.1016/j.greenca.2024.07.007
98. J. Gao, X. Qian, J. Wang, T. Hu, L. Kang et al., Ammonia-assisted photosynthesis of ethylene glycol. J. Am. Chem. Soc. **147**(46), 42777–42785 (2025). https://doi.org/10.1021/jacs.5c14704
99. S. Zhu, D. Wang, Photocatalysis: basic principles, diverse forms of implementations and emerging scientific opportunities. Adv. Energy Mater. **7**(23), 1700841 (2017). https://doi.org/10.1002/aenm.201700841
100. R. Asahi, T. Morikawa, T. Ohwaki, K. Aoki, Y. Taga, Visible-light photocatalysis in nitrogen-doped titanium oxides. Science **293**(5528), 269–271 (2001). https://doi.org/10.1126/science.1061051
101. H. Wang, L. Zhang, Z. Chen, J. Hu, S. Li et al., Semiconductor heterojunction photocatalysts: design, construction, and photocatalytic performances. Chem. Soc. Rev. **43**(15), 5234–5244 (2014). https://doi.org/10.1039/c4cs00126e
102. X. Yang, D. Wang, Photocatalysis: from fundamental principles to materials and applications. ACS Appl. Energy Mater. **1**(12), 6657–6693 (2018). https://doi.org/10.1021/acsaem.8b01345
103. X. Jing, N. Lu, S. Ben, S. Du, W. Lu et al., Single-atom-layer metallization of plasmonic semiconductors: modulating hot-electron kinetics for boosting photocatalysis. Chemsuschem **18**(19), e202501239 (2025). https://doi.org/10.1002/cssc.202501239
104. B. Zhang, D. Wang, J. Cao, W. He, G. Liu et al., Tuning Stark effect by defect engineering on black titanium dioxide mesoporous spheres for enhanced hydrogen evolution. Chin. Chem. Lett. **35**(11), 110254 (2024). https://doi.org/10.1016/j.cclet.2024.110254
105. X. Tao, Y. Zhao, S. Wang, C. Li, R. Li, Recent advances and perspectives for solar-driven water splitting using particulate photocatalysts. Chem. Soc. Rev. **51**(9), 3561–3608 (2022). https://doi.org/10.1039/D1CS01182K
106. H. Cai, F. Chen, C. Hu, W. Ge, T. Li et al., Oxygen vacancies mediated ultrathin $Bi_4O_5Br_2$ nanosheets for efficient piezocatalytic peroxide hydrogen generation in pure water. Chin. J. Catal. **57**, 123–132 (2024). https://doi.org/10.1016/S1872-2067(23)64591-7
107. Q. Zhu, Q. Xu, M. Du, X. Zeng, G. Zhong et al., Recent progress of metal sulfide photocatalysts for solar energy conversion. Adv. Mater. **34**(45), e2202929 (2022). https://doi.org/10.1002/adma.202202929
108. F. Huang, Z. Li, Y. Xu, A. Yan, T. Zhang et al., Excellent anti-photocorrosion and hydrogen evolution activity of $ZnIn_2S_4$-based photocatalysts: *in-situ* design of photogenerated charge dynamics. Chem. Eng. J. **473**, 145430 (2023). https://doi.org/10.1016/j.cej.2023.145430
109. D. Gao, J. Xu, L. Wang, B. Zhu, H. Yu et al., Optimizing atomic hydrogen desorption of sulfur-rich NiS_{1+x} cocatalyst for boosting photocatalytic H_2 evolution. Adv. Mater. **34**(6), 2108475 (2022). https://doi.org/10.1002/adma.202108475
110. C. Wu, W. Huang, H. Liu, K. Lv, Q. Li, Insight into synergistic effect of Ti_3C_2 MXene and MoS_2 on anti-photocorrosion and photocatalytic of CdS for hydrogen production. Appl. Catal. B Environ. **330**, 122653 (2023). https://doi.org/10.1016/j.apcatb.2023.122653
111. Y. Kuang, Q. Jia, G. Ma, T. Hisatomi, T. Minegishi et al., Ultrastable low-bias water splitting photoanodes *via* photocorrosion inhibition and *in situ* catalyst regeneration. Nat. Energy **2**, 16191 (2017). https://doi.org/10.1038/nenergy.2016.191
112. Z. Fan, X. Guo, F. Liu, Y. Li, L. Zhang et al., S-scheme heterojunction of polyfluorene derivatives coupled with $Zn_xCd_{1-x}S$ nanoparticles for efficient and stable photocatalytic hydrogen evolution. Appl. Mater. Today **29**, 101637 (2022). https://doi.org/10.1016/j.apmt.2022.101637
113. L. Lin, T. Hisatomi, S. Chen, T. Takata, K. Domen, Visible-light-driven photocatalytic water splitting: recent progress and challenges. Trends Chem. **2**(9), 813–824 (2020). https://doi.org/10.1016/j.trechm.2020.06.006
114. Q. Wang, M. Nakabayashi, T. Hisatomi, S. Sun, S. Akiyama et al., Oxysulfide photocatalyst for visible-light-driven overall water splitting. Nat. Mater. **18**(8), 827–832 (2019). https://doi.org/10.1038/s41563-019-0399-z
115. Z. Zhang, K. Chen, Q. Zhao, M. Huang, X. Ouyang, Electrocatalytic and photocatalytic performance of noble metal doped monolayer MoS_2 in the hydrogen evolution reaction: a first principles study. Nano Mater. Sci. **3**(1), 89–94 (2021). https://doi.org/10.1016/j.nanoms.2020.05.001
116. J. Gao, J. Wang, D. Li, G. Ran, W. Zhang et al., Artificial photosynthesis of formamide *via* an oxidant-free photoinduced radical coupling route over Pt-CdS. Angew. Chem. Int. Ed. **64**(19), e202500747 (2025). https://doi.org/10.1002/anie.202500747
117. G. Zhang, X. Wang, Oxysulfide semiconductors for photocatalytic overall water splitting with visible light. Angew. Chem. Int. Ed. **58**(44), 15580–15582 (2019). https://doi.org/10.1002/anie.201909669
118. M. Zhang, S. Nie, T. Cheng, Y. Feng, C. Zhang et al., Enhancing the macroscopic polarization of CdS for piezo-photocatalytic water splitting. Nano Energy **90**, 106635 (2021). https://doi.org/10.1016/j.nanoen.2021.106635
119. H. Wang, Y. Shi, J. Guo, S. Sun, W. Zhang et al., CdS clusters induced defect on NH_2−MIL-125(Ti) nanosheets for

improving photocatalytic synthesis of N-benzylidene benzylamine. Chin. Chem. Lett. **36**(10), 110779 (2025). https://doi.org/10.1016/j.cclet.2024.110779

120. L. Zheng, F. Teng, X. Ye, H. Zheng, X. Fang, Photo/electrochemical applications of metal sulfide/TiO_2 heterostructures. Adv. Energy Mater. **10**(1), 1902355 (2020). https://doi.org/10.1002/aenm.201902355
121. X. Jia, Y. Lu, K. Du, H. Zheng, L. Mao et al., Interfacial mediation by Sn and S vacancies of *p*-SnS/*n*-$ZnIn_2S_4$ for enhancing photocatalytic hydrogen evolution with new scheme of type-I heterojunction. Adv. Funct. Mater. **33**(50), 2304072 (2023). https://doi.org/10.1002/adfm.202304072
122. C. Wang, Y. Tang, Z. Geng, Y. Guo, X. Tan et al., Modulating charge accumulation *via* electron interaction for photocatalytic hydrogen evolution: a case of fabricating palladium sites on $ZnIn_2S_4$ nanosheets. ACS Catal. **13**(17), 11687–11696 (2023). https://doi.org/10.1021/acscatal.3c02563
123. X. Feng, H. Shang, J. Zhou, X. Ma, X. Gao et al., Heterostructured core–shell $CoS_{1.097}$@$ZnIn_2S_4$ nanosheets for enhanced photocatalytic hydrogen evolution under visible light. Chem. Eng. J. **457**, 141192 (2023). https://doi.org/10.1016/j.cej.2022.141192
124. J. Radhakrishnan, A. Kareem, S. Ratna, S. Senthilkumar, K. Biswas, Snowflake-like metastable wurtzite $CuGaS_2$/MoS_2 composite with superior electrochemical HER activity. ACS Omega **7**(48), 43883–43893 (2022). https://doi.org/10.1021/acsomega.2c05116
125. M. Zhou, Y. Wang, Highly efficient degradation of tetracycline hydrochloride using monodisperse $CuGaS_2$ quantum dots under UV-LED. J. Phys. Chem. C **129**(9), 4407–4414 (2025). https://doi.org/10.1021/acs.jpcc.4c07930
126. Z. Guan, Z. Xu, Q. Li, P. Wang, G. Li et al., $AgIn_5S_8$ nanoparticles anchored on 2D layered $ZnIn_2S_4$ to form 0D/2D heterojunction for enhanced visible-light photocatalytic hydrogen evolution. Appl. Catal. B Environ. **227**, 512–518 (2018). https://doi.org/10.1016/j.apcatb.2018.01.068
127. A. Jiang, H. Guo, S. Yu, F. Zhang, T. Shuai et al., Dual charge-accepting engineering modified $AgIn_5S_8$/CdS quantum dots for efficient photocatalytic hydrogen evolution overall H_2S splitting. Appl. Catal. B Environ. **332**, 122747 (2023). https://doi.org/10.1016/j.apcatb.2023.122747
128. X. Shi, C. Dai, X. Wang, J. Hu, J. Zhang et al., Protruding Pt single-sites on hexagonal $ZnIn_2S_4$ to accelerate photocatalytic hydrogen evolution. Nat. Commun. **13**(1), 1287 (2022). https://doi.org/10.1038/s41467-022-28995-1
129. Y. Liu, Q. Zeng, Y. Wei, R. Gao, D. Zeng, Boosting photocatalytic H_2 generation *via* interfacial charge transfer in $CuInS_2$ nanoflower-decorated CdS nanosheets. Int. J. Hydrog. Energy **138**, 286–295 (2025). https://doi.org/10.1016/j.ijhydene.2025.05.180
130. Y. Liu, X. Zheng, Y. Yang, J. Li, W. Liu et al., Photocatalytic hydrogen evolution using ternary-metal-sulfide/TiO_2 heterojunction photocatalysts. ChemCatChem **14**(5), e202101439 (2022). https://doi.org/10.1002/cctc.202101439
131. D. Zhou, X. Xue, X. Wang, Q. Luan, A. Li et al., Ni, in Co-doped $ZnIn_2S_4$ for efficient hydrogen evolution: modulating charge flow and balancing H adsorption/desorption. Appl. Catal. B Environ. **310**, 121337 (2022). https://doi.org/10.1016/j.apcatb.2022.121337
132. T. Su, C. Men, L. Chen, B. Chu, X. Luo et al., Sulfur vacancy and $Ti_3C_2T_x$ cocatalyst synergistically boosting interfacial charge transfer in 2D/2D $Ti_3C_2T_x$/$ZnIn_2S_4$ heterostructure for enhanced photocatalytic hydrogen evolution. Adv. Sci. **9**(4), 2103715 (2022). https://doi.org/10.1002/advs.202103715
133. J. Luo, Z. Lin, Y. Zhao, S. Jiang, S. Song, The embedded $CuInS_2$ into hollow-concave carbon nitride for photocatalytic H_2O splitting into H_2 with S-scheme principle. Chin. J. Catal. **41**(1), 122–130 (2020). https://doi.org/10.1016/S1872-2067(19)63490-X
134. R. Janani, R. Preethi V, S. Singh, A. Rani, C.-T. Chang, Hierarchical ternary sulfides as effective photocatalyst for hydrogen generation through water splitting: a review on the performance of $ZnIn_2S_4$. Catalysts **11**(2), 277 (2021). https://doi.org/10.3390/catal11020277
135. T. Zhang, T. Wang, F. Meng, M. Yang, S. Kawi, Recent advances in $ZnIn_2S_4$-based materials towards photocatalytic purification, solar fuel production and organic transformations. J. Mater. Chem. C **10**(14), 5400–5424 (2022). https://doi.org/10.1039/D2TC00432A
136. Y. Kumar, R. Kumar, P. Raizada, A.A.P. Khan, Q. Van Le et al., Novel Z-scheme $ZnIn_2S_4$-based photocatalysts for solar-driven environmental and energy applications: progress and perspectives. J. Mater. Sci. Technol. **87**, 234–257 (2021). https://doi.org/10.1016/j.jmst.2021.01.051
137. G. Zhang, H. Wu, D. Chen, N. Li, Q. Xu et al., A mini-review on $ZnIn_2S_4$-based photocatalysts for energy and environmental application. Green Energy Environ. **7**(2), 176–204 (2022). https://doi.org/10.1016/j.gee.2020.12.015
138. X. Zheng, Z. Shao, J. Lin, Q. Gao, Z. Ma et al., Recent advances of $CuSbS_2$ and $CuPbSbS_3$ as photocatalyst in the application of photocatalytic hydrogen evolution and degradation. Chin. Chem. Lett. **36**(3), 110533 (2025). https://doi.org/10.1016/j.cclet.2024.110533
139. A. Sarilmaz, E. Genc, E. Aslan, A. Ozen, G. Yanalak et al., Photocatalytic hydrogen evolution *via* solar-driven water splitting by $CuSbS_2$ with different shapes. J. Photochem. Photobiol. A Chem. **400**, 112706 (2020). https://doi.org/10.1016/j.jphotochem.2020.112706
140. W. Wang, G. Zhi, J. Liu, L. Hao, L. Yang et al., Effect of PVP content on photocatalytic properties of $CuSbS_2$ particles with chemical etching. J. Nanopart. Res. **22**(9), 294 (2020). https://doi.org/10.1007/s11051-020-05024-0
141. W. Wang, Q. Sheng, G. Zhi, Y. Zhao, R. Qu et al., A strategy of adjusting band alignment to improve photocatalytic degradation and photocatalytic hydrogen evolution of $CuSbS_2$. Appl. Surf. Sci. **639**, 158251 (2023). https://doi.org/10.1016/j.apsusc.2023.158251
142. G. Zhi, L. Hao, W. Chen, Q. Sheng, L. Liu et al., Z-scheme $CuSbS_2$/ZnO heterojunction for enhanced photocatalytic

 https://doi.org/10.1007/s40820-026-02111-0

degradation of RhB. ChemistrySelect **7**(29), e202202457 (2022). https://doi.org/10.1002/slct.202202457

143. O.C. Olatunde, D.C. Onwudiwe, Evaluation of the photocatalytic and persulfate activation properties of GO-$CuSbS_2$ composite. J. Photochem. Photobiol. B, Biol. **9**, 100095 (2022). https://doi.org/10.1016/j.jpap.2021.100095
144. R. Zhang, R. Liu, Z. Ding, J. Ma, T. Wang et al., Phototh ermal-assisted S-scheme heterojunction of Cu_3SnS_4/$Mn_{0.3}Cd_{0.7}S$ for enhanced photocatalytic hydrogen production. J. Colloid Interface Sci. **682**, 568–577 (2025). https://doi.org/10.1016/j.jcis.2024.11.245
145. H. Li, S. Tao, S. Wan, G. Qiu, Q. Long et al., S-scheme heterojunction of ZnCdS nanospheres and dibenzothiophene modified graphite carbon nitride for enhanced H_2 production. Chin. J. Catal. **46**, 167–176 (2023). https://doi.org/10.1016/S1872-2067(22)64201-3
146. D. Gao, H. Long, X. Wang, J. Yu, H. Yu, Tailoring antibonding-orbital occupancy state of selenium in Se-enriched $ReSe_{2+x}$ cocatalyst for exceptional H_2 evolution of TiO_2 photocatalyst. Adv. Funct. Mater. **33**(6), 2209994 (2023). https://doi.org/10.1002/adfm.202209994
147. Y. Chen, F. Su, H. Xie, R. Wang, C. Ding et al., One-step construction of S-scheme heterojunctions of N-doped MoS_2 and S-doped g-C_3N_4 for enhanced photocatalytic hydrogen evolution. Chem. Eng. J. **404**, 126498 (2021). https://doi.org/10.1016/j.cej.2020.126498
148. T. Zhang, S. Lu, Sacrificial agents for photocatalytic hydrogen production: effects, cost, and development. Chem. Catalysis **2**(7), 1502–1505 (2022). https://doi.org/10.1016/j.checat.2022.06.023
149. X. Liu, Y. Zhang, C. Wang, L. Shen, Polar materials for photocatalytic applications: a critical review. Interdiscip. Mater. **3**(4), 530–564 (2024). https://doi.org/10.1002/idm2.12176
150. Y. Zhao, S. Zhang, R. Shi, G.I.N. Waterhouse, J. Tang et al., Two-dimensional photocatalyst design: a critical review of recent experimental and computational advances. Mater. Today **34**, 78–91 (2020). https://doi.org/10.1016/j.mattod.2019.10.022
151. J. Zhang, R. Balasubramanian, X. Yang, Novel 3D multilayered carbon nitride/indium sulfide heterostructure for boosted superoxide anion radical generation and enhanced photocatalysis under visible light. Chem. Eng. J. **453**, 139776 (2023). https://doi.org/10.1016/j.cej.2022.139776
152. J. Ran, W. Guo, H. Wang, B. Zhu, J. Yu et al., Metal-free 2D/2D phosphorene/g-C_3N_4 van der Waals heterojunction for highly enhanced visible-light photocatalytic H_2 production. Adv. Mater. **30**(25), 1800128 (2018). https://doi.org/10.1002/adma.201800128
153. H. An, M. Li, W. Wang, Z. Lv, C. Deng et al., Construction of ternary rGO/1D TiO_2 nanotubes/3D $ZnIn_2S_4$ microsphere heterostructure and mutually-reinforcing synergy for high-efficiency H_2 production photoactivity under visible light. Ceram. Int. **45**(12), 14976–14982 (2019). https://doi.org/10.1016/j.ceramint.2019.04.234
154. K. Khan, A.K. Tareen, M. Aslam, R.U.R. Sagar, B. Zhang et al., Recent progress, challenges, and prospects in two-dimensional photo-catalyst materials and environmental remediation. Nano-Micro Lett. **12**(1), 167 (2020). https://doi.org/10.1007/s40820-020-00504-3
155. X. Zhang, H. Su, P. Cui, Y. Cao, Z. Teng et al., Developing Ni single-atom sites in carbon nitride for efficient photocatalytic H_2O_2 production. Nat. Commun. **14**(1), 7115 (2023). https://doi.org/10.1038/s41467-023-42887-y
156. V.N. Rao, C.W. Ahn, Y. Lee, M.V. Shankar, H. Kwon et al., Insights into excitons manipulation in metal chalcogenides based Nano-heterojunction Photocatalysts: a breakthrough in green hydrogen production. Coord. Chem. Rev. **522**, 216176 (2025). https://doi.org/10.1016/j.ccr.2024.216176
157. Y. Xiong, Z. Yi, W. Zhang, Y. Huang, Z. Zhang et al., Recent advances in perovskite/Cu(In, Ga)Se_2 tandem solar cells. Mater. Today Electron. **7**, 100086 (2024). https://doi.org/10.1016/j.mtelec.2023.100086
158. Y. Wu, M. Wei, Y. Sun, X. Yang, W. Xun et al., A buried interface modification strategy for enhancing the photovoltaic performance of NiO_x-based inverted perovskite solar cells. Vacuum **222**, 113057 (2024). https://doi.org/10.1016/j.vacuum.2024.113057
159. W. Liu, P. Shi, X. Tian, X. He, L. Li, Facile recycling of porous Si waste for stable Si/C anodes. Electrochim. Acta **507**, 145163 (2024). https://doi.org/10.1016/j.electacta.2024.145163
160. Y. Zhou, H. Zhang, Y. Xian, Z. Shi, J.N. Aboa et al., Enhancing charge-emitting shallow traps in metal halide perovskites by >100 times by surface strain. Joule **9**(1), 101772 (2025). https://doi.org/10.1016/j.joule.2024.10.004
161. C. Zhu, X. Wang, H. Li, C. Wang, Z. Gao et al., Stress compensation based on interfacial nanostructures for stable perovskite solar cells. Interdiscip. Mater. **2**(2), 348–359 (2023). https://doi.org/10.1002/idm2.12079
162. X. Yu, B. Cai, J. Zhang, X. Li, X. Wang et al., Fullerene modification of WO_3 electron transport layer toward high-efficiency MA-free perovskite solar cells with eliminated light-soaking effect. Interdiscip. Mater. **2**(3), 459–469 (2023). https://doi.org/10.1002/idm2.12089
163. Y. Xiao, D.G. Bradley, W.X. Chan, X. Hu, L. Xiao et al., Optical time-lapsed *in situ* mechanochemical studies on metal halide perovskite systems. Nat. Commun. **16**(1), 1362 (2025). https://doi.org/10.1038/s41467-025-56571-w
164. L. Brus, Size, dimensionality, and strong electron correlation in nanoscience. Acc. Chem. Res. **47**(10), 2951–2959 (2014). https://doi.org/10.1021/ar500175h
165. H. Seo, C. Hotta, H. Fukuyama, Toward systematic understanding of diversity of electronic properties in low-dimensional molecular solids. Chem. Rev. **104**(11), 5005–5036 (2004). https://doi.org/10.1021/cr030646k
166. P.J. Skabara, J.-B. Arlin, Y.H. Geerts, Close encounters of the 3D kind–exploiting high dimensionality in molecular semiconductors. Adv. Mater. **25**(13), 1948–1954 (2013). https://doi.org/10.1002/adma.201200862
167. S. Duan, Y. Cheng, W. Xia, Y. Yang, C. Xu et al., Optical manipulation of electronic dimensionality in a quantum

material. Nature **595**(7866), 239–244 (2021). https://doi.org/10.1038/s41586-021-03643-8

168. Y.-R. Liu, M. Zhang, Y.-H. Yu, Y.-L. Liu, J. Li et al., Local electric fields coupled with Cl^- fixation strategy for improving seawater oxygen reduction reaction performance. J. Electrochem. **31**(9), 2504132 (2025). https://doi.org/10.61558/2993-074x.3566
169. L. Wang, W. Zhang, X. Zheng, Y. Chen, W. Wu et al., Incorporating nitrogen atoms into cobalt nanosheets as a strategy to boost catalytic activity toward CO_2 hydrogenation. Nat. Energy **2**(11), 869–876 (2017). https://doi.org/10.1038/s41560-017-0015-x
170. C.-H. Ri, H.-U. Han, Y.-S. Kim, U.-G. Jong, Y.-H. Kye et al., Enhancing the photocatalytic hydrogen evolution performance of the $CsPbI_3/MoS_2$ heterostructure with interfacial defect engineering. J. Phys. Chem. Lett. **13**(18), 4007–4014 (2022). https://doi.org/10.1021/acs.jpclett.2c00851
171. G. Chen, P. Wang, Y. Wu, Q. Zhang, Q. Wu et al., Lead-free halide perovskite $Cs_3Bi_{2x}Sb_{2-2x}I_9$ ($x \approx 0.3$) possessing the photocatalytic activity for hydrogen evolution comparable to that of $(CH_3NH_3)PbI_3$. Adv. Mater. **32**(39), e2001344 (2020). https://doi.org/10.1002/adma.202001344
172. S. Feng, S. Ning, L. Wang, J. Zhao, J. Ou et al., Modifying $CsPbX_3$ (X = Cl, Br, I) with a zeolitic imidazolate framework through mechanical milling for aqueous photocatalytic H_2 evolution. ACS Appl. Energy Mater. **5**(5), 6248–6255 (2022). https://doi.org/10.1021/acsaem.2c00615
173. C.-H. Ri, S.-H. Pak, S.-I. O., C.-S. Jang, Y.-S. Kim et al., A first-principles study of interfacial vacancies in the β-$CsPbI_3$/1T-MoS_2 heterostructure towards photocatalytic applications. Phys. Chem. Chem. Phys. **27**(11), 5555–5565 (2025). https://doi.org/10.1039/D5CP00048C
174. D. Liu, N.P. Holzapfel, A. Milder, P.M. Woodward, Exploring the electronic dimensionality of ternary and quaternary rhodium halides. Chem. Mater. **36**(5), 2450–2460 (2024). https://doi.org/10.1021/acs.chemmater.3c03208
175. S.A. Novikov, H.A. Long, A.D. Valueva, V.V. Klepov, Application of voronoi polyhedra for analysis of electronic dimensionality in emissive halide materials. J. Am. Chem. Soc. **146**(51), 35449–35461 (2024). https://doi.org/10.1021/jacs.4c14554
176. V.R. Vadagavi, R.I. Jafri, K.S.R. Menon, S. Mandal, Tuning the electronic dimensionality and bandgap in Cs_2AgBiX_6 (X = Br, Cl) for photovoltaic applications: a DFT-1/2 study of cation disorder. Phys. Chem. Chem. Phys. **26**(47), 29595–29603 (2024). https://doi.org/10.1039/D4CP03808H
177. A. Shabaev, M.J. Mehl, A.L. Efros, Energy band structure of $CuInS_2$ and optical spectra of $CuInS_2$ nanocrystals. Phys. Rev. B **92**(3), 035431 (2015). https://doi.org/10.1103/physrevb.92.035431
178. R. Wu, Y. Liu, S. Hu, P. Fu, Z. Xiao, Red-emitting perovskite variant Cs_2PtCl_6 phosphor: material design, luminous mechanism, and application in high-color-rendering white light-emitting diodes. Adv. Opt. Mater. **10**(21), 2201081 (2022). https://doi.org/10.1002/adom.202201081
179. X. Du, Y. Liu, W. Pan, J. Pang, J. Zhu et al., Chemical potential diagram guided rational tuning of electrical properties: a case study of $CsPbBr_3$ for X-ray detection. Adv. Mater. **34**(17), e2110252 (2022). https://doi.org/10.1002/adma.202110252
180. Y. Chu, Y. Hu, Z. Xiao, First-principles insights into the stability difference between ABX_3 halide perovskites and their A_2BX_6 variants. J. Phys. Chem. C **125**(18), 9688–9694 (2021). https://doi.org/10.1021/acs.jpcc.1c02312
181. Z. Xie, Y. Wu, M. Wei, Y. Zhao, Q.-S. Jiang et al., Improving the open-circuit voltage of low-dimensional perovskite solar cells with NiO_x films by interfacial energy level alignment. ChemistrySelect **8**(17), e202300082 (2023). https://doi.org/10.1002/slct.202300082
182. Q.-S. Jiang, Z. Xie, M. Wei, Y. Zhao, Y. Wu et al., Effective of *l*-tyrosine hydrochloride on the photovoltaic performance of tin-based perovskite solar cells by suppressing tin (II) oxidation. Mater. Lett. **355**, 135485 (2024). https://doi.org/10.1016/j.matlet.2023.135485
183. Q. Sun, B. Ge, B. Xiao, F. Li, L. Ji et al., High-performance industrial-grade $CsPbBr_3$ single crystal by solid-liquid interface engineering. Adv. Sci. **10**(23), 2302236 (2023). https://doi.org/10.1002/advs.202302236
184. Y. Zhou, C. Fei, M.A. Uddin, L. Zhao, Z. Ni et al., Self-powered perovskite photon-counting detectors. Nature **616**(7958), 712–718 (2023). https://doi.org/10.1038/s41586-023-05847-6
185. Y.-P. Lin, B. Xia, S. Hu, Y. Zhong, Y.-E. Huang et al., Reversible release and fixation of bromine in vacancy-ordered bromide perovskites. Energy Environ. Mater. **3**(4), 535–540 (2020). https://doi.org/10.1002/eem2.12082
186. G. Xie, H. Li, L. Qiu, Recent advances on monolithic perovskite-organic tandem solar cells. Interdiscip. Mater. **3**(1), e12142 (2024). https://doi.org/10.1002/idm2.12142
187. Z. Xiao, Comment on "high-efficient blue emission and bandgap engineering from jahn−teller distorted halide double perovskites." Adv. Opt. Mater. **12**(32), 2302471 (2024). https://doi.org/10.1002/adom.202302471
188. S. Geng, Z. Xiao, Can nitride perovskites provide the same superior optoelectronic properties as lead halide perovskites? ACS Energy Lett. **8**(4), 2051–2057 (2023). https://doi.org/10.1021/acsenergylett.3c00658
189. Z. Xiao, Z. Song, Y. Yan, From lead halide perovskites to lead-free metal halide perovskites and perovskite derivatives. Adv. Mater. **31**(47), e1803792 (2019). https://doi.org/10.1002/adma.201803792
190. Y. Bai, D. Xing, H. Luo, Q.-S. Jiang, L. Yuan et al., Facilitating the formation of SnO_2 film *via* hydroxyl groups for efficient perovskite solar cells. Appl. Surf. Sci. **552**, 149459 (2021). https://doi.org/10.1016/j.apsusc.2021.149459
191. K.M. Koskela, B.C. Melot, R.L. Brutchey, Solution deposition of a bournonite $CuPbSbS_3$ semiconductor thin film from the dissolution of bulk materials with a thiol-amine solvent mixture. J. Am. Chem. Soc. **142**(13), 6173–6179 (2020). https://doi.org/10.1021/jacs.9b13787

 https://doi.org/10.1007/s40820-026-02111-0

192. A. Faghaninia, G. Yu, U. Aydemir, M. Wood, W. Chen et al., A computational assessment of the electronic, thermoelectric, and defect properties of bournonite ($CuPbSbS_3$) and related substitutions. Phys. Chem. Chem. Phys. **19**(9), 6743–6756 (2017). https://doi.org/10.1039/c7cp00437k
193. Y.T. Alharbi, F. Alam, K. Parvez, M. Missous, D.J. Lewis, Molecular precursor route to bournonite ($CuPbSbS_3$) thin films and powders. Inorg. Chem. **60**(17), 13691–13698 (2021). https://doi.org/10.1021/acs.inorgchem.1c02001
194. Y. Liu, B. Yang, M. Zhang, B. Xia, C. Chen et al., Bournonite $CuPbSbS_3$: an electronically-3D, defect-tolerant, and solution-processable semiconductor for efficient solar cells. Nano Energy **71**, 104574 (2020). https://doi.org/10.1016/j.nanoen.2020.104574
195. J.T.R. Dufton, A. Walsh, P.M. Panchmatia, L.M. Peter, D. Colombara et al., Structural and electronic properties of $CuSbS_2$ and $CuBiS_2$: potential absorber materials for thin-film solar cells. Phys. Chem. Chem. Phys. **14**(20), 7229–7233 (2012). https://doi.org/10.1039/C2CP40916J
196. A.B. Kehoe, D.J. Temple, G.W. Watson, D.O. Scanlon, Cu_3MCh_3 (M = Sb, Bi; Ch = S, Se) as candidate solar cell absorbers: insights from theory. Phys. Chem. Chem. Phys. **15**(37), 15477–15484 (2013). https://doi.org/10.1039/c3cp52482e
197. P.K. Sadanand, S. Singh, P. Rai, D.K. Lohia, Dwivedi, comparative study of the CZTS, $CuSbS_2$ and $CuSbSe_2$ solar photovoltaic cell with an earth-abundant non-toxic buffer layer. Sol. Energy **222**, 175–185 (2021). https://doi.org/10.1016/j.solener.2021.05.013
198. L. Fu, J. Yu, J. Wang, F. Xie, S. Yao et al., Thin film solar cells based on Ag-substituted $CuSbS_2$ absorber. Chem. Eng. J. **400**, 125906 (2020). https://doi.org/10.1016/j.cej.2020.125906
199. A. Walsh, D.J. Payne, R.G. Egdell, G.W. Watson, Stereochemistry of post-transition metal oxides: revision of the classical lone pair model. Chem. Soc. Rev. **40**(9), 4455–4463 (2011). https://doi.org/10.1039/c1cs15098g
200. B. Yang, L. Wang, J. Han, Y. Zhou, H. Song et al., $CuSbS_2$ as a promising earth-abundant photovoltaic absorber material: a combined theoretical and experimental study. Chem. Mater. **26**(10), 3135–3143 (2014). https://doi.org/10.1021/cm500516v
201. H. Zhang, Z. Wang, J. Zhang, K. Dai, Metal-sulfide-based heterojunction photocatalysts: principles, impact, applications, and *in-situ* characterization. Chin. J. Catal. **49**, 42–67 (2023). https://doi.org/10.1016/S1872-2067(23)64444-4
202. M.M. Ramin Moayed, T. Bielewicz, M.S. Zöllner, C. Herrmann, C. Klinke, Towards colloidal spintronics through Rashba spin-orbit interaction in lead sulphide nanosheets. Nat. Commun. **8**, 15721 (2017). https://doi.org/10.1038/ncomms15721
203. Z. Hu, R. O'Neill, R. Lesyuk, C. Klinke, Colloidal two-dimensional metal chalcogenides: realization and application of the structural anisotropy. Acc. Chem. Res. **54**(20), 3792–3803 (2021). https://doi.org/10.1021/acs.accounts.1c00209
204. S. Chen, D. Huang, P. Xu, W. Xue, L. Lei et al., Semiconductor-based photocatalysts for photocatalytic and photoelectrochemical water splitting: Will we stop with photocorrosion? J. Mater. Chem. A **8**(5), 2286–2322 (2020). https://doi.org/10.1039/C9TA12799B
205. K. Iwashina, A. Iwase, Y.H. Ng, R. Amal, A. Kudo, Z-schematic water splitting into H_2 and O_2 using metal sulfide as a hydrogen-evolving photocatalyst and reduced graphene oxide as a solid-state electron mediator. J. Am. Chem. Soc. **137**(2), 604–607 (2015). https://doi.org/10.1021/ja511615s
206. C. Li, H. Che, Y. Yan, C. Liu, H. Dong, Z-scheme $AgVO_3$/$ZnIn_2S_4$ photocatalysts: "one stone and two birds" strategy to solve photocorrosion and improve the photocatalytic activity and stability. Chem. Eng. J. **398**, 125523 (2020). https://doi.org/10.1016/j.cej.2020.125523
207. A. Iwase, S. Yoshino, T. Takayama, Y.H. Ng, R. Amal et al., Water splitting and CO_2 reduction under visible light irradiation using Z-scheme systems consisting of metal sulfides, CoO_x-loaded $BiVO_4$, and a reduced graphene oxide electron mediator. J. Am. Chem. Soc. **138**(32), 10260–10264 (2016). https://doi.org/10.1021/jacs.6b05304
208. Y. Zhang, Y. Wang, X. Wu, T. Li, F. Zhao et al., Photocorrosion of metal sulfides: mechanism, characterization, anti-photocorrosion strategies and solar catalysis applications. Coord. Chem. Rev. **545**, 217021 (2025). https://doi.org/10.1016/j.ccr.2025.217021
209. X. Wu, S. Xie, H. Zhang, Q. Zhang, B.F. Sels et al., Metal sulfide photocatalysts for lignocellulose valorization. Adv. Mater. **33**(50), e2007129 (2021). https://doi.org/10.1002/adma.202007129
210. X. Zheng, D. Wu, Y. Liu, J. Li, Y. Yang et al., Photocatalytic reduction of water to hydrogen by $CuPbSbS_3$ nanoflakes. Mater. Today Energy **25**, 100956 (2022). https://doi.org/10.1016/j.mtener.2022.100956
211. F. Chen, H. Huang, L. Guo, Y. Zhang, T. Ma, The role of polarization in photocatalysis. Angew. Chem. Int. Ed. **58**(30), 10061–10073 (2019). https://doi.org/10.1002/anie.201901361
212. C. Hu, H. Huang, Advances in piezoelectric polarization enhanced photocatalytic energy conversion. Acta Phys. Chim. Sin. (2023). https://doi.org/10.3866/pku.whxb202212048
213. Y. Liu, M. Zhang, Z. Wang, J. He, J. Zhang et al., Bipolar charge collecting structure enables overall water splitting on ferroelectric photocatalysts. Nat. Commun. **13**(1), 4245 (2022). https://doi.org/10.1038/s41467-022-32002-y
214. L.W. Martin, A.M. Rappe, Thin-film ferroelectric materials and their applications. Nat. Rev. Mater. **2**(2), 16087 (2017). https://doi.org/10.1038/natrevmats.2016.87
215. H. Hu, X. Li, K. Zhang, G. Yan, W. Kong et al., Dual modification of metal–organic frameworks for exceptional high piezo-photocatalytic hydrogen production. Adv. Mater. **37**(20), 2419023 (2025). https://doi.org/10.1002/adma.202419023

216. Z.L. Wang, J. Song, Piezoelectric nanogenerators based on zinc oxide nanowire arrays. Science **312**(5771), 242–246 (2006). https://doi.org/10.1126/science.1124005
217. C.R. Bowen, H.A. Kim, P.M. Weaver, S. Dunn, Piezoelectric and ferroelectric materials and structures for energy harvesting applications. Energy Environ. Sci. **7**(1), 25–44 (2014). https://doi.org/10.1039/c3ee42454e
218. G. Liu, L. Ma, L.-C. Yin, G. Wan, H. Zhu et al., Selective chemical epitaxial growth of TiO_2 islands on ferroelectric $PbTiO_3$ crystals to boost photocatalytic activity. Joule **2**(6), 1095–1107 (2018). https://doi.org/10.1016/j.joule.2018.03.006
219. S. Dutta, P. Buragohain, S. Glinsek, C. Richter, H. Aramberri et al., Piezoelectricity in *Hafnia*. Nat. Commun. **12**, 7301 (2021). https://doi.org/10.1038/s41467-021-27480-5
220. S. Assavachin, F.E. Osterloh, Ferroelectric polarization in $BaTiO_3$ nanocrystals controls photoelectrochemical water oxidation and photocatalytic hydrogen evolution. J. Am. Chem. Soc. **145**(34), 18825–18833 (2023). https://doi.org/10.1021/jacs.3c03762
221. B. Dai, G.M. Biesold, M. Zhang, H. Zou, Y. Ding et al., Piezo-phototronic effect on photocatalysis, solar cells, photodetectors and light-emitting diodes. Chem. Soc. Rev. **50**(24), 13646–13691 (2021). https://doi.org/10.1039/d1cs00506e
222. Q. Liu, D. Zhai, Z. Xiao, C. Tang, Q. Sun et al., Piezo-photoelectronic coupling effect of $BaTiO_3$@TiO_2 nanowires for highly concentrated dye degradation. Nano Energy **92**, 106702 (2022). https://doi.org/10.1016/j.nanoen.2021.106702
223. N. Ma, C. Lu, Y. Liu, T. Han, W. Dong et al., Direct Z-scheme heterostructure of vertically oriented SnS_2 nanosheet on $BiVO_4$ nanoflower for self-powered photodetectors and water splitting. Small **20**(3), e2304839 (2024). https://doi.org/10.1002/smll.202304839
224. X. Huang, R. Lei, J. Yuan, F. Gao, C. Jiang et al., Insight into the piezo-photo coupling effect of $PbTiO_3$/CdS composites for piezo-photocatalytic hydrogen production. Appl. Catal. B Environ. **282**, 119586 (2021). https://doi.org/10.1016/j.apcatb.2020.119586
225. N. Hoàng Ly, S.J. Son, H. Kamyab, Y. Vasseghian, S.-W. Joo, Dual-function piezo-photocatalytic systems for sustainable hydrogen evolution and environmental remediation. Adv. Sci. **12**(46), e13811 (2025). https://doi.org/10.1002/advs.202513811
226. R. Mohanty, S. Mansingh, K. Parida, K. Parida, Boosting sluggish photocatalytic hydrogen evolution through piezo-stimulated polarization: a critical review. Mater. Horiz. **9**(5), 1332–1355 (2022). https://doi.org/10.1039/D1MH01899J
227. S. Tu, Y. Guo, Y. Zhang, C. Hu, T. Zhang et al., Piezocatalysis and piezo-photocatalysis: catalysts classification and modification strategy, reaction mechanism, and practical application. Adv. Funct. Mater. **30**(48), 2005158 (2020). https://doi.org/10.1002/adfm.202005158
228. Z. Chen, G. Li, X. Zheng, Y. Liu, J. Dai et al., Facile synthesis of advanced $BaTiO_3$/$CuPbSbS_3$ heterostructure photocatalyst with enhanced piezo-photocatalytic degradation performance. Nano Energy **124**, 109463 (2024). https://doi.org/10.1016/j.nanoen.2024.109463
229. K. Sharma, A. Kumar, T. Ahamad, Q. Van Le, P. Raizada et al., Sulphur vacancy defects engineered metal sulfides for amended photo(electro)catalytic water splitting: a review. J. Mater. Sci. Technol. **152**, 50–64 (2023). https://doi.org/10.1016/j.jmst.2022.11.053
230. D. Ayodhya, G. Veerabhadram, A review on recent advances in photodegradation of dyes using doped and heterojunction based semiconductor metal sulfide nanostructures for environmental protection. Mater. Today Energy **9**, 83–113 (2018). https://doi.org/10.1016/j.mtener.2018.05.007
231. W. Hu, L. Xie, C. Gu, W. Zheng, Y. Tu et al., The nature of active sites of molybdenum sulfide-based catalysts for hydrogen evolution reaction. Coord. Chem. Rev. **506**, 215715 (2024). https://doi.org/10.1016/j.ccr.2024.215715
232. Q. Xu, L. Zhang, B. Cheng, J. Fan, J. Yu, S-scheme heterojunction photocatalyst. Chem **6**(7), 1543–1559 (2020). https://doi.org/10.1016/j.chempr.2020.06.010
233. X. Hao, Y. Wang, J. Zhou, Z. Cui, Y. Wang et al., Zinc vacancy-promoted photocatalytic activity and photostability of ZnS for efficient visible-light-driven hydrogen evolution. Appl. Catal. B Environ. **221**, 302–311 (2018). https://doi.org/10.1016/j.apcatb.2017.09.006
234. B. Xiao, T. Lv, J. Zhao, Q. Rong, H. Zhang et al., Synergistic effect of the surface vacancy defects for promoting photocatalytic stability and activity of ZnS nanoparticles. ACS Catal. **11**(21), 13255–13265 (2021). https://doi.org/10.1021/acscatal.1c03476
235. R. Shi, H.-F. Ye, F. Liang, Z. Wang, K. Li et al., Interstitial P-doped CdS with long-lived photogenerated electrons for photocatalytic water splitting without sacrificial agents. Adv. Mater. **30**(6), 1705941 (2018). https://doi.org/10.1002/adma.201705941
236. Y. Lei, Y. Zhang, Z. Li, S. Xu, J. Huang et al., Molybdenum sulfide cocatalyst activation upon photodeposition of cobalt for improved photocatalytic hydrogen production activity of ZnCdS. Chem. Eng. J. **425**, 131478 (2021). https://doi.org/10.1016/j.cej.2021.131478
237. Q. Liu, S. Wang, Q. Ren, T. Li, G. Tu et al., Stacking design in photocatalysis: synergizing cocatalyst roles and anti-corrosion functions of metallic MoS_2 and graphene for remarkable hydrogen evolution over CdS. J. Mater. Chem. A **9**(3), 1552–1562 (2021). https://doi.org/10.1039/D0TA10255E
238. G. Yang, H. Ding, D. Chen, J. Feng, Q. Hao et al., Construction of urchin-like $ZnIn_2S_4$-Au-TiO_2 heterostructure with enhanced activity for photocatalytic hydrogen evolution. Appl. Catal. B Environ. **234**, 260–267 (2018). https://doi.org/10.1016/j.apcatb.2018.04.038
239. Z. Liu, F. Jin, X. Li, P. Zhang, Z. Jin, Morphological effects of WO_3 in metal sulfide-based S-scheme heterojunctions for boosting photocatalytic hydrogen production. J. Mater. Sci. Technol. **188**, 131–143 (2024). https://doi.org/10.1016/j.jmst.2023.10.060
240. K. Liang, W. Guo, L. Li, H. Cai, H. Zhang et al., Defect-induced synthesis of nanoscale hierarchically porous

 https://doi.org/10.1007/s40820-026-02111-0

metal-organic frameworks with tunable porosity for enhanced volatile organic compound adsorption. Nano Mater. Sci. **6**(4), 467–474 (2024). https://doi.org/10.1016/j.nanoms.2023.10.001

241. R. Shi, Y. Zhao, G.I.N. Waterhouse, S. Zhang, T. Zhang, Defect engineering in photocatalytic nitrogen fixation. ACS Catal. **9**(11), 9739–9750 (2019). https://doi.org/10.1021/acscatal.9b03246
242. A. Kumar, V. Krishnan, Vacancy engineering in semiconductor photocatalysts: implications in hydrogen evolution and nitrogen fixation applications. Adv. Funct. Mater. **31**(28), 2009807 (2021). https://doi.org/10.1002/adfm.202009807
243. C. Duan, J. Liu, Z. Li, R. Shi, J. Zhao et al., Efficient photocatalytic propane direct dehydrogenation to propylene over PtO_2 clusters. Adv. Mater. **37**(8), e2411648 (2025). https://doi.org/10.1002/adma.202411648
244. Y. Wang, W. Yu, C. Wang, F. Chen, T. Ma et al., Defects in photoreduction reactions: fundamentals, classification, and catalytic energy conversion. eScience **4**(3), 100228 (2024). https://doi.org/10.1016/j.esci.2024.100228
245. J. Liu, D. Zhao, X. Wu, D. Wu, N. Su et al., Synergistic dual-defect band engineering for highly efficient photocatalytic degradation of microplastics *via* Nb-induced oxygen vacancies in SnO_2 quantum dots. J. Mater. Chem. A **13**(6), 4429–4443 (2025). https://doi.org/10.1039/d4ta07579j
246. J. Liu, Y. Yang, Z. Tang, Y. Chen, H. Chen et al., Catalytic hydrogenolysis of organosolv lignin: cleaving C-O bonds over $CuMgAlO_x$ -layered porous metal oxide catalysts for oriented monophenols production. Green Carbon **2**(2), 211–220 (2024). https://doi.org/10.1016/j.greenca.2024.04.001
247. F. Liu, Y. Hu, Z. Qu, X. Ma, Z. Li et al., Rapid production of kilogram-scale graphene nanoribbons with tunable interlayer spacing for an array of renewable energy. Proc. Natl. Acad. Sci. U.S.A. **120**(26), e2303262120 (2023). https://doi.org/10.1073/pnas.2303262120
248. S. Li, Z. Kan, H. Wang, J. Bai, Y. Liu et al., Single-atom photo-catalysts: synthesis, characterization, and applications. Nano Mater. Sci. **6**(3), 284–304 (2024). https://doi.org/10.1016/j.nanoms.2023.11.001
249. M. Abbas, M.A.Z.G. Sial, New horizon in stabilization of single atoms on metal-oxide supports for CO_2 reduction. Nano Mater. Sci. **3**(4), 368–389 (2021). https://doi.org/10.1016/j.nanoms.2021.07.009
250. J. Liu, X. Qu, C. Zhang, W. Dong, C. Fu et al., High-yield aqueous synthesis of partial-oxidized black phosphorus as layered nanodot photocatalysts for efficient visible-light driven degradation of emerging organic contaminants. J. Clean. Prod. **377**, 134228 (2022). https://doi.org/10.1016/j.jclepro.2022.134228
251. J. Zhang, D. Yan, G. Ding, X. Wang, C. Li et al., Dual co sites in n─n type heterojunction enable selective electrochemical co-valorization of HMF and CO_2. Angew. Chem. Int. Ed. **64**(37), e202511448 (2025). https://doi.org/10.1002/anie.202511448
252. F. Su, Z. Wang, H. Cao, H. Xie, W. Tu et al., Oxygen-deficient MoO_{3-x} evoked synergistic photo-thermal catalytic CO_2 reduction over g-C_3N_4. Catal. Sci. Technol. **13**(5), 1325–1334 (2023). https://doi.org/10.1039/d2cy01944b
253. H. Hong, H. Zhang, S. Lin, J.A. Dhas, B. Paudel et al., Metal-to-insulator transition in oxide semimetals by anion doping. Interdiscip. Mater. **3**(3), 358–368 (2024). https://doi.org/10.1002/idm2.12158
254. G. Wang, S. Zhong, X. Xiong, J. Li, F. Wang et al., Plasma induced grain boundaries to boost electrochemical reduction of CO_2 to formate. J. Energy Chem. **95**, 636–643 (2024). https://doi.org/10.1016/j.jechem.2024.04.026
255. H. Huang, B. Dai, W. Wang, C. Lu, J. Kou et al., Oriented built-in electric field introduced by surface gradient diffusion doping for enhanced photocatalytic H_2 evolution in CdS nanorods. Nano Lett. **17**(6), 3803–3808 (2017). https://doi.org/10.1021/acs.nanolett.7b01147
256. Q. Zeng, Y. Bao, S. Ning, Q. Yu, Y. Wei et al., Plasmonic Cu–Ni bimetal nanoparticles coupled with ultrathin CdS nanosheets for remarkably improved photocatalytic H_2 generation under visible-light irradiation. J. Mater. Chem. A **12**(28), 17286–17294 (2024). https://doi.org/10.1039/D4TA02353F
257. Y. Chen, K. Chen, J. Fu, A. Yamaguchi, H. Li et al., Recent advances in the utilization of copper sulfide compounds for electrochemical CO_2 reduction. Nano Mater. Sci. **2**(3), 235–247 (2020). https://doi.org/10.1016/j.nanoms.2019.10.006
258. Y. Song, W. Xie, M. Shao, X. Duan, Integrated electrocatalysts derived from metal organic frameworks for gas-involved reactions. Nano Mater. Sci. **5**(2), 161–176 (2023). https://doi.org/10.1016/j.nanoms.2022.01.003
259. G. Yu, Q. Zhang, M. Wang, H. Lu, Z. Chen et al., Osmotic energy directly driving flexible all-solid-state 2D nanofluidic pressure sensors. Adv. Mater. **37**(47), e06990 (2025). https://doi.org/10.1002/adma.202506990
260. S.-H. Li, M.-Y. Qi, Z.-R. Tang, Y.-J. Xu, Nanostructured metal phosphides: from controllable synthesis to sustainable catalysis. Chem. Soc. Rev. **50**(13), 7539–7586 (2021). https://doi.org/10.1039/d1cs00323b
261. C. Yang, Y. Xiang, W. Wang, B. Cheng, K. Yang et al., Enhancing photocatalytic H_2O_2 production of donor−acceptor polymers by modulation of polymerization modes. Appl. Catal. B Environ. Energy **365**, 124856 (2025). https://doi.org/10.1016/j.apcatb.2024.124856
262. H. Long, X. Zhang, Z. Zhang, J. Zhang, J. Yu et al., Fine-tuning d-p hybridization in Ni- B_x cocatalyst for enhanced photocatalytic H_2 production. Nat. Commun. **16**(1), 946 (2025). https://doi.org/10.1038/s41467-025-56306-x
263. Y. Xiao, G. Ding, J. Tao, Z. Wang, Z. Chen et al., Selective conversion of CO_2 to C_2H_6 in pure water photocatalyzed by fluorobenzene-linked perylene diimide. Nat. Commun. **16**(1), 7476 (2025). https://doi.org/10.1038/s41467-025-62369-7
264. Z. Kong, Z. Kong, D. Zhang, J. Liu, X.-Y. Ji et al., Magnetic separable non-precious metal Schottky heterojunction photocatalyst toward photothermal-assisted photocatalytic hydrogen evolution. Sep. Purif. Technol. **361**, 131429 (2025). https://doi.org/10.1016/j.seppur.2025.131429

265. Y. Yu, G. Li, Y. Xiao, C. Chen, Y. Bai et al., Iridium-based electrocatalysts for acidic oxygen evolution reaction. J. Energy Chem. **103**, 200–224 (2025). https://doi.org/10.1016/j.jechem.2024.11.033
266. T. Zhou, X. Li, J. Zhao, L. Luo, Y. Wang et al., Ultrafine metal nanoparticles isolated on oxide nano-islands as exceptional sintering-resistant catalysts. Nat. Mater. **24**(6), 891–899 (2025). https://doi.org/10.1038/s41563-025-02134-9
267. Y. Zhou, L. Zhao, Z. Ni, S. Xu, J. Zhao et al., Heterojunction structures for reduced noise in large-area and sensitive perovskite X-ray detectors. Sci. Adv. **7**(36), eabg6716 (2021). https://doi.org/10.1126/sciadv.abg6716
268. L. Zhang, Q. Zeng, Y. Liu, Z. Wang, Y. Wei et al., Significant enhancement of photocatalytic H_2 evolution and tetracycline degradation by CdO nanosheets-modified UiO-66-NH_2 nanoparticles. Chem. Eng. J. **500**, 157173 (2024). https://doi.org/10.1016/j.cej.2024.157173
269. J. Low, J. Yu, M. Jaroniec, S. Wageh, A.A. Al-Ghamdi, Heterojunction photocatalysts. Adv. Mater. **29**(20), 1601694 (2017). https://doi.org/10.1002/adma.201601694
270. Q. Chen, S. Ning, J. Yang, L. Wang, X. Yin et al., *In situ* interfacial engineering of CeO_2/Bi_2WO_6 heterojunction with improved photodegradation of tetracycline and organic dyes: mechanism insight and toxicity assessment. Small **20**(18), 2307304 (2024). https://doi.org/10.1002/smll.202307304
271. X. Yin, D. Gao, J. Zhang, H. García, J. Yu et al., Plasmon-induced ultrafast interfacial charge transfer for enhanced photocatalytic hydrogen evolution. J. Am. Chem. Soc. **147**(38), 34881–34890 (2025). https://doi.org/10.1021/jacs.5c11154
272. X. Wang, T. Shi, J. Cui, G. Li, L. Wang et al., Artificially regulating the crystallinity for constructing poly(heptazine imide)-based S-scheme homojunction with boosted photocatalytic hydrogen evolution performance. J. Mater. Sci. Technol. **196**, 262–272 (2024). https://doi.org/10.1016/j.jmst.2024.02.024
273. X.-Q. Wan, C.-L. Yang, W.-J. Shi, X. Li, Y. Liu et al., Efficient Z-scheme photocatalyst for hydrogen production *via* water splitting using CH_3- and F-modified C_{60} fullerene-based heterostructures. Small (2025). https://doi.org/10.1002/smll.202504146
274. T. Di, Q. Xu, W. Ho, H. Tang, Q. Xiang et al., Review on metal sulphide-based Z-scheme photocatalysts. ChemCatChem **11**(5), 1394–1411 (2019). https://doi.org/10.1002/cctc.201802024
275. Y. Bao, Q. Zeng, S. Ning, W. Zhao, L. Wang et al., Interfacial engineering of 0D/2D $CoMn_2O_4$ nanoparticles/CdS nanosheets p-n heterostructures for boosted photocatalytic H_2 production and U(VI) reduction. Int. J. Hydrog. Energy **68**, 586–595 (2024). https://doi.org/10.1016/j.ijhydene.2024.04.285
276. S. Chen, C. Li, K. Domen, F. Zhang, Particulate metal chalcogenides for photocatalytic Z-scheme overall water splitting. Joule **7**(11), 2445–2467 (2023). https://doi.org/10.1016/j.joule.2023.10.004
277. S. Wan, W. Wang, B. Cheng, G. Luo, Q. Shen et al., A superlattice interface and S-scheme heterojunction for ultrafast charge separation and transfer in photocatalytic H_2 evolution. Nat. Commun. **15**(1), 9612 (2024). https://doi.org/10.1038/s41467-024-53951-6
278. M. Tian, F. Su, Z. Wang, Y. Xiao, Y. Zhang et al., Constructing a stable CdS/Nb_2O_5 Z-scheme heterojunction for efficient photocatalytic conversion of CO_2. Mol. Catal. **576**, 114930 (2025). https://doi.org/10.1016/j.mcat.2025.114930
279. Y. Zhu, J. Ren, G. Huang, C.-L. Dong, Y.-C. Huang et al., Red phosphorus grafted high-index (116) faceted anatase TiO_2 for Z-scheme photocatalytic pure water splitting. Adv. Funct. Mater. **34**(9), 2311623 (2024). https://doi.org/10.1002/adfm.202311623
280. X.-Q. Wan, C.-L. Yang, X.-H. Li, M.-S. Wang, X.-G. Ma, Insights into photogenerated carrier dynamics and overall water splitting of the CrS_3/GeSe heterostructure. J. Phys. Chem. Lett. **14**(40), 9126–9135 (2023). https://doi.org/10.1021/acs.jpclett.3c01780
281. X. Wang, J. Li, W. Liu, S. Yang, C. Zhu et al., A fast chemical approach towards Sb_2S_3 film with a large grain size for high-performance planar heterojunction solar cells. Nanoscale **9**(10), 3386–3390 (2017). https://doi.org/10.1039/C7NR00154A
282. C. Wu, L. Zhang, H. Ding, H. Ju, X. Jin et al., Direct solution deposition of device quality $Sb_2S_{3-x}Se_x$ films for high efficiency solar cells. Sol. Energy Mater. Sol. Cells **183**, 52–58 (2018). https://doi.org/10.1016/j.solmat.2018.04.009
283. G. Wang, W. Zhao, Y. Cui, Q. Tian, S. Gao et al., Fabrication of a $Cu_2ZnSn(S, Se)_4$ photovoltaic device by a low-toxicity ethanol solution process. ACS Appl. Mater. Interfaces **5**(20), 10042–10047 (2013). https://doi.org/10.1021/am402558a
284. H. Guo, Y. Cui, Q. Tian, S. Gao, G. Wang et al., Significantly enhancing grain growth in $Cu_2ZnSn(S, Se)_4$ absorber layers by insetting Sb_2S_3, $CuSbS_2$, and $NaSb_5S_8$ thin films. Cryst. Growth Des. **15**(2), 771–777 (2015). https://doi.org/10.1021/cg501589t
285. Y. Xu, Q. Ye, W. Chen, X. Pan, L. Hu et al., Solution-processed $CuSbS_2$ solar cells based on metal–organic molecular solution precursors. J. Mater. Sci. **53**(3), 2016–2025 (2018). https://doi.org/10.1007/s10853-017-1663-8
286. X. Wang, R. Tang, C. Wu, C. Zhu, T. Chen, Development of antimony sulfide–selenide $Sb_2(S, Se)_3$-based solar cells. J. Energy Chem. **27**(3), 713–721 (2018). https://doi.org/10.1016/j.jechem.2017.09.031
287. G. Wang, S. Wang, Y. Cui, D. Pan, A novel and versatile strategy to prepare metal–organic molecular precursor solutions and its application in Cu(In, Ga)$(S, Se)_2$ solar cells. Chem. Mater. **24**(20), 3993–3997 (2012). https://doi.org/10.1021/cm3027303
288. Y. Liu, C. Chen, Y. Zhou, R. Kondrotas, J. Tang, Butyldithiocarbamate acid solution processing: its fundamentals and applications in chalcogenide thin film solar cells. J. Mater. Chem. C **7**(36), 11068–11084 (2019). https://doi.org/10.1039/c9tc02837d
289. L. Cheng, Q. Xiang, Y. Liao, H. Zhang, CdS-based photocatalysts. Energy Environ. Sci. **11**(6), 1362–1391 (2018). https://doi.org/10.1039/c7ee03640j

 https://doi.org/10.1007/s40820-026-02111-0

290. Z. Xu, W. Yue, C. Li, L. Wang, Y. Xu et al., Rational synthesis of Au-CdS composite photocatalysts for broad-spectrum photocatalytic hydrogen evolution. ACS Nano **17**(12), 11655–11664 (2023). https://doi.org/10.1021/acsnano.3c02092
291. Z. Fan, Q. Xu, Y. Wang, Y. Cao, X. Zeng et al., Electron regulation accelerates photocatalytic hydrogen evolution for bimetallic Pt, Au on CdS nanorods. Chem. Eng. J. **511**, 162016 (2025). https://doi.org/10.1016/j.cej.2025.162016
292. M. Ding, S. Cui, Z. Lin, X. Yang, Crystal facet engineering of hollow cadmium sulfide for efficient photocatalytic hydrogen evolution. Appl. Catal. B Environ. Energy **357**, 124333 (2024). https://doi.org/10.1016/j.apcatb.2024.124333
293. T. Huang, Z. Huang, X. Yang, S. Yang, Q. Gao et al., Green and regulable synthesis of CdNCN on CdS semiconductor: atomic-level heterostructures for enhanced photocatalytic hydrogen evolution. Adv. Powder Mater. **3**(6), 100242 (2024). https://doi.org/10.1016/j.apmate.2024.100242
294. W. Wu, N. Zhang, Y. Wang, Construction of Au/$ZnWO_4$/CdS ternary photocatalysts with oxygen vacancy modification for efficient photocatalytic hydrogen production. Adv. Funct. Mater. **34**(32), 2316604 (2024). https://doi.org/10.1002/adfm.202316604
295. R. Shen, D. Ren, Y. Ding, Y. Guan, Y.H. Ng et al., Nanostructured CdS for efficient photocatalytic H_2 evolution: a review. Sci. China Mater. **63**(11), 2153–2188 (2020). https://doi.org/10.1007/s40843-020-1456-x
296. X. Zheng, Y. Liu, Y. Yang, Y. Song, P. Deng et al., Recent advances in cadmium sulfide-based photocatalysts for photocatalytic hydrogen evolution. Renewables **1**(1), 39–56 (2023). https://doi.org/10.31635/renewables.022.202200001
297. Y. Wei, H. Qin, J. Deng, X. Cheng, M. Cai et al., Semiconductor photocatalysts for solar-to-hydrogen energy conversion: recent advances of CdS. Curr. Anal. Chem. **17**(5), 573–589 (2021). https://doi.org/10.2174/1573411016666200106103712
298. J.A. Nasir, Z.U. Rehman, S.N. Ali Shah, A. Khan, I.S. Butler et al., Recent developments and perspectives in CdS-based photocatalysts for water splitting. J. Mater. Chem. A **8**(40), 20752–20780 (2020). https://doi.org/10.1039/d0ta05834c
299. X. Zheng, Y. Song, Y. Liu, J. Li, Y. Yang et al., Synthesis of phase junction cadmium sulfide photocatalyst under sulfur-rich solution system for efficient photocatalytic hydrogen evolution. Small **19**(19), e2207623 (2023). https://doi.org/10.1002/smll.202207623
300. Y. Liu, X. Zheng, Y. Yang, Y. Song, Y. Yang et al., Recent advances in the hydrogen evolution reaction of $Zn_xCd_{1-x}S$-based photocatalysts. Solar RRL **6**(4), 2101061 (2022). https://doi.org/10.1002/solr.202101061
301. Q. Li, H. Meng, P. Zhou, Y. Zheng, J. Wang et al., $Zn_{1-x}Cd_xS$ solid solutions with controlled bandgap and enhanced visible-light photocatalytic H_2-production activity. ACS Catal. **3**(5), 882–889 (2013). https://doi.org/10.1021/cs4000975
302. X. Gao, D. Zeng, J. Yang, W.-J. Ong, T. Fujita et al., Ultrathin $Ni(OH)_2$ nanosheets decorated with $Zn_{0.5}Cd_{0.5}S$ nanoparticles as 2D/0D heterojunctions for highly enhanced visible light-driven photocatalytic hydrogen evolution. Chin. J. Catal. **42**(7), 1137–1146 (2021). https://doi.org/10.1016/S1872-2067(20)63728-7
303. J. Yu, P. Su, D. Zhang, H. Zhao, N. Yang et al., A S-scheme 0D/2D heterojunction formed by decorating $Cd_{0.5}Zn_{0.5}S$ nanoparticles on Cu_2MoS_4 plates for efficient photocatalytic hydrogen generation. Sep. Purif. Technol. **354**, 128694 (2025). https://doi.org/10.1016/j.seppur.2024.128694
304. Z. Wang, L. Wang, B. Cheng, H. Yu, J. Yu, Photocatalytic H_2 evolution coupled with furfuralcohol oxidation over Pt-modified ZnCdS solid solution. Small Methods **5**(11), e2100979 (2021). https://doi.org/10.1002/smtd.202100979
305. L. Ma, M. Liu, D. Jing, L. Guo, Photocatalytic hydrogen production over CdS: effects of reaction atmosphere studied by *in situ* Raman spectroscopy. J. Mater. Chem. A **3**(10), 5701–5707 (2015). https://doi.org/10.1039/C4TA06577H
306. W.-J. Zhong, M.-Y. Hung, Y.-T. Kuo, H.-K. Tian, C.-N. Tsai et al., Dual-vacancy-engineered $ZnIn_2S_4$ nanosheets for harnessing low-frequency vibration induced piezoelectric polarization coupled with static dipole field to enhance photocatalytic H_2 evolution. Adv. Mater. **36**(36), 2403228 (2024). https://doi.org/10.1002/adma.202403228
307. Z. Bao, Y. Wang, J. Hu, J. Geng, S. Ma et al., Heterojunction photocatalyst MnO_2-$CsSnI_3$ for highly efficient formaldehyde oxidation at room temperature. Chem. Eng. J. **497**, 154697 (2024). https://doi.org/10.1016/j.cej.2024.154697
308. F. Tan, F. Liu, J. Li, K. Shi, Electronic and optical properties of $CsSnI_3$/MoS_2 heterostructure as ultrabroadband photoelectric device. Appl. Surf. Sci. **678**, 161048 (2024). https://doi.org/10.1016/j.apsusc.2024.161048
309. A. Thanetchaiyakup, M. Sadek, W.X. Chan, Y. Qian, J. Yang et al., Lead-free metal halide double perovskite-photoelectrocatalyzed activation of $C(sp^3)$-H bonds and alkylation of alkenes and azo compounds. JACS Au **5**(7), 3189–3202 (2025). https://doi.org/10.1021/jacsau.5c00366
310. W. Liu, M. Cui, Y. Shi, Y. Ming, P. Yuan et al., Large area flexible Cs_2TeI_6 films based on optimized solvent annealing for high performance X-ray detection. J. Alloys Compd. **1036**, 181871 (2025). https://doi.org/10.1016/j.jallcom.2025.181871
311. Y. Xiao, K. Choudhuri, A. Thanetchaiyakup, W.X. Chan, X. Hu et al., Machine-learning-assisted discovery of mechanosynthesized lead-free metal halide perovskites for the oxidative photocatalytic cleavage of alkenes. Adv. Sci. **11**(29), 2309714 (2024). https://doi.org/10.1002/advs.202309714
312. T. Huang, B. Gao, M. Li, X. Zhou, W. He et al., Cathode-free aqueous micro-battery for an all-in-one wearable system with ultralong stability. Adv. Energy Mater. **15**(4), 2402871 (2025). https://doi.org/10.1002/aenm.202402871
313. J. Liu, L. Chen, H. Dong, L. Fu, H. Xiong et al., A numerical study on the performance of a novel arc-shaped solid oxide fuel cell. Int. J. Hydrog. Energy **105**, 1207–1216 (2025). https://doi.org/10.1016/j.ijhydene.2025.01.386

314. J. Liu, L. Liang, B. Su, D. Wu, Y. Zhang et al., Transformative strategies in photocatalyst design: merging computational methods and deep learning. J. Mater. Inf. **4**(4), 33 (2024). https://doi.org/10.20517/jmi.2024.48
315. F. Zheng, B. Yuan, Y. Cai, H. Xiang, C. Tang et al., Machine learning tailored anodes for efficient hydrogen energy generation in proton-conducting solid oxide electrolysis cells. Nano-Micro Lett. **17**(1), 274 (2025). https://doi.org/10.1007/s40820-025-01764-7
316. X. Li, H. Mai, J. Lu, X. Wen, T.C. Le et al., Rational atom substitution to obtain efficient, lead-free photocatalytic perovskites assisted by machine learning and DFT calculations. Angew. Chem. Int. Ed. **62**(52), e202315002 (2023). https://doi.org/10.1002/anie.202315002
317. F. Häse, L.M. Roch, P. Friederich, A. Aspuru-Guzik, Designing and understanding light-harvesting devices with machine learning. Nat. Commun. **11**(1), 4587 (2020). https://doi.org/10.1038/s41467-020-17995-8
318. Y. Bai, L. Wilbraham, B.J. Slater, M.A. Zwijnenburg, R.S. Sprick et al., Accelerated discovery of organic polymer photocatalysts for hydrogen evolution from water through the integration of experiment and theory. J. Am. Chem. Soc. **141**(22), 9063–9071 (2019). https://doi.org/10.1021/jacs.9b03591
319. J. Liu, Q. Wang, L. Fu, L. Chen, H. Dong, Numerical study of the effects of obstacles in the flow channel on the long-term stability performance of solid oxide fuel cells. Int. J. Hydrog. Energy **133**, 165–176 (2025). https://doi.org/10.1016/j.ijhydene.2025.04.383
320. B.-R. Su, J.-Q. Liu, D. Zhao, D. Wu, C.-Q. Hu et al., Past, present, prospect: AI-driven evolution of low-dimensional material design for sustainable environmental solutions. Rare Met. (2025). https://doi.org/10.1007/s12598-025-03631-1
321. Y. Yue, N. Liu, T. Su, Y. Cheng, W. Liu et al., Self-powered nanofluidic pressure sensor with a linear transfer mechanism. Adv. Funct. Mater. **33**(13), 2211613 (2023). https://doi.org/10.1002/adfm.202211613
322. K. Zhao, X. Peng, S. Hu, X. Wang, Machine learning models for rapid prediction of chemicals' life-cycle environmental impacts: current status, challenges, and future directions. Green Carbon **3**(4), 433–442 (2025). https://doi.org/10.1016/j.greenca.2025.05.004
323. H. Mai, T.C. Le, D. Chen, D.A. Winkler, R.A. Caruso, Machine learning for electrocatalyst and photocatalyst design and discovery. Chem. Rev. **122**(16), 13478–13515 (2022). https://doi.org/10.1021/acs.chemrev.2c00061
324. S. Zhao, M. Liu, Y. Zhang, Z. Zhao, Q. Zhang et al., Harvesting mechanical energy for hydrogen generation by piezoelectric metal-organic frameworks. Mater. Horiz. **9**(7), 1978–1983 (2022). https://doi.org/10.1039/d1mh01973b
325. Q. Wang, D. Astruc, State of the art and prospects in metal-organic framework (MOF)-based and MOF-derived nanocatalysis. Chem. Rev. **120**(2), 1438–1511 (2020). https://doi.org/10.1021/acs.chemrev.9b00223
326. D. Chakraborty, A. Yurdusen, G. Mouchaham, F. Nouar, C. Serre, Large-scale production of metal–organic frameworks. Adv. Funct. Mater. **34**(43), 2309089 (2024). https://doi.org/10.1002/adfm.202309089
327. H. Hu, X. Sun, Y. Ma, H. Li, W. Zhang et al., Anchoring redox mediator on COFs for efficient solar to hydrogen conversion. Adv. Mater. **37**(45), e10193 (2025). https://doi.org/10.1002/adma.202510193
328. W. Dai, C. Wang, Y. Wang, J. Sun, H. Ruan et al., Unlocking photocatalytic NO removal potential in an S-type UiO-66-NH_2/ZnS(en)$_{0.5}$ heterostructure. Interdiscip. Mater. **3**(3), 400–413 (2024). https://doi.org/10.1002/idm2.12160
329. M. Wu, Z. Zhou, Covalent organic frameworks as electrode materials for rechargeable metal-ion batteries. Interdiscip. Mater. **2**(2), 231–259 (2023). https://doi.org/10.1002/idm2.12070
330. J. Hong, W. Li, J. Shang, H. Yamashita, Y. Hu, Constructing Cu_0/Cu^+ interfaces on Cu-based MOF derivatives to promote the adsorption stability of intermediates in the process of CO_2 electroreduction to C_2 products. Environ. Sci. Nano **11**(10), 4230–4239 (2024). https://doi.org/10.1039/D4EN00466C
331. X. Huang, K.-Y. Wu, C. Su, L. Yang, B.-B. Xiao, Metal-organic framework Cu-BTC for overall water splitting: a density functional theory study. Chin. Chem. Lett. **36**(4), 109720 (2025). https://doi.org/10.1016/j.cclet.2024.109720
332. M. Wang, Y. Hong, W. He, Q. Zhang, G. Yu et al., Nature-inspired MXene electrode with the highly interconnected gradient nanoconfined architecture. Adv. Mater. **37**(45), e11444 (2025). https://doi.org/10.1002/adma.202511444
333. M. Wang, Y. Cheng, H. Zhang, F. Cheng, Y. Wang et al., Nature-inspired interconnected macro/meso/micro-porous MXene electrode. Adv. Funct. Mater. **33**(12), 2211199 (2023). https://doi.org/10.1002/adfm.202211199
334. Y. Li, L. Ding, S. Yin, Z. Liang, Y. Xue et al., Photocatalytic H_2 evolution on TiO_2 assembled with Ti_3C_2 MXene and metallic 1T-WS_2 as co-catalysts. Nano-Micro Lett. **12**(1), 6 (2019). https://doi.org/10.1007/s40820-019-0339-0
335. C. Chen, X. Tang, M. Wang, Y. Ma, S. Wang et al., Multiscale porous structured MXene: synthesis, design and applications in batteries and supercapacitors. Mater. Today **88**, 526–551 (2025). https://doi.org/10.1016/j.mattod.2025.05.021
336. Z. Lei, S. Ali, C.I. Sathish, M. Ahmed, J. Qu et al., Transition metal carbonitride MXenes anchored with Pt sub-nanometer clusters to achieve high-performance hydrogen evolution reaction at all pH range. Nano-Micro Lett. **17**(1), 123 (2025). https://doi.org/10.1007/s40820-025-01654-y
337. S. Zhao, X. Luo, Y. Cheng, Z. Shi, T. Huang et al., A flexible zinc ion hybrid capacitor integrated system with layers-dependent V_2CT_x MXene. Chem. Eng. J. **454**, 140360 (2023). https://doi.org/10.1016/j.cej.2022.140360
338. D. Zhao, Y. Wang, C.-L. Dong, Y.-C. Huang, J. Chen et al., Boron-doped nitrogen-deficient carbon nitride-based Z-scheme heterostructures for photocatalytic overall water splitting. Nat. Energy **6**(4), 388–397 (2021). https://doi.org/10.1038/s41560-021-00795-9

 https://doi.org/10.1007/s40820-026-02111-0

339. D. Zhao, C.-L. Dong, B. Wang, C. Chen, Y.-C. Huang et al., Synergy of dopants and defects in graphitic carbon nitride with exceptionally modulated band structures for efficient photocatalytic oxygen evolution. Adv. Mater. **31**(43), 1903545 (2019). https://doi.org/10.1002/adma.201903545

340. D. Ma, Z. Zhang, Y. Zou, J. Chen, J.-W. Shi, The progress of g-C_3N_4 in photocatalytic H_2 evolution: from fabrication to modification. Coord. Chem. Rev. **500**, 215489 (2024). https://doi.org/10.1016/j.ccr.2023.215489

341. I. Khan, T. Benkó, A. Horváth, S. Shen, J. Su et al., Photoelectrochemical water splitting by hematite boosted in a heterojunction with B-doped g-C_3N_4 nanosheets and carbon nanotubes. J. Mater. Chem. A **12**(30), 19247–19258 (2024). https://doi.org/10.1039/D4TA02512A

342. J. Liu, N. Tian, S. Ren, Z. Zhang, Z. Yang et al., Which type of carbon nitride more suits photocatalysis: amorphous or crystalline? Adv. Funct. Mater. **35**(3), 2413406 (2025). https://doi.org/10.1002/adfm.202413406

343. Z. Chen, G. Ding, Z. Wang, Y. Xiao, X. Liu et al., Precision molecular engineering of carbon nitride for efficient and selective photoreduction of CO_2 to C_2H_6 in pure water. Adv. Funct. Mater. **35**(25), 2423213 (2025). https://doi.org/10.1002/adfm.202423213

344. Z. Chen, D. Yan, X. Wang, G. Ding, Z. Wang et al., Biochar-tailored carbon nitride enables piezo-photocatalytic H_2O_2 production *via* boosted charge transport. ACS Catal. **15**(15), 13568–13580 (2025). https://doi.org/10.1021/acscatal.5c02889

345. F. Su, M. Tian, H. Cao, Z. Wang, Q. Zhao et al., Constructing a Z-scheme heterojunction of oxygen-deficient WO_{3-x} and g-C_3N_4 for superior photocatalytic evolution of H_2. Surf. Interfaces **55**, 105346 (2024). https://doi.org/10.1016/j.surfin.2024.105346

346. C. Huang, Q. Chen, Y. Chen, L. Wang, M. Wu et al., Regulating interfacial molecule activation and carrier dynamics by engineering Fe single-atoms modified g-C_3N_4 for efficient photocatalytic oxidation. Chem. Eng. J. **525**, 170570 (2025). https://doi.org/10.1016/j.cej.2025.170570

347. C. Yang, H. Cao, F. Su, M. Tian, H. Xie et al., Structural distortion of g- C_3N_4 induced by a schiff base reaction for efficient photocatalytic H_2 evolution. Chem. Asian J. **19**(18), e202400588 (2024). https://doi.org/10.1002/asia.202400588

348. C. Wu, S. Wu, Q. Huang, K. Sun, X. Huang et al., Potassium-modified carbon nitride photocatalyzed-aminoacylation of N-sulfonyl ketimines. Chin. Chem. Lett. **36**(2), 110250 (2025). https://doi.org/10.1016/j.cclet.2024.110250

349. Y. Wang, A. Vogel, M. Sachs, R.S. Sprick, L. Wilbraham et al., Current understanding and challenges of solar-driven hydrogen generation using polymeric photocatalysts. Nat. Energy **4**(9), 746–760 (2019). https://doi.org/10.1038/s41560-019-0456-5

350. T. Hisatomi, K. Domen, Reaction systems for solar hydrogen production *via* water splitting with particulate semiconductor photocatalysts. Nat. Catal. **2**(5), 387–399 (2019). https://doi.org/10.1038/s41929-019-0242-6

351. J. Zhang, W. Hu, S. Cao, L. Piao, Recent progress for hydrogen production by photocatalytic natural or simulated seawater splitting. Nano Res. **13**(9), 2313–2322 (2020). https://doi.org/10.1007/s12274-020-2880-z

352. H. Nishiyama, T. Yamada, M. Nakabayashi, Y. Maehara, M. Yamaguchi et al., Photocatalytic solar hydrogen production from water on a 100-m^2 scale. Nature **598**(7880), 304–307 (2021). https://doi.org/10.1038/s41586-021-03907-3

353. C. Cheng, J. Zhang, R. Zeng, F. Xing, C. Huang, Schottky barrier tuning *via* surface plasmon and vacancies for enhanced photocatalytic H_2 evolution in seawater. Appl. Catal. B Environ. **310**, 121321 (2022). https://doi.org/10.1016/j.apcatb.2022.121321

354. P. Zhou, I.A. Navid, Y. Ma, Y. Xiao, P. Wang et al., Solar-to-hydrogen efficiency of more than 9% in photocatalytic water splitting. Nature **613**(7942), 66–70 (2023). https://doi.org/10.1038/s41586-022-05399-1

355. H. Ling, H. Sun, L. Lu, J. Zhang, L. Liao et al., Sustainable photocatalytic hydrogen peroxide production over octonary high-entropy oxide. Nat. Commun. **15**(1), 9505 (2024). https://doi.org/10.1038/s41467-024-53896-w

356. Y. Yang, Y. Zheng, S. Liu, M. Shan, J. Guo et al., Deep learning prediction of photocatalytic water splitting for hydrogen production under natural light based on experiments. Energy Convers. Manage. **301**, 118007 (2024). https://doi.org/10.1016/j.enconman.2023.118007

357. X. Guan, F.A. Chowdhury, N. Pant, L. Guo, L. Vayssieres et al., Efficient unassisted overall photocatalytic seawater splitting on GaN-based nanowire arrays. J. Phys. Chem. C **122**(25), 13797–13802 (2018). https://doi.org/10.1021/acs.jpcc.8b00875

358. S. Ning, H. Ou, Y. Li, C. Lv, S. Wang et al., Co^0–$Co^{\delta+}$ interface double-site-mediated C–C coupling for the photothermal conversion of CO_2 into light olefins. Angew. Chem. Int. Ed. **62**(23), e202302253 (2023). https://doi.org/10.1002/anie.202302253

359. T. Peng, Y. Wang, C.-L. Dong, T.T.T. Nga, B. Wu et al., BiOCl atomic layers with electrons enriched active sites exposed for efficient photocatalytic CO_2 overall splitting. Nano-Micro Lett. **17**(1), 223 (2025). https://doi.org/10.1007/s40820-025-01723-2

360. S. Ning, Y. Zhu, S. Zhang, X. Wu, X. Yin et al., Light-driven electronic restructuring in RuCu alloy catalysts for selective CO_2-to-methanol conversion. Adv. Funct. Mater. (2025). https://doi.org/10.1002/adfm.202514006

361. X. Wu, S. Zhang, S. Ning, C. Yang, L. Li et al., Recent advances and developments in solar-driven photothermal catalytic CO_2 reduction into multicarbon (C_{2+}) products.

Chem. Sci. **16**(11), 4568–4594 (2025). https://doi.org/10.1039/d5sc00330j

362. J. Pan, G. Zhang, Z. Guan, Q. Zhao, G. Li et al., Anchoring Ni single atoms on sulfur-vacancy-enriched $ZnIn_2S_4$ nanosheets for boosting photocatalytic hydrogen evolution. J. Energy Chem. **58**, 408–414 (2021). https://doi.org/10.1016/j.jechem.2020.10.030
363. J. Zhang, L. Li, M. Du, Y. Cui, Y. Li et al., Single-atom phosphorus defects decorated CoP cocatalyst boosts photocatalytic hydrogen generation performance of $Cd_{0.5}Zn_{0.5}S$ by directed separating the photogenerated carriers. Small **19**(20), e2300402 (2023). https://doi.org/10.1002/smll.202300402
364. K. Yang, Y. Huang, T. Wang, Y. Li, Y. Du et al., *In-situ* anchoring of co single-atom synergistically with Cd vacancy of cadmium sulfide for boosting asymmetric charge distribution and photocatalytic hydrogen evolution. Adv. Mater. **36**(48), 2409832 (2024). https://doi.org/10.1002/adma.202409832
365. Z. Chen, L. Wang, X. Jiao, Y. Xia, D. Chen, Defect-mediated spatial confinement of Pt single atoms on photoactive $CdIn_2S_4$ octahedrons: synergistic carrier dynamics optimization for photocatalytic hydrogen production. Chem. Eng. J. **517**, 164289 (2025). https://doi.org/10.1016/j.cej.2025.164289
366. D. Zhang, C. Zhang, H. Ma, B. Ye, T. Zhuang et al., Rh single atoms anchored in hollow microflower MoS_2/sulfur-vacancy rich CdZnS with dual proton reduction sites for enhanced photocatalytic hydrogen generation. J. Colloid Interface Sci. **684**, 207–214 (2025). https://doi.org/10.1016/j.jcis.2025.01.104
367. D. Zhang, C. Zhang, H. Wang, L. Jiang, C. Wang et al., Single-atom RhS bond on defective CdZnS for enhanced photocatalytic hydrogen production. Sep. Purif. Technol. **357**, 130022 (2025). https://doi.org/10.1016/j.seppur.2024.130022
368. C. Zhang, C. Xie, Y. Gao, X. Tao, C. Ding et al., Charge separation by creating band bending in metal-organic frameworks for improved photocatalytic hydrogen evolution. Angew. Chem. Int. Ed. **61**(28), e202204108 (2022). https://doi.org/10.1002/anie.202204108
369. Q. Mo, L. Zhang, S. Li, H. Song, Y. Fan et al., Engineering single-atom sites into pore-confined nanospaces of porphyrinic metal-organic frameworks for the highly efficient photocatalytic hydrogen evolution reaction. J. Am. Chem. Soc. **144**(49), 22747–22758 (2022). https://doi.org/10.1021/jacs.2c10801
370. P. Ayala, S. Naghdi, S.P. Nandan, S.N. Myakala, J. Rath et al., The emergence of 2D building units in metal-organic frameworks for photocatalytic hydrogen evolution: a case study with COK-47. Adv. Energy Mater. **13**(31), 2300961 (2023). https://doi.org/10.1002/aenm.202300961
371. Z. Li, J. Zi, X. Luan, Y. Zhong, M. Qu et al., Localized surface plasmon resonance promotes metal–organic framework-based photocatalytic hydrogen evolution. Adv. Funct. Mater. **33**(33), 2303069 (2023). https://doi.org/10.1002/adfm.202303069
372. L. Tang, Q.-C. Lin, Z. Jiang, J. Hu, Z. Liu et al., Nanoscaling and heterojunction for photocatalytic hydrogen evolution by bimetallic metal-organic frameworks. Adv. Funct. Mater. **33**(22), 2214450 (2023). https://doi.org/10.1002/adfm.202214450
373. L. Liu, H. Meng, Y. Chai, X. Chen, J. Xu et al., Enhancing built-in electric fields for efficient photocatalytic hydrogen evolution by encapsulating C_{60} fullerene into zirconium-based metal-organic frameworks. Angew. Chem. Int. Ed. **135**(11), e202217897 (2023). https://doi.org/10.1002/ange.202217897
374. S. Qi, K. Zhu, T. Xu, H. Zhang, X. Guo et al., Water-stable high-entropy metal-organic framework nanosheets for photocatalytic hydrogen production. Adv. Mater. **36**(26), e2403328 (2024). https://doi.org/10.1002/adma.202403328
375. S. Zhang, L. Lu, J. Jiang, N. Liu, B. Zhao et al., Organizing photosensitive and photothermal single-sites uniformly in a trimetallic metal-organic framework for efficient photocatalytic hydrogen evolution. Adv. Mater. **36**(26), e2403464 (2024). https://doi.org/10.1002/adma.202403464
376. B. Chen, A. Mansouri, C.M. Rueda-Navarro, I. Dovgaliuk, P. Boullay et al., A novel Ti_{12}-based metal-organic framework for photocatalytic hydrogen evolution. Adv. Energy Mater. **15**(26), 2500211 (2025). https://doi.org/10.1002/aenm.202500211
377. Y. Li, J. Huang, M.-L. Gao, X. Zhang, S. Chen et al., Decoration of metal-organic frameworks with coenzyme mimics for boosting photocatalytic hydrogen production. Angew. Chem. Int. Ed. **64**(40), e202511775 (2025). https://doi.org/10.1002/anie.202511775
378. H. Lei, J. Zhang, Z. Wu, Y. Ye, Z. Li et al., Crystal facet-dependent photocatalytic hydrogen evolution from ultra-stable Cu-Zr/Hf heterobimetallic metal-organic frameworks. Angew. Chem. Int. Ed. **64**(37), e202509572 (2025). https://doi.org/10.1002/anie.202509572
379. S. Ma, T. Deng, Z. Li, Z. Zhang, J. Jia et al., Photocatalytic hydrogen production on a sp_2-carbon-linked covalent organic framework. Angew. Chem. Int. Ed. **134**(42), e202208919 (2022). https://doi.org/10.1002/ange.202208919
380. Y. Chen, X. Luo, J. Zhang, L. Hu, T. Xu et al., Bandgap engineering of covalent organic frameworks for boosting photocatalytic hydrogen evolution from water. J. Mater. Chem. A **10**(46), 24620–24627 (2022). https://doi.org/10.1039/d2ta07271h
381. Y. Li, L. Yang, H. He, L. Sun, H. Wang et al., *In situ* photodeposition of platinum clusters on a covalent organic framework for photocatalytic hydrogen production. Nat. Commun. **13**(1), 1355 (2022). https://doi.org/10.1038/s41467-022-29076-z
382. W. Weng, J. Guo, The effect of enantioselective chiral covalent organic frameworks and cysteine sacrificial donors on photocatalytic hydrogen evolution. Nat. Commun. **13**(1), 5768 (2022). https://doi.org/10.1038/s41467-022-33501-8
383. R. Shen, X. Li, C. Qin, P. Zhang, X. Li, Efficient photocatalytic hydrogen evolution by modulating excitonic effects in

 https://doi.org/10.1007/s40820-026-02111-0

Ni-intercalated covalent organic frameworks. Adv. Energy Mater. **13**(13), 2203695 (2023). https://doi.org/10.1002/aenm.202203695

384. W. Zhou, Q.-W. Deng, H.-J. He, L. Yang, T.-Y. Liu et al., Heterogenization of salen metal molecular catalysts in covalent organic frameworks for photocatalytic hydrogen evolution. Angew. Chem. Int. Ed. **62**(3), e202214143 (2023). https://doi.org/10.1002/anie.202214143
385. H. Zhang, Z. Lin, P. Kidkhunthod, J. Guo, Stable immobilization of nickel ions on covalent organic frameworks for panchromatic photocatalytic hydrogen evolution. Angew. Chem. Int. Ed. **62**(21), e202217527 (2023). https://doi.org/10.1002/anie.202217527
386. X. Guan, Y. Qian, X. Zhang, H.-L. Jiang, Enaminone-linked covalent organic frameworks for boosting photocatalytic hydrogen production. Angew. Chem. Int. Ed. **62**(31), e202306135 (2023). https://doi.org/10.1002/anie.202306135
387. S. Wang, T. Wu, S. Wu, J. Guo, T. He et al., Cobaloxime-integrated covalent organic frameworks for photocatalytic hydrogen evolution coupled with alcohol oxidation. Angew. Chem. Int. Ed. **62**(44), e202311082 (2023). https://doi.org/10.1002/anie.202311082
388. Z. Li, T. Deng, S. Ma, Z. Zhang, G. Wu et al., Three-component donor-π-acceptor covalent-organic frameworks for boosting photocatalytic hydrogen evolution. J. Am. Chem. Soc. **145**(15), 8364–8374 (2023). https://doi.org/10.1021/jacs.2c11893
389. Y. Zhong, W. Dong, S. Ren, L. Li, Oligo(phenylenevinylene)-based covalent organic frameworks with kagome lattice for boosting photocatalytic hydrogen evolution. Adv. Mater. **36**(1), e2308251 (2024). https://doi.org/10.1002/adma.202308251
390. W. Zhao, L. Luo, M. Cong, X. Liu, Z. Zhang et al., Nanoscale covalent organic frameworks for enhanced photocatalytic hydrogen production. Nat. Commun. **15**(1), 6482 (2024). https://doi.org/10.1038/s41467-024-50839-3